UNIVERSITÄT HAMBURG
DEPARTMENT PHYSIK

Development of an X-ray delay unit for correlation spectroscopy and pump - probe experiments

Dissertation zur Erlangung des Doktorgrades des Fachbereichs Physik der Universität Hamburg

vorgelegt von

Wojciech Roseker

aus Bydgoszcz, Polen

Hamburg

2008

Gutachter der Dissertation:

Prof. Dr. W. Wurth
Prof. Dr. E. F. Weckert

Gutachter der Disputation:

Prof. Dr. W. Wurth
Dr. G. Grübel

Datum der Disputation:

26.06.2008

Vorsitzender des Prüfungsausschusses:

Dr. M. Martins

Vorsitzender des Promotionsausschusses:

Prof. Dr. J. Bartels

Dekan des Fachbereichs Physik:

Prof. Dr. A. Frühwald

Abstract

Probing condensed matter on time scales ranging from femtoseconds to nanoseconds will be one of the key topics for future X-ray Free Electron Laser (XFEL) sources. The accessible time windows are, however, compromised by the intrinsic time structure of the sources. One way to overcome this limitation is the usage of a time delay unit. A prototype device capable of splitting an X-ray pulse into two adjustable fractions, delaying one of them with the aim to perform X-ray Photon Correlation Spectroscopy and pump - probe type studies was designed and manufactured. The device utilizes eight perfect crystals in vertical 90° scattering geometry. Its performance has been verified with 8.39 keV and 12.4 keV X-rays at various synchrotron sources. The measured throughput of the device with a Si(333) monochromator at 8.39 keV under ambient conditions is 0.6%. The stability was verified at 12.4 keV and operation without realignment and feedback was possible for more than 30 minutes. Time delays up to 2.95 ns have been achieved. The highest resolution achieved in an experiment was 15.4 ps, a value entirely determined by the diagnostics system. The influence of the delay unit optics on the coherence properties of the beam was investigated by means of Fraunhofer diffraction and static speckle analysis. The obtained high fringe visibility and contrast values larger than 23% indicate the feasibility of performing coherence based experiments with the delay line.

Zusammenfassung

Das Studium kondensierter Materie auf Femto- bis Nanosekunden Zeitsskalen wird eines der Hauptanwendungsgebiete zukünftiger Freier Elektronen Laser Quellen (XFEL) im Röntgenspektralbereich sein. Die zugänglichen Zeitfenster sind aber durch die interne Zeitstruktur der Quellen begrenzt. Eine optische Verzögerungseinheit ('time delay unit') zur zeitlichen Verzögerung eines Röntgenpulses erlaubt es diese Limitation zu überwinden. Ein Prototyp einer solchen Einheit wurde entwickelt der es erlaubt einen Röntgenpuls in zwei (unterschiedlich intensive) Unterpulse zu teilen, diese relativ zueinander zu verzögern mit dem Ziel Röntgenkorrelationsspektroskopie und Pump-Probe Studien durchzuführen zu können. Die Optikeinheit basiert auf 8 perfekten Kristallen, die in vertikaler (90 Grad) Streugeometrie angeordnet sind. Die Leistungsfähigkeit der Einheit wurde mit Röntgenstrahlung der Energie 8.39 keV und 12.4 keV an verschiedenen Synchrotronstrahlungsquellen getestet. Die Transmission der Einheit mit Si(333) Vor-Monochromator beträgt 0.6% bei 8.39 keV. Die Stabilität der Einheit wurde bei 12.4 keV verifiziert und der Betrieb war für 30 Minuten ohne Nachjustage und Feed-back System möglich. Laufzeitunterschiede von bis zu 2.95 ns wurden erzielt. Die höchste Zeitauflösung war nur durch die intrinsische Zeitauflösung des Detektorsystems limitiert und betrug 15.4 ps. Ein eventueller Einfluss der optischen Elemente auf die Kohärenzeigenschaften des Strahls wurden in Fraunhoferbeugungsmessungen und durch die Analyse statischer Specklemuster untersucht. Der hohe Interferenzkontrast der Beugungsmuster und Speckle-Kontrastwerte über 23% lassen erwarten daß kohärenzbasierte Experimente mit der Verzögerungseinheit möglich sein werden.

Contents

Chapter 1

Introduction

1.1 Probing ultra-fast dynamics

Various processes in matter involve structural changes on fast and ultra-fast[1] time scales. Probing matter on a time scale from femto to nanoseconds will be one of the key topics for time resolved experiments at the future X-ray Free Electron Laser (XFEL) sources [1–3]. The improvement of ultra-short pulsed laser sources allowed to inspect ultra-fast phenomena such as bond formation and bond breaking in matter by optically pumping and probing matter [4]. However, if visible light is used to probe fast dynamics it is impossible to directly resolve the rearrangement of atoms or molecules in matter on an atomic scale. Hard X-rays, with wavelengths comparable to interatomic distances are however well suited to measure structural dynamics with atomic scale resolution.

Early X-ray sources such as X-ray tubes were unable to provide both, high spatial and temporal resolution. Storage ring sources deliver nowadays highly intense photon pulses with a duration of about 100 ps that allow performing time resolved experiments [5]. However, for many applications that are e.g. concerned with the monitoring of electronic dynamics, the duration of storage ring pulses is still too long.

New sources and techniques, based on higher harmonic generation [6], laser-produced plasma sources [7] or slicing techniques of synchrotron radiation [8] have been demonstrated recently. They provide ultra-short X-ray pulses suited for the determination of atomic rearrangements. However, all these sources are still limited in the number of photons per pulse.

Free Electron Lasers such as the Linac Coherent Light Source (LCLS) at Stanford, USA [9], the European XFEL in Hamburg [10] and the XFEL in Hyogo, Japan [3] will produce ultra-short and very intense photon pulses. The European XFEL will provide 100 fs long pulses, each supplying typically 10^{12} photons. The time structure of the machine consists of single pulses separated by 200 ns arranged into bunch trains of 3000 pulses arriving with a repetition rate of 10 Hz. The LCLS is expected to deliver 230 fs long pulses with a repetition rate of 120 Hz.

The ultra-short pulses and the high peak brightness of future XFEL sources

[1] 'ultra-fast' here stands for picosecond times scales and below.

provide excellent conditions for probing ultra-fast time dependent phenomena. But unfortunately the minimum spacing between the photon pulses is still too long to carry out ultra-fast X-ray *pump* X-ray *probe* (cf. section 1.2) and 'split-pulse' XPCS experiments (cf. section 1.3).

The subject of this work is to build and test a device capable of splitting an X-ray pulse into two parts and recombining them on the same path with a variable time delay, so that the time structure of the beam can be adapted to the needs of the aforementioned experiments.

1.2 Pump-probe techniques

Two basic approaches can be pursued to monitor time dependent phenomena occurring in matter. In the first one a system is illuminated with a dc source and an ultra-fast detector is used to resolve the details of intermediate stages of a dynamical process. The second approach is to illuminate matter with an ultra-short pulse of radiation. Structural information of the system is then averaged over the time scale corresponding to the duration of the pulse. Due to the limited time resolution of detectors the latter approach is more often pursued.

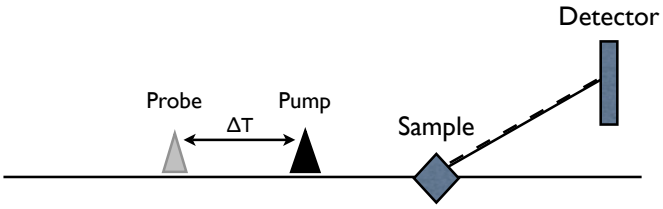

Figure 1.1: Typical scheme of pump-probe experiments

To study ultra-fast dynamics of a system upon external perturbation one can use two ultra-fast pulses as illustrated in figure 1.1. The sample is illuminated with a *pump* pulse, which initiates the process. The second pulse arrives after a time delay ΔT and *probes* the state of the system at that time. By varying the distance between both *pump* and *probe* pulses, the dynamics of the system can

be mapped out. The resolution of such experiments is determined by the pulse length and the accuracy of setting the time delay ΔT. Usually the *pump* pulse is provided by an intense femtosecond laser and the *probe* is an ultra-short X-ray pulse (see figure 1.2a). To ensure high time resolution, the two sources have to be synchronized better than the pulse duration.

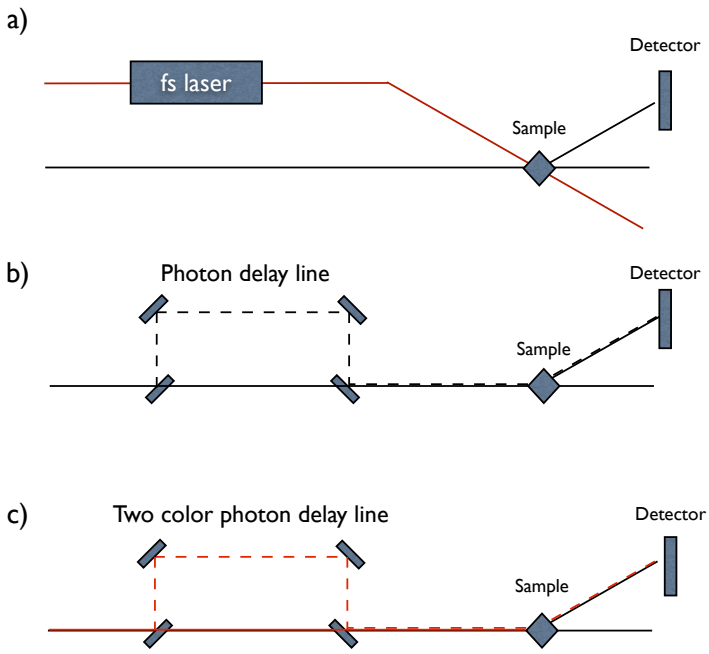

Figure 1.2: Various pump-probe schemes. a) laser *pump* and X-ray *probe*. b) X-ray *pump* and X-ray *probe* c) 'two-color' X-ray pump-probe. Red and the black colors correspond to X-ray pulses of different wavelengths.

If however, one wants to study inner shell dynamics [11] it is necessary to 'pump' the system with an X-ray pulse. In this case the *pump* and *probe* pulses should originate from the same X-ray source (see figure 1.2b). This ensures very high time resolution, which is limited only by the pulse length, since no synchronization is necessary. The most challenging part of this scheme is the design of a time delay unit, which offers easy tunability of the time delay. The class of pump-probe experiments, that involves two X-ray wavelengths is commonly referred as 'two-color' pump-probe mode and is illustrated in figure 1.2c.

1.3 Photon Correlation Spectroscopy

Photon Correlation Spectroscopy (PCS) is a technique which measures the time correlations of photons scattered by the investigated system. When a (disordered) material is illuminated by coherent light, a grainy interference pattern is produced on the detector, commonly referred to as a 'speckle patten'. This pattern reflects the spatial arrangement of scatterers in the investigated sample. When the system shows dynamics, the speckle pattern will change with time. The intensity fluctuations of a speckle can be used as a measure of the underlying dynamics in the system. The availability of 3$^{\text{rd}}$ generation storage rings producing partially coherent X-rays allows to perform PCS in the short wavelength regime by slitting out the coherent part of the beam. X-ray photon correlation spectroscopy [12] is a technique applied to study the dynamics in matter over a wide range of time scales. It can typically measure dynamics from 10^6 to 10^{-3} Hz in a q range from 10^{-6} Å^{-1} up to several Å^{-1}.

With the advent of new FEL type sources it will be possible to perform XPCS studies on time and length-scales much smaller than achievable today. The coherent peak flux of XFEL pulses is expected to be at least 9 orders of magnitude larger as compared to 3$^{\text{rd}}$ generation radiation sources. This will give access to very fast dynamics not accessible at today's storage ring sources.

For the case of the European XFEL the minimum distance between photon pulses is 200 ns. In this case only dynamics slower than $5 \cdot 10^6$ Hz can be measured in the so called 'sequential' technique [10]. In order to probe dynamics at shorter time scales the 'split-pulse' approach was proposed [13]. The concept of this technique is illustrated in figure 1.3. Each XFEL pulse is split into two equally intense pulses, that are separated in time. The time delay between the two pulses is determined by a delay line. The scattering from the two pulses is collected during the exposure time by an area detector. For a static system the contrast of the speckle pattern remains constant after a change of the delay time. However, if an investigated system shows dynamics at a time scale faster than the separation of the two pulses, the summed speckle pattern will have a lower contrast. By repeating this procedure for various delay times, the correlation

time of the system can be traced.

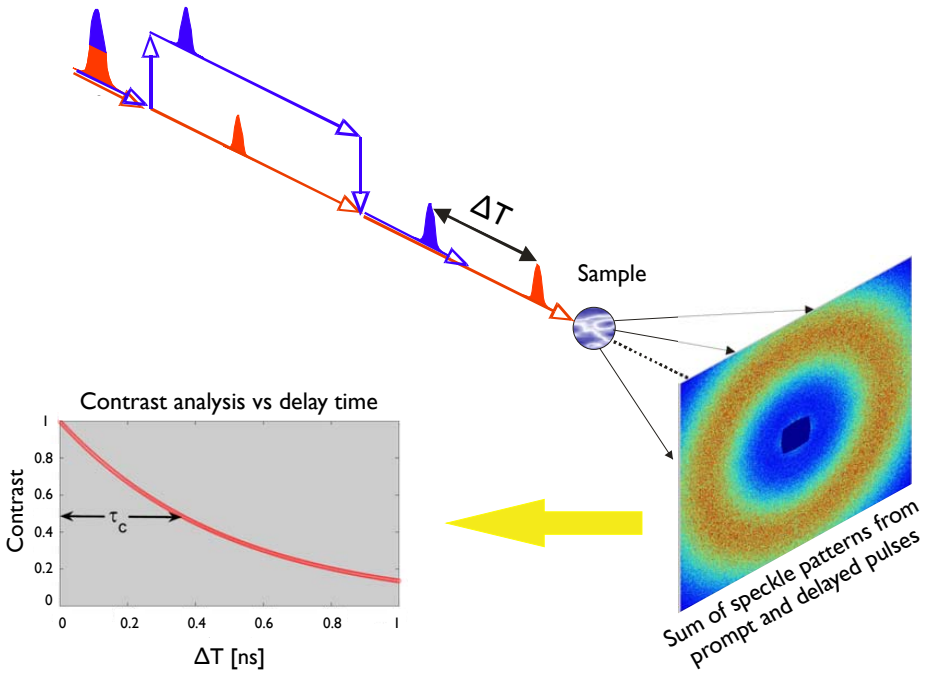

Figure 1.3: Illustration of the split-pulse technique [14].

1.4 Delay unit development

Currently available delay lines[2] work in the wavelength range down to the soft X-ray regime [15]. Equivalent devices for hard X-rays have been discussed for many years [1, 2, 16] but so far only one attempt to delay X-ray pulses at high photon energies has been reported [17]. This work presents the first operational X-ray delay unit, a device manufactured with the aim to conduct fast time domain XRD and pump-probe experiments at XFEL sources.

[2]the terms delay line and delay unit are equivalent. Both terms are used in this manuscript

1.5 Outline

The manuscript is structured in the following way: In chapter 2 the basic concept of the delay unit is described. The choice of the basic components such as beam splitters and reflective optics is discussed. Chapter 3 outlines the experimental setup of the X-ray delay unit. The performance of the delay unit is presented in chapter 4. An outlook for future work is presented in chapter 5 before concluding in chapter 6.

Chapter 2

Concept of a delay unit

This chapter introduces the concept of an X-ray delay unit for pulses of hard (8.39 - 12.4 keV) X-rays. Since the design of optical components in this energy range is based on perfect crystal optics a short introduction to diffraction with perfect crystals is presented. Furthermore, a scheme for splitting and delaying X-ray pulses is introduced. The choice of diffracting optics is based upon the demands from the present 3^{rd} and forthcoming 4^{th} generation X-ray sources. Various splitting schemes are presented. The expected performance of the proposed delay unit is discussed.

2.1 Diffraction of X-rays by single crystals

Diffraction of X-rays in single crystals can be treated according to kinematical or dynamical theory. Kinematical diffraction [18, 19] assumes that the scattering from each volume element of the crystal is independent of the other volume elements. In practice this theory can only be applied for a very small or heavily distorted crystal, exposed to an X-ray beam. The condition for diffraction in a crystal is fulfilled when the angle θ_i between the incident X-ray beam and the crystal net planes equals the Bragg angle θ_B, which is defined by

$$\theta_B = \arcsin\left(\lambda/2d_{hkl}\right) \tag{2.1}$$

where d_{hkl} and λ denote the spacing between hkl net planes in the crystal and the X-ray wavelength, respectively.

For diffraction from large and ideally perfect crystals the kinematical approach is no longer appropriate. Multiple scattering takes place when the incident beam propagates into the crystal and hence dynamical theory must be used. Many reviews of the theory can be found in the literature [18–22]. This section presents only some features of dynamical theory as a basis for the discussion of the delay unit concept.

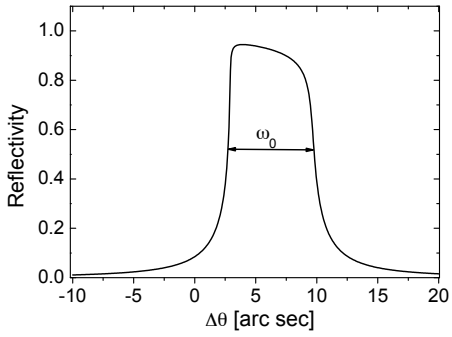

Figure 2.1: Perfect crystal reflection curve of Si(111) in the symmetric Bragg case at E=8.388 keV as a function of $\Delta\theta = \theta_i - \theta_B$, where θ_i is the incident angle. The Darwin width ω_0 is the FWHM of the rocking curve.

One of the most important effects in dynamical diffraction is the existence of a finite reflection width ω_0 (the Darwin width) for a semi-infinite perfect crystal. Figure 2.1 shows the reflectivity of a silicon (111) crystal at 8.388 keV in the so called symmetric Bragg case. The angular range of incident angles over which total reflection occurs is given by [18]

$$\omega_0 = \frac{2r_e\lambda^2}{\pi V \sin 2\theta_B}\sqrt{b}|P||F_{hkl}|e^{-M} \tag{2.2}$$

where r_e is the classical radius of the electron ($r_e = 2.82 \cdot 10^{-5}$Å), e^{-M} is the Debye-Waller factor, F_{hkl} is the structure factor of the unit cell and V its volume. From expression (2.2) it can be seen that the Darwin width also depends on the X-ray beam properties such as its wavelength λ and polarization factor P. The polarization factor equals 1 if the scattering plane is perpendicular to the polarization (σ polarization) and equals $\cos 2\theta_B$ if the scattering plane is parallel to the polarization (π polarization).

The parameter b in equation (2.2) is the asymmetry factor defined by:

$$b = \frac{\sin(\alpha + \theta_B)}{\sin(\alpha - \theta_B)} \tag{2.3}$$

Here α denotes the angle between the crystal surface and the reflecting planes.

For the symmetric Bragg reflection b = -1 ($\alpha = 0$). Negative b values indicate that the beam penetrates and exits through the same surface of the crystal, which is in fact the case of Bragg geometry (see figure 2.2a).

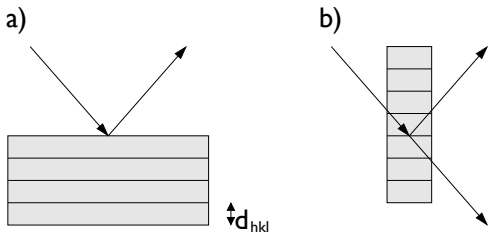

Figure 2.2: Scattering geometry of a perfect crystal with the lattice spacing d_{hkl}. Symmetric Bragg a) and Laue b) geometries.

In the symmetric Laue case $b = 1$ ($\alpha = 90°$). A positive value of b represents the Laue geometry, which is illustrated in figure 2.2b. When the surface normal is neither parallel nor perpendicular to the lattice planes $b \neq \pm 1$ and the reflection is asymmetric. Figure 2.3 illustrates the asymmetric Bragg crystal geometry. X-ray optics utilizing such reflections can modify the divergence and spatial cross section of the beam [23].

Due to refraction the center of the rocking curve is shifted from the Bragg angle by [21]

$$\Delta\theta_i = \frac{1}{2}(1-b)\cdot\Delta\theta_{os} \tag{2.4}$$

$$\Delta\theta_e = \frac{1}{2}(1-\frac{1}{b})\cdot\Delta\theta_{os} \tag{2.5}$$

for the incident θ_i and reflected θ_e beam. The parameter $\Delta\theta_{os}$ in expressions (2.4, 2.5) is

$$\Delta\theta_{os} = \frac{1}{\sin 2\theta_B}\frac{r_e\lambda^2 F_0}{\pi V} \tag{2.6}$$

where F_0 is the unit cell structure factor in the forward direction. For the symmetric reflection in Bragg geometry $\Delta\theta_e = \Delta\theta_i = \Delta\theta_{os}$. In a symmetric Laue geometry (i.e. $b = 1$) $\Delta\theta_e = \Delta\theta_i = 0$.

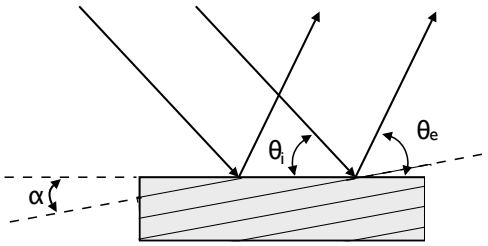

Figure 2.3: Asymmetric geometry of crystal reflection. θ_i and θ_e denotes the incidence and exit angle, respectively. The figure is drawn for the asymmetric Bragg geometry (b<0).

The integrated intensity of the Darwin reflectivity curve R is given by integrating the diffraction profile over the entire angular range.

$$I = \int_{-\infty}^{\infty} R(\theta) d\theta \tag{2.7}$$

The maximum value of the curve is called to the peak reflectivity R_{max}.

2.2 Requirements for an XFEL delay unit

As a beamline component for a future XFEL a delay unit has to fulfill specific requirements.

- The optical path length difference of the delay unit should be chosen such that the desired time range of dynamics can be investigated. Ideally, the delay unit should allow accessing time scales longer than the X-ray pulse duration and shorter than the minimum bunch spacing of the machine. For the European XFEL the delay range should cover 100 fs up to 200 ns. Expressing these numbers in path length difference yields about 30 μm to 60 m, respectively. The first value can be easily achieved with current mechanical components. For the other extreme, a delay path of 60 m is more challenging since it requires to maintain the optical stability over a large distance and dramatically increases the size of the setup or imposes the use of many crystal reflections.

- The time resolution of the delay unit should be better than the width of X-ray pulse duration.

- The opto-mechanical design of the device should guarantee stable delay times and allow one to change the delay time easily.

- The delay unit should provide operation over a wide range of wavelengths.

- The throughput of the device should be as high as possible.

- In order to conduct 'split-pulse' XPCS experiments [12] the delay unit should preserve the coherence properties of the radiation.

In order to meet these demands the following base concept is proposed.

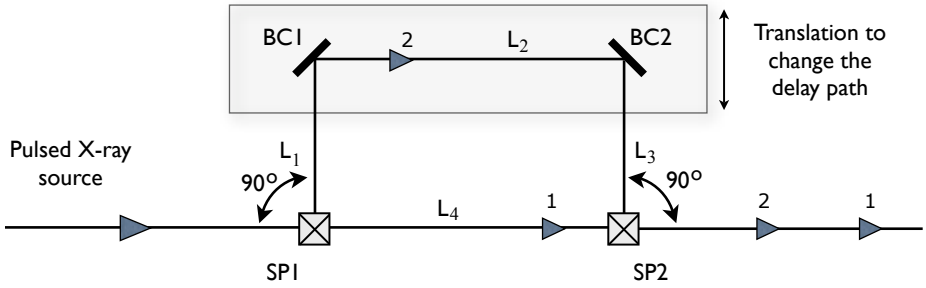

Figure 2.4: Basic concept of the X-ray delay line. Four optical components arranged in 90 degree scattering geometry. The X-ray beam is split by SP1 and follows two paths denoted $L_1 + L_2 + L_3$ and L_4, respectively. The time delay is given by the difference of the two beam path lengths. Both beams are recombined on the original path by the beam mixer SP2.

2.3 Basic concept

A simplified scheme based upon a single X-ray path [1, 2] is shown in figure 2.4. The device consists of 4 optical components arranged in 90 degree scattering geometry. The incoming X-ray pulsed beam is split by a first crystal SP1[1] and travels unequal paths defined by $L_1 + L_2 + L_3$ and L_4, respectively. After the splitter, the optical path for one fraction of the beam is defined by Bragg crystal reflectors BC1 and BC2. The second part follows a direct, straight beam path. Finally, both beams are recombined and brought back on to the primary direction by the beam mixer SP2.

The concept illustrated in figure 2.4 utilizes a beam splitting technique, which indicates that both pulses (i.e. the main pulse and its delayed replica) originate from the same electron bunch. In this way, both pulses are intrinsically synchronized to the X-ray source. The resolution of the delay line is limited then only by the stability of the optical components with respect to each other. In addition, bunch to bunch instabilities coming from the source will not affect the experiment

[1] the crossed rectangle symbol is used in figure 2.4 to denote a beam splitter. It will be shown later in this chapter that the delay unit will utilize Laue beam splitters at the SP1 and SP2 positions. A detail description of the X-ray beam splitter employed in the delay line concept is given in paragraph 2.4.1.

which takes place downstream the delay unit.

The delay between the arrival of the two split pulses introduced by the delay unit scheme of figure 2.4 is

$$\tau = \frac{L_1 + L_2 + L_3 - L_4}{c} \tag{2.8}$$

where L_1, L_2, L_3 and L_4 are the distances of the beam paths and c is the light velocity, respectively. Due to the 90 degree geometry one finds that the beam path $L_1 = L_3$ and $L_2 = L_4$, thus simplifying equation (2.8) to

$$\tau = \frac{2 \cdot L_1}{c} \tag{2.9}$$

According to equation (2.9) the delay τ can be changed by varying L_1. This can be achieved by simultaneous movement of the two Bragg crystals BC1 and BC2 in the vertical scattering plane in the direction perpendicular to the incident beam. The maximum accessible delay time for the prototype design (cf. chapter 3) is 2.84 ns. This value is comparable with the time structure of 3$^{\text{rd}}$ generation storage rings[2] and allows one to perform initial tests at these sources. Although it is of great importance to access longer delays, the aforementioned value of time delay puts already extremely high demands for the delay unit mechanical components (cf. chapter 3).

In order to avoid technical constrains[3] that would compromise the minimum delay time τ_{min} a second delay branch needs to be added. Figure 2.5 shows the scheme of two combined delay lines. Examination of figure 2.5 results in a time delay

$$\tau = |\tau_1 - \tau_2| = \Big| \underbrace{\frac{2 \cdot L_1}{c}}_{upperbranch} - \underbrace{\frac{2 \cdot L_2}{c}}_{lowerbranch} \Big| \tag{2.10}$$

According to expression (2.10) the total delay time τ is defined by two terms.

[2] The minimum bunch spacing at European Synchrotron Radiation Facility is 2.82 ns

[3] τ_{min} is defined by the minimum separation between SP1 and BC1 crystals, which cannot be smaller than the size of the crystals.

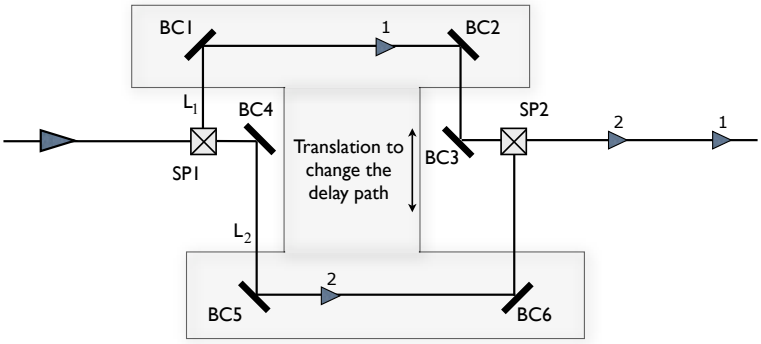

Figure 2.5: Combined delay unit schemes to achieve zero delay. The time delay is given by the difference of the distances between the two beam path lengths.

The first term τ_1 gives the delay introduced by the upper branch of the delay line only, with τ given by equation (2.9). The second term in equation (2.10) corresponds to delay introduced by the lower branch of delay line. Note that the configuration allows one to experimentally access zero delay time. The delay time τ can be changed by moving simultaneously four Bragg crystals: BC1, BC2, BC5 and BC6. When both branches L_1 and L_2 are set to be equal ($\tau = 0$) the delay unit does not affect the bunch spacing of an X-ray source (see figure 2.6a).

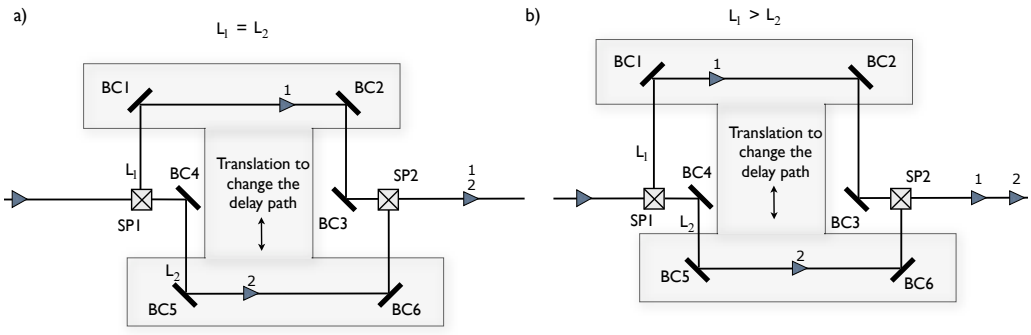

Figure 2.6: Combined delay unit schemes to achieve zero delay. a) When $L_1 = L_2$ both pulses arrives at a sample position at the same time. b) For $L_1 > L_2$ the sequence of pulses is reversed.

Accessing $\tau = 0$ is of particular interest since it allows one to calibrate the delay line independently with a precision given by the employed mechanics only.

In contrast to the one-branch concept, the minimum delay time τ_{min} is not limited by technical constrain. Translating Bragg crystals (BC1, BC2, BC5, BC6) to the case when $L_2 < L_1$ results in reversing the pulse position i.e. the *pump* pulse denoted as **1** arrives at the sample position at time τ after the *probe* pulse denoted as as **2** (see figure 2.6b).

If the incident beam is constituted of two or more wavelengths separated by the $\Delta\lambda$, which is larger than the acceptance of the delay unit beamsplitter, the setup can be utilized to perform 'two-color' or 'three-color' experiments. Figures 2.7 and 2.8 show potential schemes. The separation of photons with different wavelength takes place at the beam splitter SP1. Photons of wavelength λ_1 are diffracted by the beam splitter and travel a longer path than the photons of λ_2, which are transmitted by SP1 and SP2 accompanied by absorption losses (see figure 2.7).

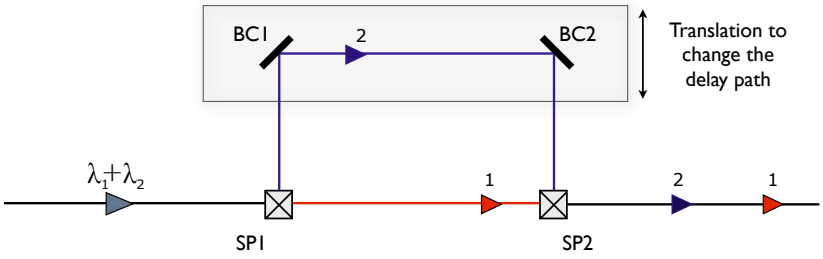

Figure 2.7: Scheme for 'two-color' time delay experiments with the one-branch configuration.

With the combined delay lines (i.e. the two-branch scheme) a 'three-color' experiments might also be feasible at undulator based sources. By orienting the splitter and the crystals of the lower branch to reflect a slightly[4] different wavelength relative to the upper branch yields 3 pulses of different wavelength

[4]The difference between wavelengths must be larger than angular acceptance of the crystal but smaller than the bandwidth of the incident fundamental radiation

and delay times (see figure 2.8). Since the harmonic radiation is transmitted through all crystals, it is recorded always at the same time, which can be used as a reference for time calibration of the other two branches.

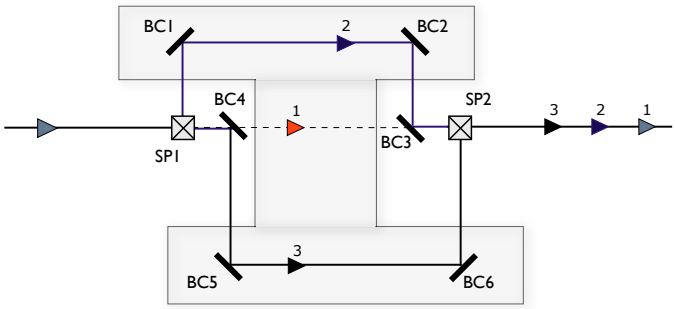

Figure 2.8: Scheme for 'three-color' time delay experiments with the two-branch configuration.

2.4 Crystal optics

The optical components of the delay unit should guarantee first of all high transmission, a wide energy tuning range and good thermal stability. Silicon and diamond are currently the most promising materials for optical components which might fulfill the aforementioned requirements for XFEL sources. Comparing silicon and diamond, the thermal and reflection properties of diamond are superior. The peak reflectivity of diamond is slightly higher and the absorption length μ is larger. This implies that less heat per unit volume is absorbed which makes diamond better suited for high power X-ray beams. Table 2.1 summarizes the thermal properties of silicon and diamond.

Despite of these superior properties of diamond, silicon is the preferred candidate in this early design stage. This is because silicon is available as an almost defect-free perfect crystal in suitable quality and size, which is not the case for diamond. The perfection of diamond crystals is presently not sufficient to perform experiments without distorting the wavefront. Furthermore, silicon can be

Table 2.1: Thermal properties of silicon and diamond crystals. Materials with low lattice expansion α and high thermal conductivity κ can achieve good performance (i.e. preserving the Darwin width) even at high heat load conditions. The absorption coefficient is denoted as μ.

	Silicon	Diamond
μ (8.4 keV) [μm^{-1}]	0.01258	0.001768
α at 300K [$1/K$]	$2.62 \cdot 10^{-6}$	$0.8 \cdot 10^{-6}$
κ at 300K [W m^{-1}K^{-1}]	160	3500

machined into different complex shapes. As will be shown in the next section, this feature is of particular importance for designing an X-ray beam splitter.

It was shown at the beginning of the chapter that the concept of 90 degree scattering geometry allows one an easy change of the delay time by simply translating four Bragg crystals. On the other hand, this concept imposes certain requirements on the delay line optics. Namely, all crystals have to be aligned to the Bragg angle of 45 degrees.

For silicon with unit cell dimension $a = 5.43$ Å, the lattice spacing d_{hkl} is given by

$$d_{hkl} = \frac{a}{\sqrt{h^2 + k^2 + l^2}} \tag{2.11}$$

The appropriate Miller indices are found by using the Bragg equation and expression (2.11). The expected Bragg reflectivities from a crystal with various hkl are calculated with the XOP 2.11 package [24] assuming an ideally perfect crystal and a monochromatized divergence free beam. The Darwin width, reflectivity and the integrated intensities obtained from the calculations are given in table 2.2.

The choice of the crystal reflections for optimal performance is based mainly on energy considerations. To perform experiments at an energy of about 8 keV with undulator radiation, the Si(511) reflection was selected. The reflection has a high peak reflectivity i.e $R_{max} = 0.89$ and Darwin width $\omega_0 = 8.58$ μrad, which is

Table 2.2: Energy, Darwin width ω_0, reflectivity and integrated intensity of various crystal reflections diffracted at the dynamical Bragg angle of 45° in symmetric scattering geometry.

hkl	Energy	Darwin width		$\Delta\lambda/\lambda$	Reflectivity	Integrated intensity [a.u.]
	[keV]	[μrad]	[arcsec]	[10^{-6}]	R_{max}	$\int_{-\infty}^{\infty} R(\theta)d\theta$
333	8.388	8.29	1.71	8.29	0.89	1.93
440	9.132	9.26	1.91	9.26	0.96	2.21
444	11.184	4.84	1.00	4.84	0.96	1.21
511	8.388	8.58	1.77	8.58	0.89	1.92
531	9.550	5.72	1.18	5.72	0.91	1.35
533	10.586	4.12	0.85	4.12	0.91	0.99
551	11.528	3.10	0.64	3.10	0.91	0.75
553	12.400	2.33	0.48	2.33	0.92	0.57
711	11.528	3.10	0.64	3.10	0.91	0.75
731	12.400	2.33	0.48	2.33	0.91	0.57
800	12.914	2.81	0.58	2.81	0.95	0.71

comparable to the typical vertical divergence of 3rd generation undulator sources[5].

The Si(553) reflection was chosen for performance tests of the delay unit optics at 12.4 keV at the PETRA II storage ring[6]. Although the Darwin width is only $\omega_0 = 2.33$ μrad, it allows one to test the limits of the mechanics employed in the delay unit. One should note that this reflection is also well suited for the European XFEL beam in terms of energy and divergence[7]. The calculated reflection curves of the chosen reflections are shown in figure 2.9.

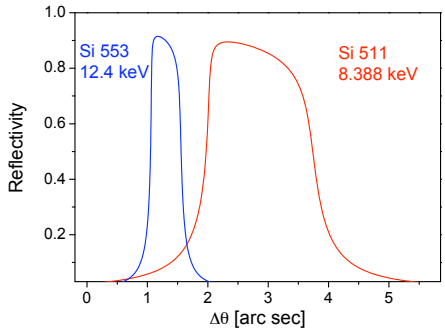

Figure 2.9: Calculated rocking curves of Si(511) at E = 8.388 keV(red) and Si(553) at E = 12.4 keV(blue) for the symmetric Bragg geometry.

2.4.1 X-ray beam splitter

A beam splitter is an optical device that allows one to split a beam i.e. reflect one part of the beam and transmit the other part. A well known example of a beam splitter is the Michelson interferometer, in which laser light is split and recombined by a semitransparent mirror. Currently available splitters work at a wide range of wavelengths down to the hard X-ray regime [25–28]. In order to choose the right beam splitter various splitting schemes are presented here.

[5]The vertical divergence of the ID10C undulator at ESRF is 3.5 arcsec (17 μrad)

[6]The minimum accessible energy at the beamline PETRA 1 of PETRA II storage ring is 12.4 keV

[7]The expected divergence for the European XFEL SASE2 is 0.84 μrad. At least one undulators of the European XFEL will be optimized for 12.4 keV [10].

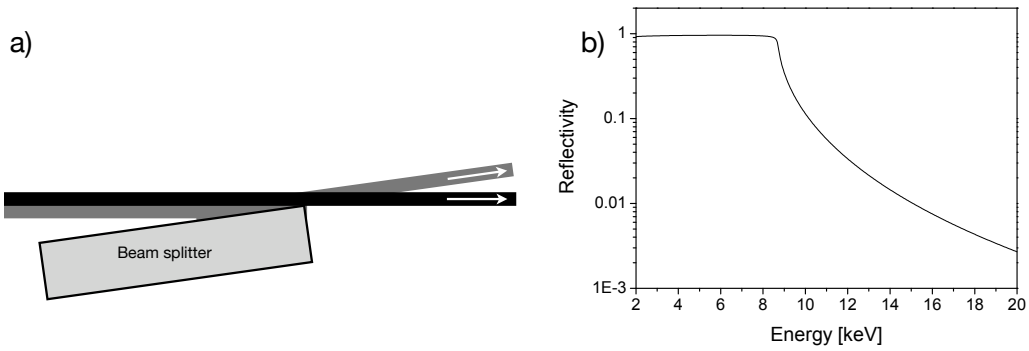

Figure 2.10: a) X-ray mirror as a possible beam splitting scheme for hard X-ray radiation. b) Reflectivity from a silicon mirror calculated for the energy range 2 - 20 keV at incident angle θ_i=0.2°.

2.4.1.1 Mirror beam splitter

The main requirement for an X-ray beam splitter is to redirect the beam into two directions with the smallest possible absorption. Very efficient splitting of X-ray beams can be achieved by utilizing an X-ray mirror. Figure 2.10a shows a scheme of this kind. The incoming lower part of the X-ray beam is reflected from the upper part of the splitter. The upper part of the beam propagates unaffected. The angle of incidence below which total external reflection of X-rays occurs is given by

$$\theta_c = \sqrt{4\pi\rho r_e}/k \tag{2.12}$$

where the wavevector $k = 2\pi/\lambda$, and ρ is the electron density.

From equation (2.12) one can find that total external reflection from the mirror surface demands very small incident angles. Figure 2.10b shows the reflectivity of a silicon mirror at $\theta_i = 0.2°$ calculated for various energies. Below 9 keV the reflectivity of the silicon mirror is close to unity and therefore the overall throughput of the splitter is very high. However, due to the very small reflection small angle the separation of the beam is also very small. For $\theta_i = 0.2°$ two beams are separated only by 1 m after a distance of 143 m. Achieving significant delay times in this way is very inefficient and would require the construction of a very large experimental setup. Furthermore, to reflect energies higher than 9 keV

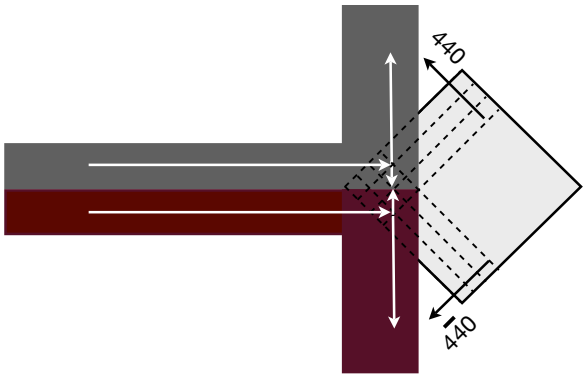

Figure 2.11: Rhombic-shape perfect crystal as a beam splitting device for hard X-rays.

the incident angle must be further decreased. The critical angle can be shifted to larger values by coating the surface of the mirror by a material with a higher electron density or using X-rays with longer wavelengths. A splitting scheme with a deflection angle of 3° was recently proposed for soft X-rays [15]. An intrinsic problem for this splitting scheme might arise from the diffraction effects caused by the edge of the mirror.

2.4.1.2 Rhombic-shape crystal beam splitter

Another approach for splitting soft X-ray beams by a mirror was proposed by Feldhaus et al. [29]. In this concept the beam is split by the two faces of a rhombic-shape SiC mirror at reflection angle of 45°. This optical geometry can be transposed to hard X-rays employing the three beam case of Bragg optics [30]. Due to the high symmetry of silicon more than one set of lattice planes can reflect an X-ray beam simultaneously. At E = 9.132 keV the two sets of Bragg planes; (440) and ($4\bar{4}0$), are excited[8] simultaneously giving rise to two Bragg reflected beams. Figure 2.11 shows a scheme for three beam case splitting with a rhombic-shape Si(440) perfect crystal. The crystal serves as a beam splitter diffracting the upper part of the beam upwards and the other part in opposite direction.

[8] in order to excite both reflections it is required that the incident beam has a divergence (and energy spread) larger than the angular (and energy) acceptance of the splitter. This condition is caused by the refraction of X-rays.

Due to the multiple diffraction in the crystal the proposed scheme will have a low efficiency. To further limit absorption losses, the edge between two reflecting surfaces of the crystal must be manufactured with a very high precision. Due to the polarization of X-rays the proposed 90° scattering scheme should work in vertical geometry.

2.4.1.3 Laue crystal beam splitter

A perfect crystal oriented in symmetric Laue geometry is one of the approaches that has been proposed and successfully applied to split the beam in hard X-ray interferometers [31]. A convenient prototype splitter for a delay unit could be a perfect silicon crystal cut in Laue geometry. Figure 2.12a shows the schematic layout of a Laue X-ray splitter. The incident beam generates 2 wavefields in the crystal, that follow different paths. In the Laue diffraction geometry both traveling waves interfere with each other. At the exit surface both wavefields redistribute into two X-ray beams: the forward diffracted I_{fd} (with the momentum parallel to the incoming beam) and the Bragg reflected I_r.

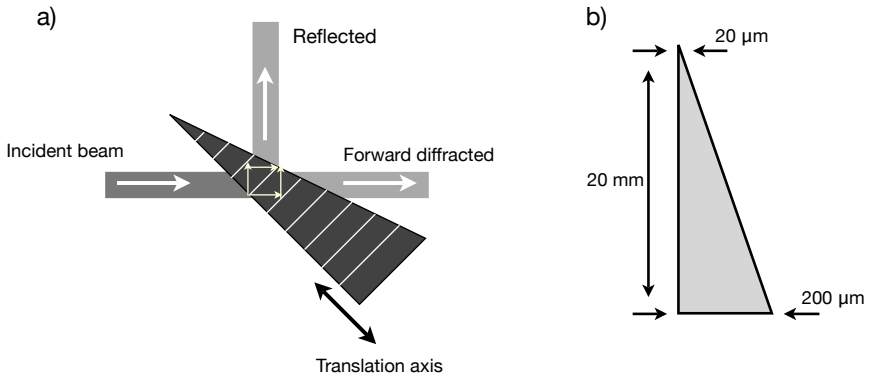

Figure 2.12: Schematic layout of the X-ray beam splitter. a) A crystal oriented in Laue diffraction geometry. By moving the crystal along the translation axis different thicknesses of the crystal are probed. b) Proposed dimensions of the beam splitter used for the experimental procedure in this work.

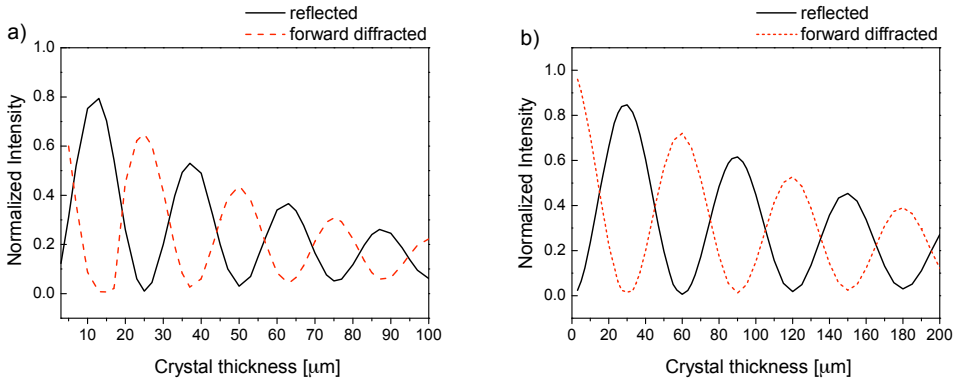

Figure 2.13: Pendellösung fringes. Variations of reflected (solid line) and forward diffracted (dashed line) intensities as a function of the beam splitter thickness at $\Delta\theta = 0$. Calculations performed for symmetric Laue geometry of a) Si(511) at E = 8.388 keV and b) Si(553) at E = 12.4 keV.

An important property of the splitter is its ability to control the intensity ratio of the two diffracted beams, $R_s = I_r/I_{fd}$. For different experiments different schemes of splitting have to be applied. The 'split-pulse' XPCS technique (cf. section 1.3) requires two equal intensity split pulses for autocorrelation measurements. For 'pump-probe' experiments the excitation of the sample is produced by the first very intense pulse (i.e. the *pump*) and the evolution of the process is observed by the second much weaker pulse (i.e. the *probe*). Thus, a different ratio of pulse power between both split pulses is demanded. To tune the ratio of intensities R_s the beam splitter could be wedge shaped. Proposed dimensions of the splitter are given in figure 2.12b. With an apex angle of 15.7 μrad and a height of 20 mm the thickness of the crystal, probed by the X-ray beam, can be continuously varied from the top to the bottom by moving the crystal along the translation axis, as depicted in figure 2.12a.

Figure 2.13a shows calculated[9] variations of the intensities of the forward diffracted and Bragg reflected beams at $\theta_B = 45°$ as a function of the crystal thickness. The splitting capability of the crystal depends on the ratio of the

[9]the calculations are based on the plane wave theory.

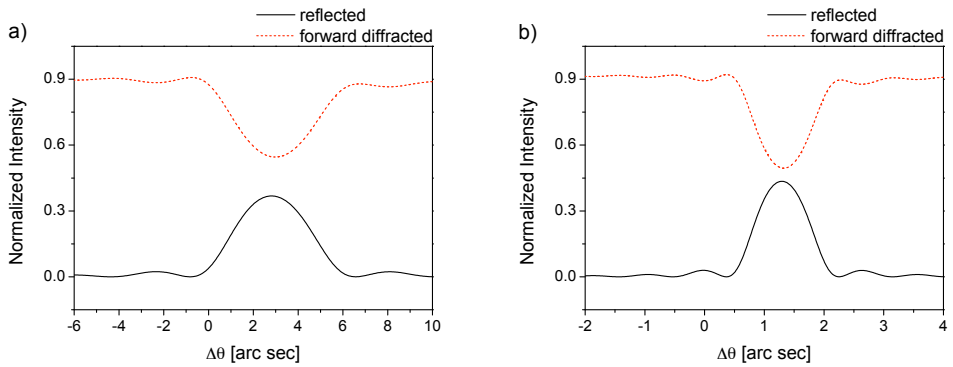

Figure 2.14: Variations of reflected (solid line) and forward diffracted (dashed line) intensities as a function of $\Delta\theta = \theta_i - \theta_B$, where θ_i is incident angle and $\theta_B = 45°$. Calculations performed for symmetric Bragg geometry for a) Si(511) at E = 8.39 keV at crystal thickness $t = 6$ μm and b) Si(553) at E = 12.4 keV $t = 16$ μm.

beam splitter thickness t to the Pendellösung period Λ_L, as illustrated in figure 2.13. At E = 8.388 keV the Si(511) reflection yields Λ_L of 26.6 μm. Probing the crystal at a thickness corresponding to $n\Lambda_L/4$, where n is a positive odd number yields equal intensity splitting. It can be seen that the splitting ratio close to $R_s \approx 1$ is achieved at thickness of $3\Lambda_L/4 = 20$ μm. The maximum intensity ratio corresponds to the crystal thickness of $\Lambda_L/2$. At the thicker part of the crystal the efficiency of the splitter decreases due to increasing absorption. A thin crystal with the thickness up to half of Λ_L (i.e. 13.3 μm) would provide the best splitting conditions for pump - probe studies. The ratio of diffracted intensities increases and the losses due to absorption are minimized.

2.4.1.4 Bragg crystal beam splitter

A Bragg crystal with a thickness smaller than the extinction length can also serve as a beam splitter. An advantage of using a Bragg crystal as the delay unit beam splitter is the exact 90° scattering geometry. However, the thickness of the beam splitter has to be much smaller compared to the Laue case, which causes constrains for the manufacturing process. Figure 2.14a shows intensities I_r and

I_{rd} as a function of relative incident angle $\Delta\theta$ calculated for a 6 μm thick Si(511) Bragg crystal. A splitting ratio R_s close to 1 is achieved. Similar calculations for the Si(553) Bragg crystal gives $R_s = 1$ at $t = 16$ μm.

2.4.1.5 Choice of the delay line beam splitter

For the proposed concept of the delay unit a wedge shaped Laue crystal has been chosen to split the X-ray beam. To support this choice it is worthwhile to summarize the aforementioned splitting schemes. The highest splitting efficiency can be achieved with a mirror beam splitter, however, the accessible maximum delay times are limited by the low scattering angle of the mirror. In case of the rhombic-shaped crystal, the splitting efficiency is affected by the absorption of X-rays reflected inside the crystal into opposite directions. Laue and Bragg beam splitters are certainly the most promising concepts. However the utilization of a Bragg geometry imposes manufacturing a very thin crystal. Fabricating a crystal with a thickness below 10 μm without inducing deformation in the crystal lattice is still a challenge nowadays. The extinction length in a Laue crystal is longer than in Bragg case, therefore the required thickness of a Laue beam splitter is larger. It should be noted that choosing a Laue crystal as the delay unit beam splitter affects the scattering path inside the delay unit. The effect of the beam splitter geometry on the path of the X-ray beam inside the delay unit is discussed in detail in the next section. It is also important to note, that the proposed delay unit concept is also valid with Bragg beam splitters and can be realized as soon as such crystals become available.

2.4.1.6 Laue vs Bragg beam splitter

The choice of the Laue crystal as a beam splitter slightly modifies the proposed 90° scattering geometry (cf. section 2.3) affecting the incident beam conditions of pump-probe and correlation spectroscopy experiments. The consequences of using Laue beam splitters on the conducted experiments is discussed in this section.

It is known from dynamical theory that the difference between the dynamical and kinematical Bragg angle varies with energy and asymmetry. Using expres-

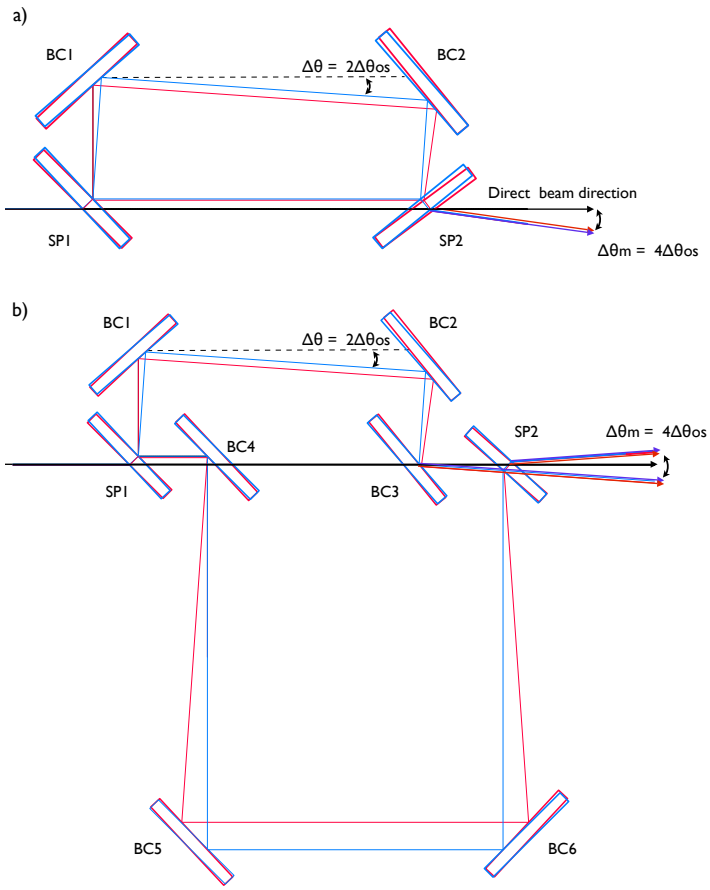

Figure 2.15: Expected X-ray paths inside the delay unit arranged in a) the one-branch and b) the two-branch configurations. The delay unit optics is aligned to the dynamical (blue line) and kinematical (red line)Bragg angles. Note that the two exit beams do not propagate symmetrically to the incident beam axis. Note also that the beamsplitting Laue crystal is a wedge shaped thus implying $\Delta\theta \neq 0$.

sion (2.5) one can find that at an energy of 8.388 keV and for the symmetric Laue and Bragg geometries this difference is 0 and 13.6 μrad, respectively. Since the delay unit optics consists of Laue beam splitters and Bragg reflectors the beam path will not follow exactly the 90° geometry shown in figure 2.4.

Figure 2.15a shows the expected X-ray paths in the one-branch delay unit configuration. The blue and red lines represent the delay unit optics aligned to reflect the energies corresponding to the kinematical and dynamical bragg angles, respectively. It is evident from the figure that in neither of the two cases the

delayed beam downstream of the delay unit follows the direction of the incident X-ray beam. The expected angular mismatch between the delayed and direct beams is $\Delta\theta_m = 4 \cdot \Delta\theta_{os}$, which in the case of Si(551) optics is 54.5 μrad. At higher energies the effect of refraction is weaker, therefore $\Delta\theta_{os}$ is smaller. For the Si(553) optics (at energy of 12.4 keV) $\Delta\theta_{os} = 6.3$ μrad and consequently $\Delta\theta_m =$ 24.9 μrad. Similar analysis for the two-branch configuration yields the same value of angular mismatch between the two delayed beams. This is illustrated in figure 2.15b.

The directional mismatch of the delayed beams can be of advantage or disadvantage depending on the experiment taking place downstream the delay unit. For XPCS experiments the co-linearity of two beams downstream the delay unit is important since the same sample volume need to be illuminated. Otherwise the two pulses probe dynamics attributed to slightly different volumes of the sample. When $\Delta\theta_m$ is larger than the angular width of the speckle size, the two pulses will produce two different speckle patterns (for a static sample). On the other hand, the angular offset creates a possibility to eventually probe the dynamics of the sample with two detectors, each dedicated for one beam. In this way the correlation functions can be measured separately. In this arrangement both 'split-pulse' and 'sequential' modes are accessible during XPCS experiments.

In case of measurements of the delay time for diagnostics purposes, e.g. with an ultra-fast time resolving detector located right behind the second beam splitter, the mismatch should not affect the precision of the measured delay as long as the both beams arrive at the detector position within its active area.

The are several ways to compensate for the angular mismatch. For instance, the BC3 and SP2 crystals could be titled to deflect the beam slightly in the horizontal plane[10] minimizing the angular offset. The beam can be recombined back horizontally with a help of tilting the BC2 and BC6 crystals. To minimize the angular mismatch one can also utilize other (more complicated) delay unit schemes, which are discussed in chapter 5. Another way would be to change the

[10] as it will be shown in chapter 4 the procedure of minimizing the offset with the help of crystal tilts was successfully applied to achieve collinear beams behind the delay unit.

lattice spacing d_{hkl} of the beam splitters by varying the temperature of the Laue beam splitters. The temperature difference ΔT of 0.5 K should be sufficient to match the scattering angle of the beam splitters to the ones of the Bragg crystals. Using asymmetric[11] Bragg reflection is another way to shift the Bragg scattering angles in a such way that both beams become co-llinear behind the delay unit. As mentioned before, replacing the Laue beam splitters with very thin Bragg crystals will also bring the two exit beams on the same path. As one can see there are ways to compensate the angular mismatch of the two exit beams, however some of them would require a further development of the delay unit's basic concept.

2.4.1.7 Pulse broadening

XFEL sources [1, 2] will typically provide 100 fs long pulses that are ideal for investigating ultra-fast dynamics. Since the delay unit employes perfect crystal diffraction, the influence of the delay unit optics on the pulse duration has to be taken into account. Due to a relatively small energy acceptance of the Si(511) reflection at 8.39 keV (i.e. $\Delta E = 72$ meV) pulse broadening will occur after the reflection. It was suggested by [32] that the pulse duration can be estimated via uncertainty relation $\Delta E \cdot \Delta t/(2.35)^2 \gtrsim \hbar$ yielding for $\Delta E = 72$ meV the transient reflection to last more than 23 fs. For the Si(553) reflection at 12.4 keV $\Delta E = 23$ meV and therefore a longer time response is expected i.e. 65 fs. In this calculations the incident pulse is considered as a δ-function. The results are confirmed by computer simulations of a XFEL pulse reflected from the Si(111) and Si(444) crystals[32, 33]. In agreement with the uncertainty relation a wider broadening was found for the higher index reflection. Furthermore the time response of pulses passing a (non-dispersive) double crystal arrangement is more pronounced than observed for single bounce reflections. This result is of importance for the delay unit, which utilize up to 4 crystal reflections per branch and therefore a significant pulse broadening can be expected.

[11] asymmetric reflections affect not only the scattering angle but also the beam size and divergence. The use of such reflections in the delay unit can minimize the angular offset but it might also affect the throughput of the device.

2.5 Expected performance of the delay line optics

The performance of any beamline component can be defined by two essential parameters, namely throughput and stability. The first one defines how well the optical components transmits X-rays under stable conditions. It is usually defined by

$$T = \frac{I_1}{I_0} \tag{2.13}$$

where the I_1 and I_0 are outgoing and incoming beam intensity, respectively. For the ideal optical component T equals unity, however, due to absorption this value will always be lower. When the optical element is a perfect crystal, the properties of the X-ray beam such as relative energy bandwidth, divergence and the width can be modified. An elegant approach to discuss these modifications is known as the DuMond diagram method [34]. The DuMond description is a graphical method that permits to understand X-ray properties of not only one but a series of optical elements. In the diagram the horizontal axis represents an angular variable $\Delta\theta$ and the vertical axis is given by the wavelength λ. In a 3D visualization of the diagram the third axis would represent the intensity.

Since the delay unit utilizes Bragg and Laue crystals in various arrangements the corresponding DuMond diagrams are calculated. The overall device performance is discussed first by analyzing properties of Laue and Bragg geometries. Next, the discussion is extended to double crystal arrangements and analyzed separately for the upper and the lower branch of the delay unit. Finally the expected throughput is calculated using ray tracing [35].

Figure 2.16 shows the DuMond diagram of the Si(511) reflection in symmetric Bragg geometry. The diagram is composed of two parts. The left one corresponds to the incoming beam and represents a plot of λ as a function of $\Delta\theta_i = \theta_i - \theta_B$, where θ_i is incident angle. The right part of the diagram corresponds to the outgoing beam and is represented by the plot of λ vs $\Delta\theta_e = \theta_e - \theta_B$, where θ_e is the exit angle. The width of the black vertical bar along the horizontal axis in figure 2.16a(left) corresponds to the divergence of X-ray source. The red curve is a graphical representation of Bragg's law calculated for the wavelength

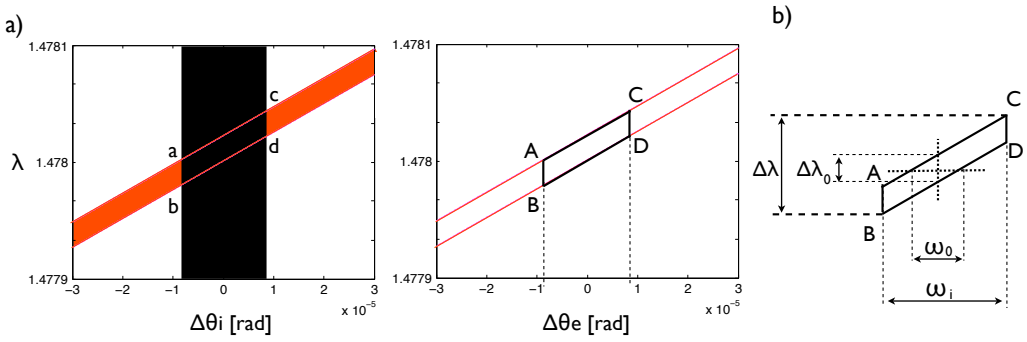

Figure 2.16: a) DuMond diagram for Si(511) perfect crystals in symmetric Bragg geometry at $\lambda = 1.4078$ Å. The width of the vertical black bar represents the divergence of the incident beam. b) Details of the diagram illustration that the angular width of the reflection is determined by the incident beam divergence ω_i.

spread $\Delta\lambda$ centered at $\lambda = 1.4781$ Å. The breadth of the Bragg curve along $\Delta\theta_{i,e}$ is the Darwin width ω_0, as depicted in figure 2.16b. The DuMond ordinate λ expresses the wavelength band accepted by the reflection. For perfectly collimated polychromatic incident beam its value is related to the intrinsic bandwidth of the crystal $\Delta\lambda_0$, defined as :

$$\Delta\lambda_0 = \omega_0 \cdot \cos\theta_B \cdot 2d_{hkl} \tag{2.14}$$

According to the DuMond approach the crystal accepts the radiation in the region abcd, where the reflection band intersects with the source divergence and transmits it to ABCD. The region inside ABCD has a reflectivity close to 1 while the regions outside have zero reflectivity. For the Si(511) reflection in the Bragg case the reflectivity $R = 0.89$ and the transmitted intensity is proportional to the area depicted by the parallelogram ABCD.

For polychromatic radiation with the finite divergence ω_i the wavelength bandwidth $\Delta\lambda$ and the exit divergence ω_e of the beam reflected from a perfect crystal

is defined as [23]:

$$\Delta\lambda = (\omega_0 + \omega_i) \cdot \cos\theta_B \cdot 2d_{hkl} \tag{2.15}$$

$$\omega_e = \omega_0 \cdot |1 + b| + \omega_i \tag{2.16}$$

It is often very convenient to represent the crystal monochromatization in terms of relative wavelength bandwidth, which can be derived from expressions (2.1) and (2.15) into:

$$\frac{\Delta\lambda}{\lambda} = \frac{(\omega_0 + \omega_i)}{\tan\theta_B} \tag{2.17}$$

According to expression (2.16) the exit divergence ω_e reflected in the symmetric Bragg geometry ($b = -1$) equals ω_i, i.e. the incident divergence. Moreover, the reflection band on the incident side maps exactly the reflection band on the exit side, which is a unique property of the symmetric Bragg geometry.

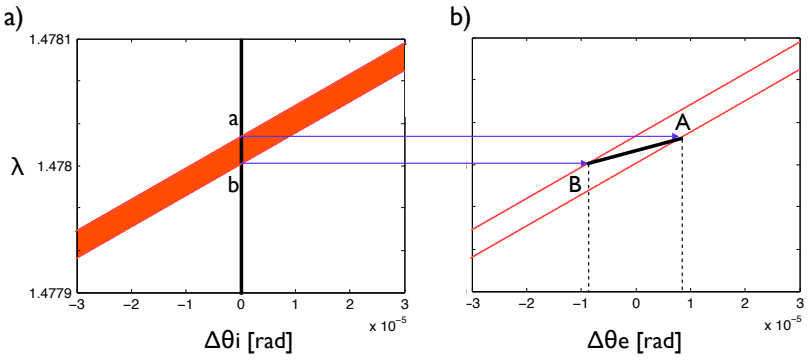

Figure 2.17: DuMond diagram for a perfect Si(511) crystal in symmetric Laue geometry for a perfectly collimated polychromatic source. a) and b) correspond to the incident and outgoing beam, respectively.

This is not the case for the symmetric Laue geometry ($b = 1$). The difference is clear from figure 2.17, which shows a DuMond diagram of the beam splitter crystal at SP1 diffracting perfectly collimated beam. The crystals behaves like an optical prism dispersing wavelengths into angles. Due to this angular disper-

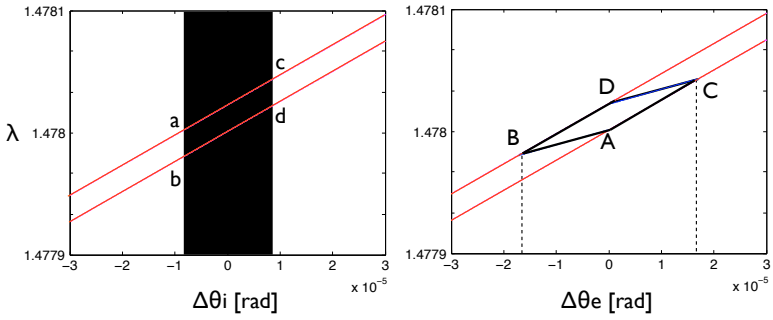

Figure 2.18: DuMond diagram for a perfect Si(511) crystal in symmetric Laue geometry. The vertical black bar represents the vertical divergence of the source.

sion [23] the exit divergence of the beam reflected from the symmetrically cut Laue crystal is much beyond the incident divergence ω_i. According to equation (2.16) the exit divergence in this case equals $2\omega_0 + \omega_i$. For $\omega_i = 17$ μrad and the Darwin width[12] $\omega_0 = 8.8$ μrad the exit divergence is $\omega_e = 34.7$ μrad (see figure 2.18). It is clear that the use of crystals in Laue geometry will lead to a degradation of the brilliance[13] of highly collimated polychromatic radiation unless other downstream optical components will regain the losses. This effect is negligible for purely monochromatic or divergent beams, as demonstrated later in figure 2.23.

The SP1 Laue beam splitter is the first crystal of the delay unit. Following the X-ray path of the upper branch, one can notice that the symmetric Bragg crystal BC1 accepts the radiation enclosed by ABCD from the crystal SP1, shown in figure 2.19, and transmits it preserving the wavelength band and divergence.

Crystals BC1 and BC2 shown in figure 2.20b are arranged in the so called (+n,+n) anti-parallel or dispersive setting [36]. The DuMond diagram of this crystal setting is illustrated in figure 2.20a. For a fixed position of the BC1 and BC2 crystals the bandwidth $\Delta\lambda$ and the angular width are determined by the Darwin width and are independent[14] of the incident divergence ω_i.

[12] Darwin width of Si(511) at E = 8.388 keV
[13] brilliance is defined as photons/sec/mrad^2/mm^2/0.1%bandwidth
[14] when the incident divergence is larger than the Darwin width.

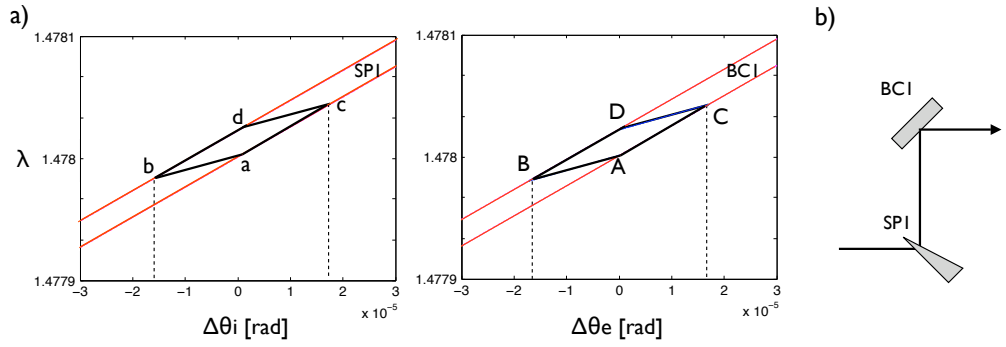

Figure 2.19: a) DuMond diagram of the SP1 - BC1 crystals. b) The SP1 - BC1 crystal arrangement.

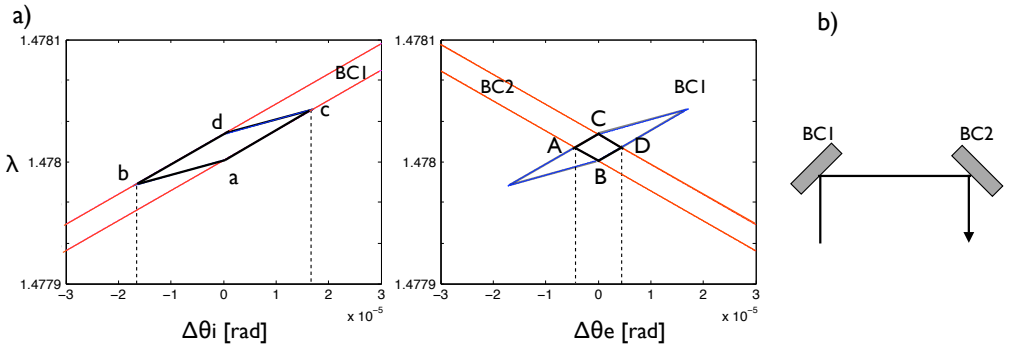

Figure 2.20: DuMond diagram of the dispersive BC1 - BC2 crystals setting. b) The corresponding arrangement of crystals.

The arrangement of the BC2 and BC3 crystals, shown in figure 2.5, is non-dispersive (+n,-n)[15], meaning that the bandwidth and wavelength spread will be conserved before and after the BC3 crystal. The expected DuMond diagram is shown in figure 2.21.

Before discussing the performance of the lower branch it is worthwhile to summarize the findings of the above DuMond analysis of the upper branch. The dispersive character of the beam splitter and the dispersive arrangement of the BC1 and BC2 crystals are the two effects that affect considerably the throughput

[15]The notation (+n,-n) was introduced by [37] and denotes the parallel setting of two identical reflections.

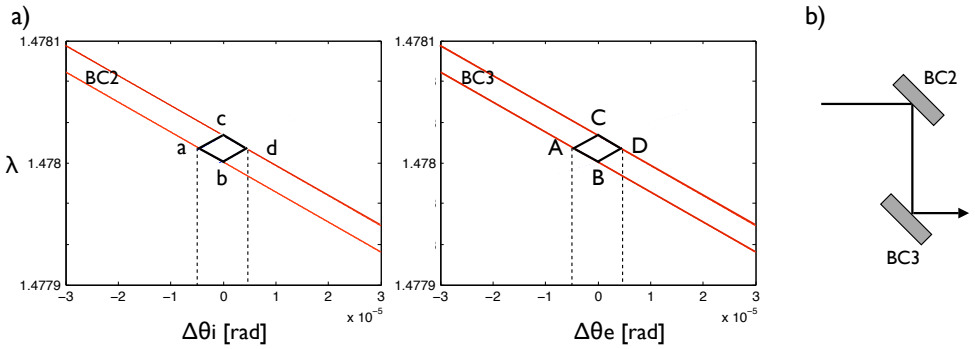

Figure 2.21: DuMond diagram of the non-dispersive setting of the BC2 - BC3 crystals. b) The corresponding arrangement of crystals.

of the upper branch. Since the divergence of the beam diffracted by SP1 is increased and then it is significantly reduced by the BC1 and BC2 arrangement, one can expect the lower throughput of the upper branch compared to optimally matched conditions[16]. Additionally, it should be noted that the divergence of the exit beam is defined by the Darwin width of the utilized Bragg optics. This is not the case for the beam transmitted through the lower branch.

Comparing both branches of the delay unit the same crystal arrangements can be found. Namely, the arrangements BC2-BC3 and BC1-BC2 in the upper branch corresponds to the BC4-BC5 and BC5-BC6 arrangement of the lower branch, respectively. Therefore, the DuMond diagrams of corresponding crystal configurations in the lower branch are expected to be the same as the ones in the upper branch. The only difference is related to the SP1-BC1 and BC6-SP2 crystal arrangements. Both crystal configurations utilize Laue and Bragg crystals, however, the order of scattering process is different. Namely, in the SP1-BC1 configuration the incident beam is diffracted first by the Laue crystal. The divergence and the wavelength spread is unaffected upon reflection from the BC1 crystal. This is not the case for the BC6-SP2 configuration. Figure 2.22 shows the corresponding DuMond diagram. Due to the dispersive behavior of the

[16] e.g. Bragg beam splitter and the non-dispersive arrangement of the BC2 and BC3 crystals.

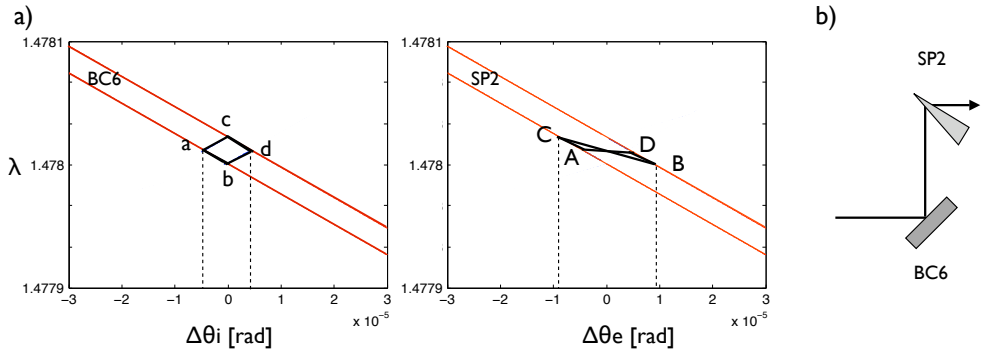

Figure 2.22: DuMond diagram of Bragg BC6 and Laue SP2 crystals. b) The corresponding arrangement of the crystals.

SP2 crystal a peculiar shape of reflection area occurs with a minimum intensity in the center of the reflection band. Additionally, the divergence of the beam transmitted through the lower branch is twice larger than the upper branch beam.

The performance of the delay line optics will vary depending on the used X-ray source. Figure 2.23 shows DuMond diagrams calculated for the Si(511) optics of the delay unit arranged in the two-branch configuration at the bending magnet beamline C at DORIS III, the undulator beamline ID10C at ESRF and

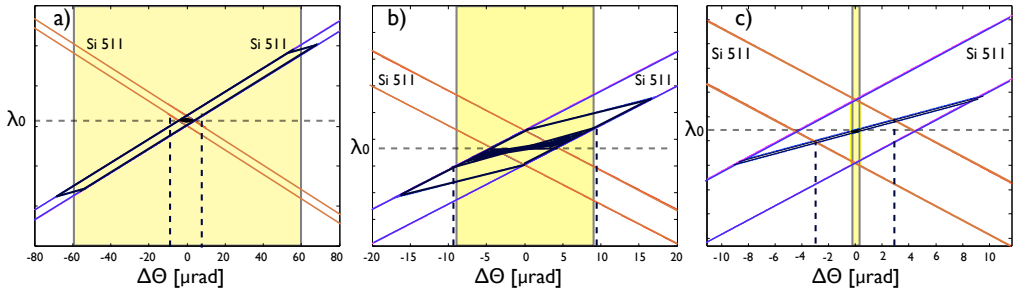

Figure 2.23: DuMond diagram illustrating the performance of Si(511) delay line optics with a bending magnet a) undulator b) and XFEL radiation c). The yellow area corresponds to the incident beam divergence and the wavelength spread. The vertical dashed lines represent the exit divergence of the photon beam behind the delay unit. Note different angular scales.

the European XFEL SASE2 [10]. As it is shown in figure 2.23a, the throughput of the delay unit with the bending magnet radiation is not optimal due to the large source divergence, which is more than one order of magnitude larger than the Darwin width. A much higher throughput can be expected at undulator based sources, since the source divergence is comparable to the angular acceptance of the delay unit optics. It is also evident from the DuMond diagrams that the effective increase in the exit beam divergence downstream the delay unit is the largest for the best collimated source. This effect is of importance for the XFEL source, which has a divergence of only 0.84 μrad. Since the radiation is not ideally monochromatic, it will be dispersed by the Laue SP2 crystal into an angular width of about 5.3 μrad at 12.4 keV.

Table 2.3 shows the expected throughput of the delay unit at 8.388 keV and 12.4 keV, respectively. The calculations were performed using ray tracing [35] assuming the monochromatic beam ($\Delta\lambda/\lambda = 1.4{\cdot}10^{-4}$) of the undulator beamline ID10C at ESRF and the European XFEL SASE2. The highest throughput of the delay unit with the Si(553) optics was found for the European XFEL source. This result is not surprising since the reflectivity of the Si(553) optics at E=12.4 keV is slightly higher than Si(511) at E=8.39 keV and the incident XFEL divergence is comparable to the Darwin width of the Si(553) reflection. In this case the delay line throughput is less sensitive to the dispersive crystal arrangements of the delay unit optics (i.e. BC1-BC2 and BC5-BC6 depicted in figure 2.5). As expected, the throughput value normalized to the energy acceptance of the delay

Table 2.3: The overall throughput T of the delay line in the two-branch configuration, calculated for monochromatized X-rays from undulator beamline ID10C and the European XFEL SASE2. T_{MEAS} corresponds to the throughput T normalized to the energy acceptance of the delay unit.

Source	Energy [keV]	T_{MEAS}	T
ESRF ID10C	8.388	0.024	$1.42 \cdot 10^{-3}$
XFEL SASE2	12.4	0.25	$4.14 \cdot 10^{-3}$

unit is also larger for the XFEL source.

Using very narrow reflections requires not only extremely high precision mechanics but also temperature stabilization of the optical components. Due to thermal expansion the interplanar spacing d_{hkl} varies with temperature:

$$\frac{\Delta d_{hkl}}{d_{hkl}} = -\alpha \cdot \Delta T \tag{2.18}$$

and consequently the Bragg angle changes according to:

$$\Delta\theta_B = -\alpha \cdot \Delta T \cdot \tan\theta_B \tag{2.19}$$

where α is the thermal-expansion coefficient for silicon (cf. table 2.1).

Using expression (2.19) for Si(511) one can find that a variation of temperature of $\Delta T = 1$ K results in $\Delta\theta_B = 2.42$ μrad (i.e. change of the Bragg angle at the given conditions). This change of the reflecting angle however is not significant ($\Delta\theta_B$ is 3.3 times smaller than the Darwin width) and temperature stabilization better than 0.8 K should be enough to maintain the Bragg condition. For the case of Si(553) optics the change of the Bragg angle is comparable to the Darwin width and stabilization better than 0.3 K is required. Another solution to the heat problem is the implementation of a feedback loop system that will react to temperature variations with crystal adjustments.

2.6 Summary

The concept of the delay unit for hard X-rays was introduced. The design of the optical components is based on perfect crystals cut in Bragg and Laue geometries. The device comprises up to eight crystals arranged in 90° scattering geometry. The pulse splitting is accomplished by a thin wedge shaped crystal oriented in Laue geometry. The delay unit optics employs Si(511) and Si(553) reflections implying operation of the device at 8.39 keV and 12.4 keV, respectively. Due to the polarization of X-rays the vertical scattering plane is used. The proposed design should be compatible with a variable delay time up to 2.84 ns. The expected

overall throughput will depend on the X-ray source. Due to the beam splitters, which disperse the collimated X-ray beam, the overall throughput at the XFEL SASE2 will be lower compared to the optimally matched conditions and the exit divergence of the beam downstream the delay unit will be increased beyond the incident beam divergence. The expected throughput of the delay unit at the XFEL SASE2 monochromatized to $\Delta\lambda/\lambda$ of $1.4{\cdot}10^{-4}$ is $4.1{\cdot}10^{-3}$.

Chapter 3

Experimental setup

This chapter presents a realization of the delay unit concept introduced in chapter 2. The description covers the crystal optics and the choice of mechanical and electronic components. A description of the beamlines, at which the device was commissioned is presented as well.

3.1 Crystal optics

The delay unit crystals were fabricated from a high quality silicon ingot cut in Laue and Bragg geometries. Figure 3.1a shows the delay unit beam splitter. The crystal has a wedged form (cf. section 2.4.1). To achieve a proper thickness variation from the top to the bottom of the crystal, it was etched in HF, HC_3COOH and HNO_3 solutions. The crystal foot has grooves on both sides that allow clamping the crystal to a holder. The basic dimensions of the splitter are given in figure 3.1b.

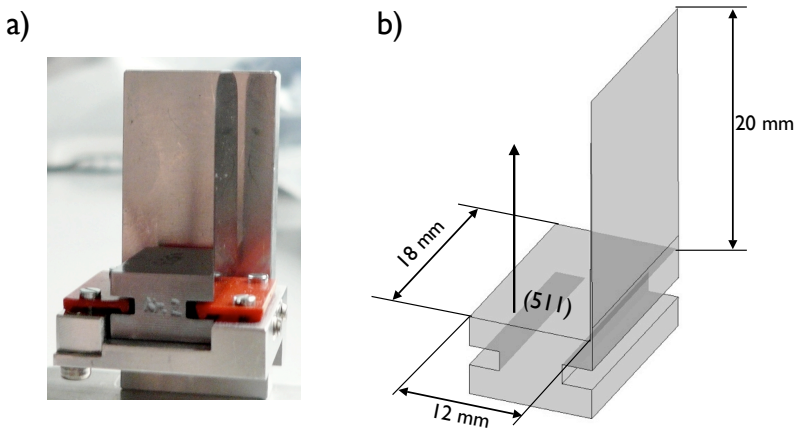

Figure 3.1: a) The Si(511) delay unit beam splitter mounted on a holder. b) Dimensions of the splitter.

The height of the wedge is about 20 mm and the size of the crystal base is 12 mm x 18 mm. Aligning the crystal to $\theta_B = 45°$ allows one to access only its upper part. The rest is blocked by the crystal foot.

Figure 3.2 shows the delay unit Bragg optics. Each crystal was cut into the shape shown in figure 3.2a. The surface of the crystal was etched and polished. The dimensions of the crystal are shown in figure 3.2b.

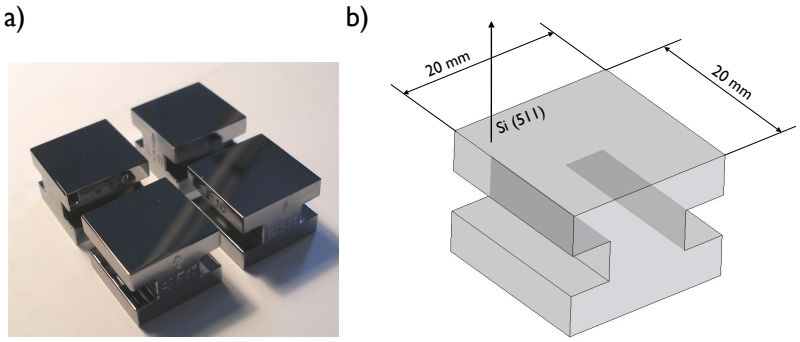

Figure 3.2: a) The delay unit Bragg crystals. b) Dimensions of the Bragg crystal.

3.2 Mechanical design

To implement the concept introduced in chapter 2 the delay unit must meet several mechanical requirements:

- The resolution of mechanical components of the delay unit optics must be better than the width of the crystal reflections. An angular resolution better than 8.6 μrad and 2.33 μrad is required at 8.388 kV and 12.4 keV, respectively.

- A change of the delay time is achieved by means of a simultaneous translation of the four Bragg crystals. The most straightforward way to do that is to place all 4 crystals on one translation stage. In this case the time delay range and resolution depends on the translation range and accuracy of the stage. Any mechanical inaccuracy will result in a loss of reflectivity and the necessity of realignment of the delay unit optics. Therefore, a translation stage with 1 μm resolution and a yaw below the reflection width is required.

- The entire delay line must be mechanically stable. Therefore a massive support for all mechanical components must be considered in the design.

- The two exit beams of the delay unit should ideally be combined and co-propagate. The accuracy for positioning the two beams should be better

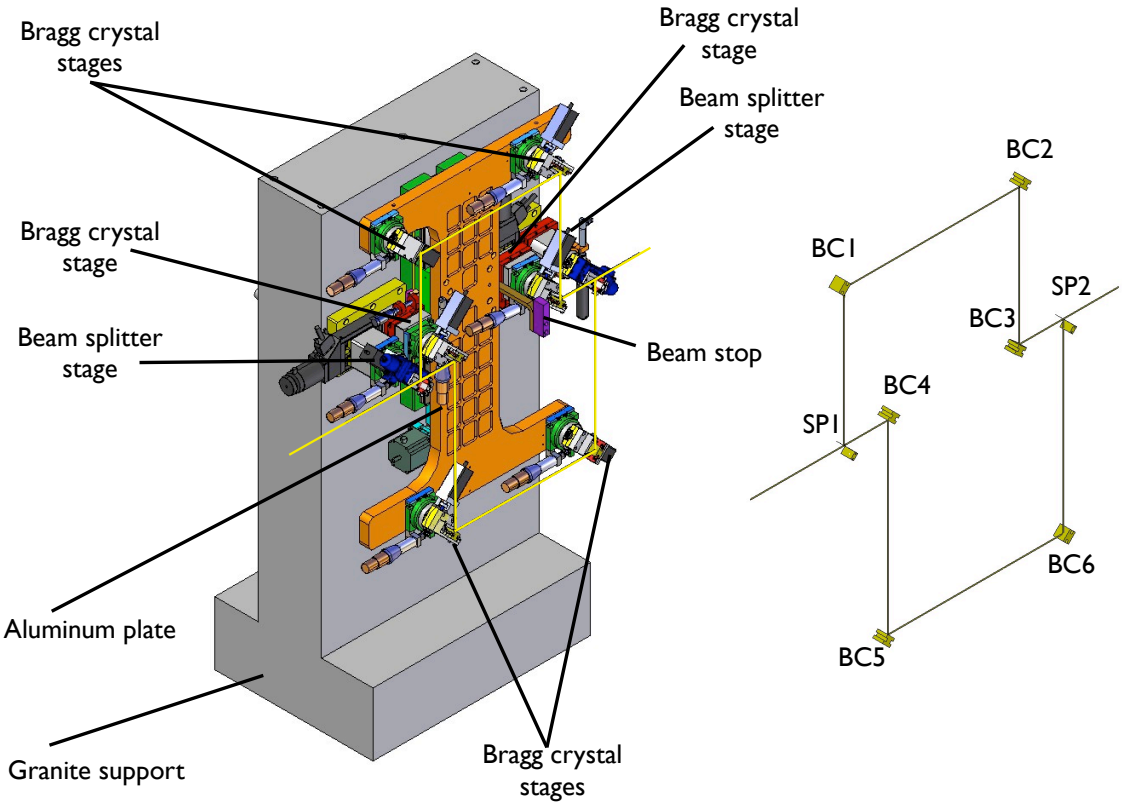

Figure 3.3: Left) Mechanical design of the delay line. Right) The x-ray path inside the delay line. The description of optical components was adapted from chapter 2.

than 1 μm.

- The overall dimensions of the delay unit line are of importance as well. The device should fit in the experimental hutches at various beamlines allowing to carry out performance tests at various sources. Therefore, the size of the device and maximum achievable delays should be optimized.

3.2.1 System overview

Figure 3.3 shows the technical realization of the delay line concept introduced in chapter 2. For clarity, the optical path of the X-ray beam inside the delay unit is also presented. The key components of the device are: Bragg and Laue beam splitter assemblies, aluminium plate, main translation stage and granite support.

Four Bragg crystal stages with crystals BC1, BC2, BC5, and BC6 are mounted on the aluminium plate, as shown in figure 3.6. The plate is mounted on the main translation stage, which is fixed to the massive granite support. The other four crystals; SP1, BC3, BC4 and SP2 are mounted on identical stages, that are fixed rigidly to the granite support.

3.2.1.1 Basic components

Figure 3.4 shows one of the Bragg crystal stages. The crystal is clamped from both sides to the holder and mounted on a motorized swivel stage (KOHZU SA04B-RT). In this way the beam path can be aligned to the vertical scattering plane. The angular range of the stage is $\pm 10^{\circ}$ with a resolution of 1.16 μrad.

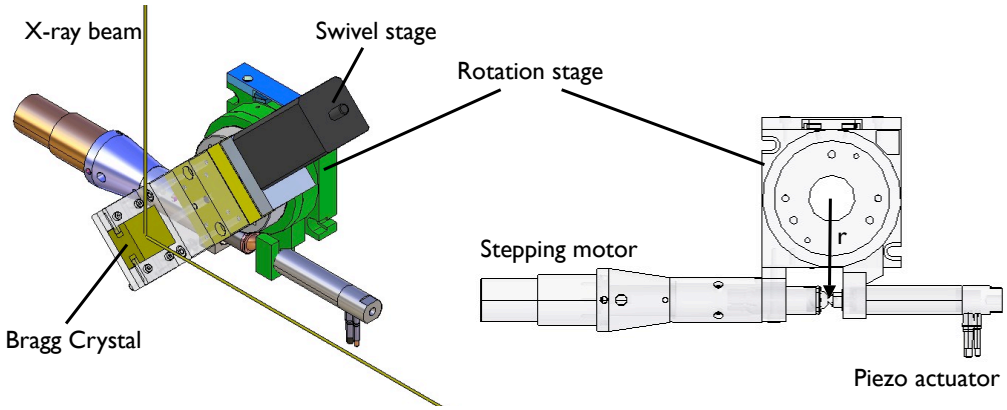

Figure 3.4: Left) Bragg stage assemble. Right) Tangent arm rotation stage.

In order to achieve the required angular resolution, the Bragg stage is equipped with a tangent-arm rotation stage (PI M-035). The angular motion of the stage is provided by linear actuators. The stage is equipped with a stepping motor providing 12 degrees of positioning range. Additional fine adjustment over ± 485 μrad is possible with a piezo actuator. In closed loop operation a resolution better than 1 μrad can be achieved. The displacement of Δx provided by the actuator is related to the angular motion $\Delta\alpha$ of the stage according to

$$\Delta\alpha = \arctan(\Delta x / r) \tag{3.1}$$

where r is the distance from the contact point of the actuator to the center of rotation. At the 0 degree position, which is depicted in figure 3.4(right), r is 44 mm. The common rotation center is located on the surface of the crystal, 10 mm from the edge.

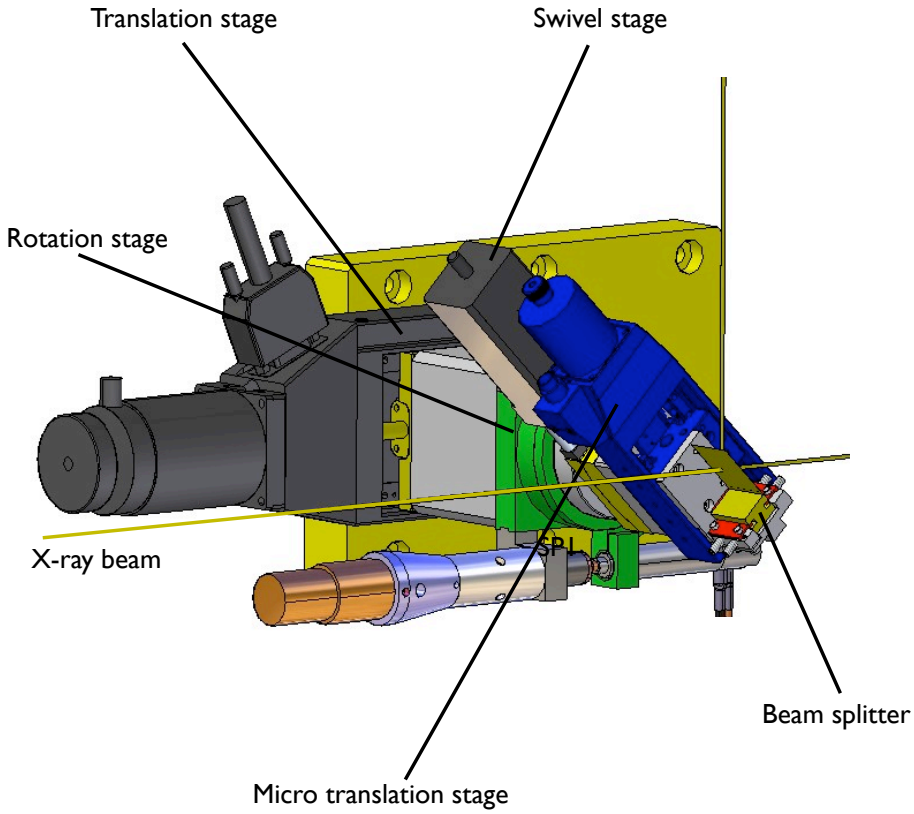

Figure 3.5: Splitter SP1 stage

The splitting of the incident radiation is achieved by a Laue crystal mounted on the beam splitter stage, shown in figure 3.5. The ratio of the splitting is adjusted with the micro translation stage (MICOS MT-40). A travel range of 26 mm gives an access to the top 9 mm of the crystal, allowing measurements of the strongest Pendellösung fringes. The micro stage is mounted on a high

resolution rotation stage and a swivel stage of the same type as in the Bragg crystal stage. The horizontal adjustment of the beam reflected by the splitter is achieved by a translation stage (MICOS MT-65), coupled rigidly to the granite.

The position of the beams downstream the delay unit is defined by the BC3 and SP2 crystal stages. The vertical alignment is achieved with stage BC3 mounted on a vertical translation (MICOS MT-65). The resolution of the stage is 0.25 μm. This defines the resolution of the vertical spatial beam overlap downstream of the delay unit. The large translation range allows one to separate the beams in the scattering plane by 12.5 mm.

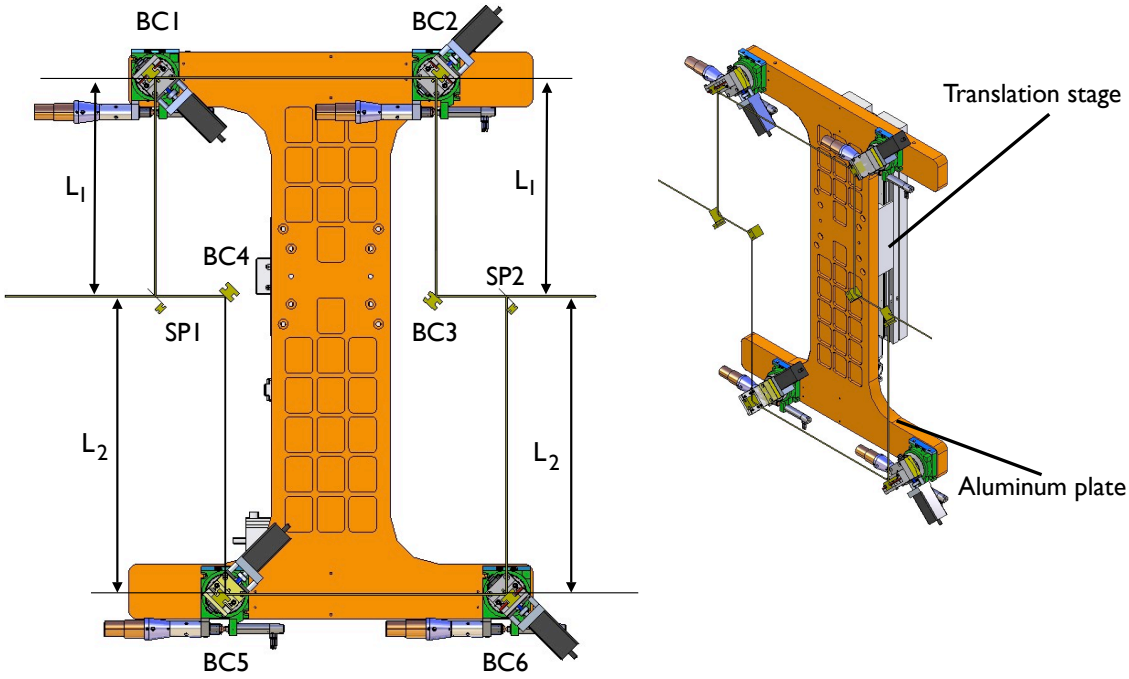

Figure 3.6: Left) The translation unit of the delay unit. Right) The aluminum plate.

Figure 3.6 shows the technical design of the translation unit. Four Bragg stages, mounted on the aluminum plate define the optical paths. The only variable distances between the crystals are L_1 and L_2. In the actual design, the minimum

value of L_1 and the maximum value of L_2 are 126 mm and 525 mm, respectively, giving a maximum delay path of 798 mm.

A change of the delay time is achieved by vertically moving the aluminium plate mounted onto a high resolution translation stage (HUBER 5101.30 - 300hp). The stage is a custom made translation, in which the yaw (i.e. the angular deviation from the straight motion of the translation in the scattering plane) was reduced at the expense of the other degrees of freedom, such as the pitch[1]. Moving the translation stage from position 0 to 200.5 mm changes the path difference from 798 mm to 0 mm. At this position the paths of the two branches have the same lengths $L_1 = L_2 = 326.5$ mm. It should be noted that in this position the translation is 50.5 mm from the middle position. The plate was mounted asymmetrically on the translation stage. In this way longer delay times can be achieved.

The design of the setup allows one to choose which of the split pulses arrives at the sample position first. Translating the plate to its maximum i.e. 300 mm, gives a path length difference of 402 mm. However, in this case, the position of the two pulses is reversed in time.

The intrinsic resolution of the stage is ± 10 μm. That translates into a minimum delay step of 200 fs. Using micro-stepping this value was improved to ± 0.5 μm. This yields a delay time step of ± 6.67 fs. The stage is equipped with an encoder system (Renishaw RGH24)[2].

The maximum load of the stage is limited to 18 kg due to the vertical geometry. This condition imposes tight boundaries on the choice of the components for the Bragg crystal stage and the thickness of the aluminium plate. The latter one was 25 mm and gave a proper stiffness of the plate. The total weight of the translation unit (except the translation stage) is below 14.5 kg.

[1] Angular deviation from the straight motion of a translation perpendicular to the scattering plane

[2] The resolution of the the encoder is ± 0.5 μm. It was not operational on during the experiments.

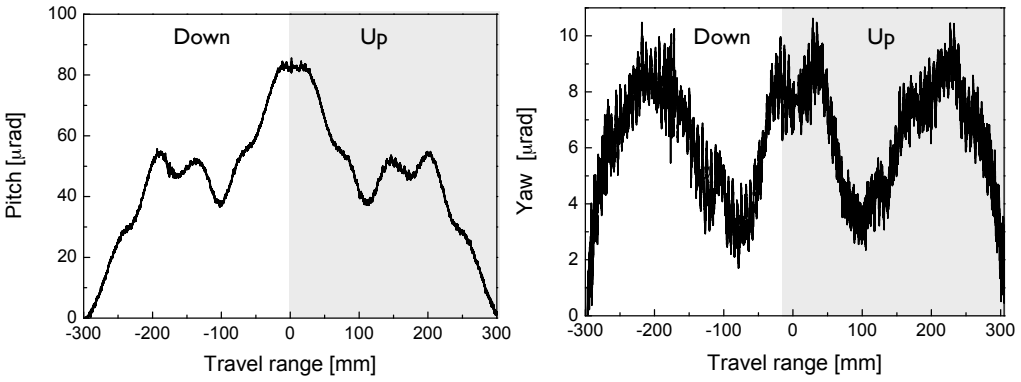

Figure 3.7: Pitch and yaw measurements of the translation unit performed with an autocollimator.

Although the mass distribution is not symmetric, optical metrology measurements showed that the translation unit has a yaw not larger than 10 μrad. Figure 3.7 shows the pitch and yaw deviations measured at the BC5 and BC6 positions with an autocollimator.

Figure 3.8 shows a 3D sketch of the complete delay unit assembly. In order to reduce temperature drifts acting on the delay unit optics the setup is enclosed by a plexiglass box. Additionally, a support construction was specially designed for the delay unit, providing suitable translations and rotations for the alignment of the delay unit optics to the X-ray beam. The horizontal translation with a movement of 50 mm allows also to remove the delay unit from the beam path. The maximum range of the vertical translation is 50 mm. The support structure comprises 8 adjustable feet allowing to correct for tilts of the granite support. The size of the whole assemble is 930 mm x 990 mm x 1990 mm.

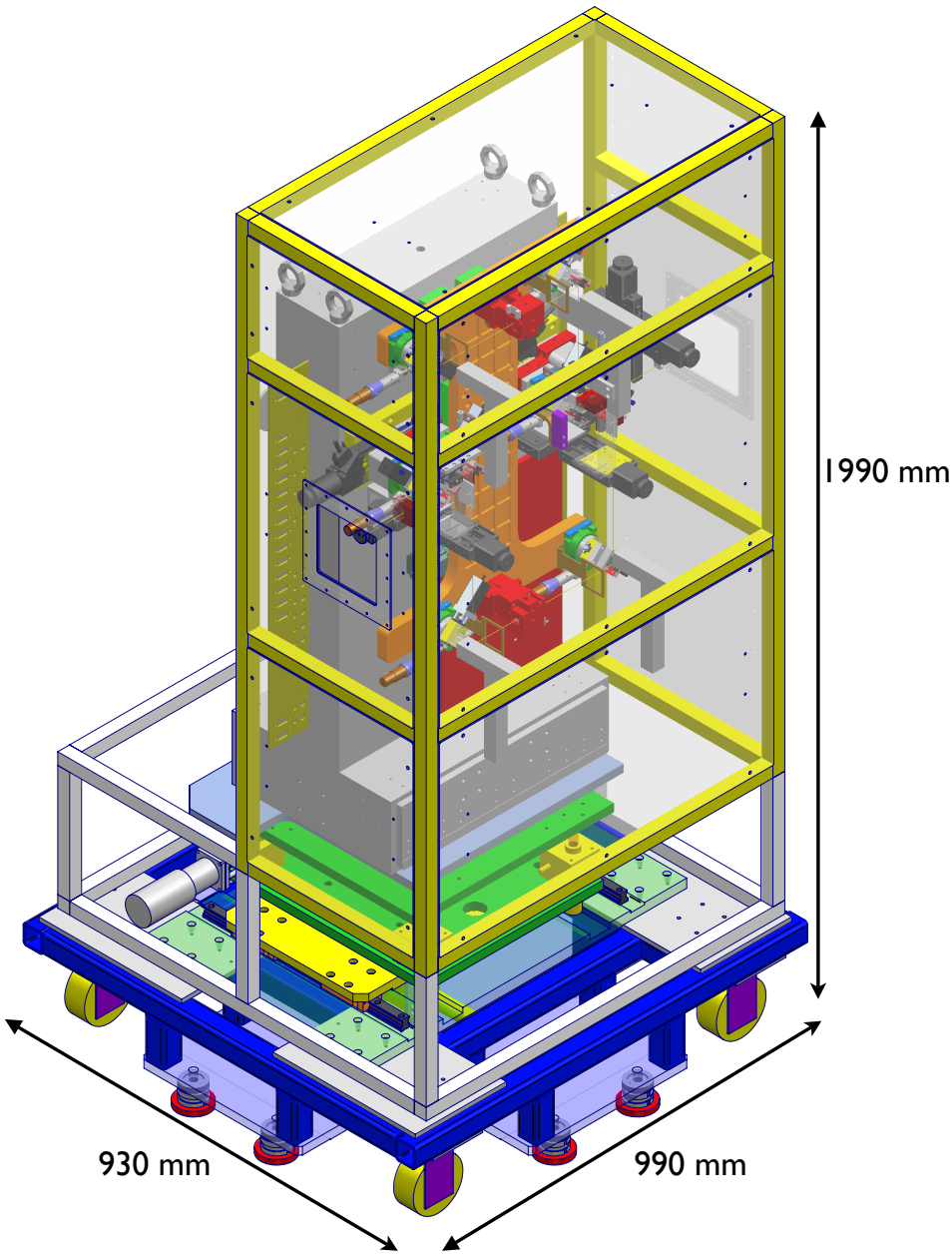

Figure 3.8: 3D model of the delay line with the support structure.

It should be noted that the possibility for conducting pump-probe experiments was implemented in the design. When the BC3 crystal stage, shown in figure 3.3, is replaced by the splitter stage SP2 and the BC4 stage is removed, the delay unit operates with the upper branch configuration only. Figure 3.9a shows the corresponding configuration.

The setup allows for other crystal arrangements as well. A combination in which the beam splitters are replaced with Bragg crystals (the Bragg - branch) is shown in figure 3.9b.

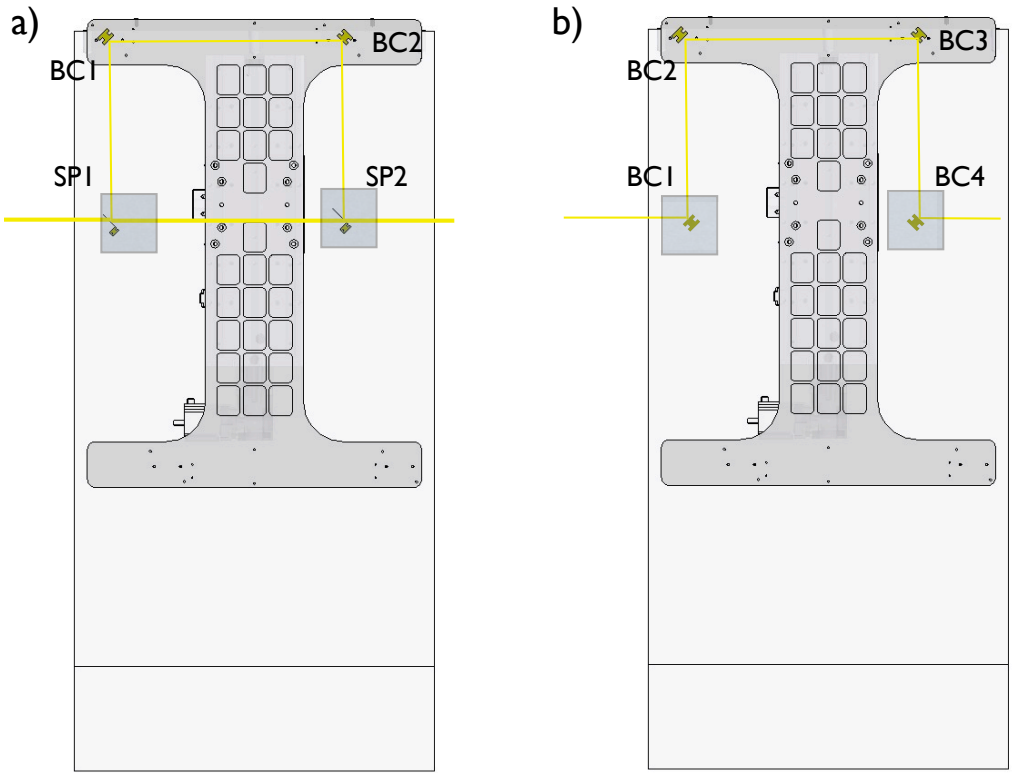

Figure 3.9: a) The delay unit arranged for pump - probe experiments. b) Bragg crystal configuration of the delay unit. For clarity the mechanics of the crystals is not shown.

3.3 Delay line control system

Figure 3.10 shows a sketch of the delay unit control system. Alignment of the delay unit optics and the change of the delay time is fully controlled by a PC. The communication between the computer and the devices is realized via VME electronics. This includes motor controllers (OMS VME58) and SINCOS power supplies for 32 motorized devices (16 translations, 8 swivel and 8 rotations stages). All stages were equipped with micro stepping option, which improves the resolution by a factor up to 20. Eight piezo low voltage actuators are controlled by LVPZT controllers (E-621) installed and networked in one chassis. The connection between the chassis and the PC is established via RS-232.

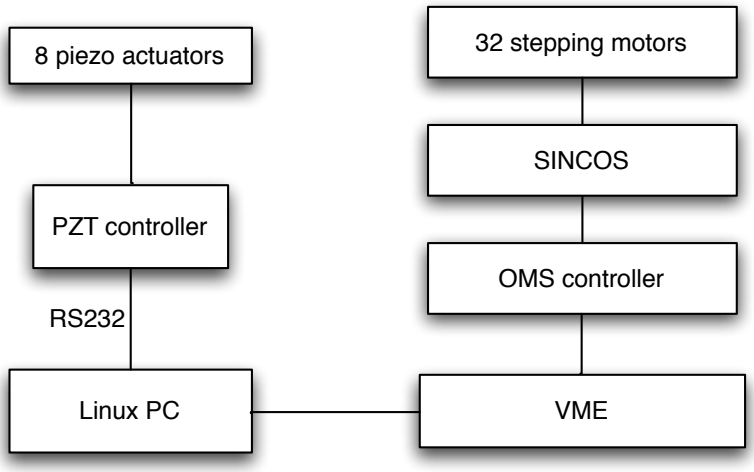

Figure 3.10: Schematic of the delay unit control system.

3.4 Diagnostics

The diagnostics system of the delay unit comprises two detector types: ionization chamber (IC) (cf. section 3.4.1) and an Avalanche Photo Diode (APD) (cf. section 3.4.2). Figure 3.11 shows the layout of the diagnostic system of the delay unit. The first detector on the X-ray beam path is an ionization chamber (ICM), which is mounted 89 mm in front of the beam splitter and serves as a monitor

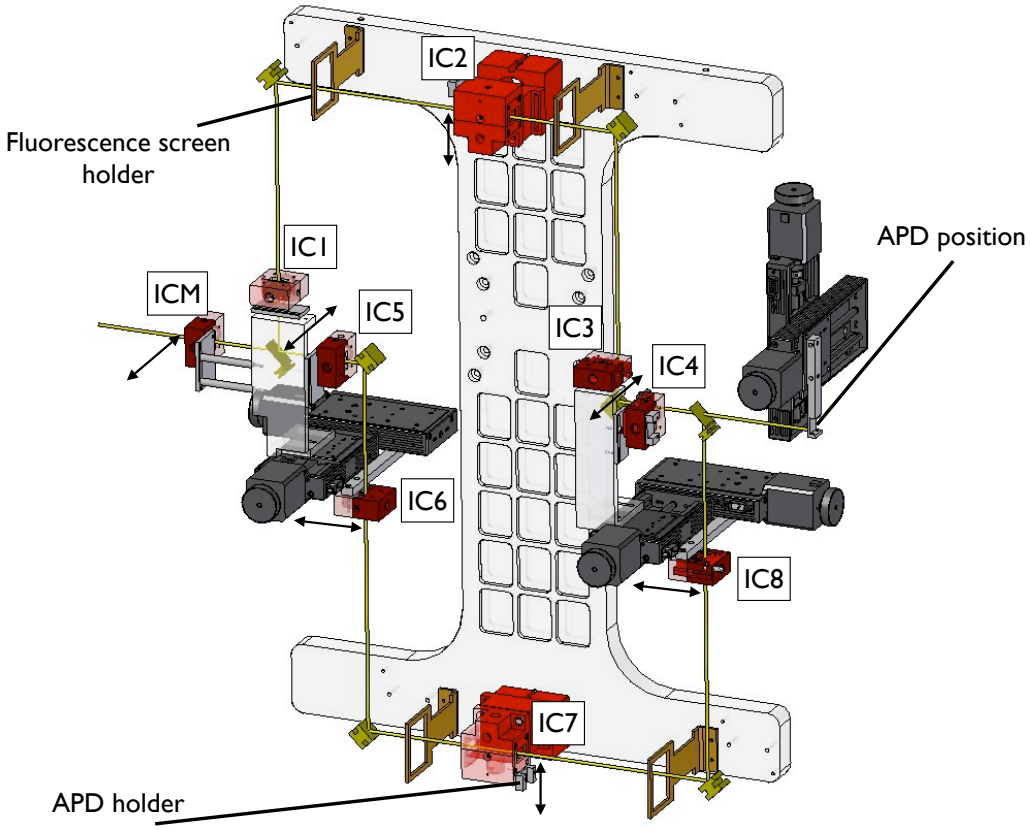

Figure 3.11: Diagnostics of the delay unit. Possible movements of the chambers are depicted by arrows.

for the incoming X-ray intensity. It is followed by 8 further ionization chambers, placed behind each crystal of the delay unit, as it is shown in figure 3.11. In this way the intensity reflected by any crystal is monitored by a dedicated ionization chamber. Due to the compact design of the delay unit, two sizes of chambers are employed: 'small' chambers (ICM, IC1, IC3, IC4, IC5, IC6, IC8) and 'big' chambers (IC2, IC7) with 12 mm and 36 mm length of electrodes along the beam path, respectively. All 'small' chambers are mounted on motorized translation stages (MICOS VT-80) allowing horizontal alignment relative to the beam path. The stages are coupled to the granite support, such that movement of their motor drives does not affect the stability of the aluminum plate. The range of translation is large enough (i.e. 30 mm) to move the chamber out of the beam path.

'Big' chambers are mounted on special holders, which allow a vertical alignment. Additionally, each ionization chamber was equipped with an APD holder. To visualize the beam position along the delay path a set of removable fluorescence screens is mounted to the aluminium plate.

3.4.1 Ionization chamber

Two types of ionization chambers were designed for the diagnostics of the delay unit optics. Figure 3.12 shows the 'small' chamber manufactured at HASYLAB/DESY.

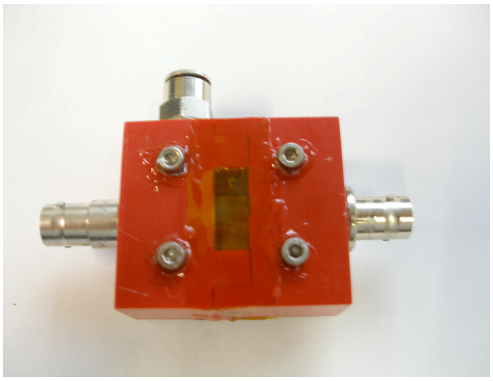

Figure 3.12: Front view of the ionization chamber

The housing of the chambers is made of a light insulating material (i.e. trovidour). To minimize discharging effects the electrodes are made of polished copper. The chamber incorporates standard high voltage (SHV) and signal (BNC) connectors. The efficiency of the chamber can be increased by filling it with various gases. To prevent any leakage of the ionization current through the insulator, a guard ring was employed in the design [38]. The front and the back window is made of 20 μm thick kapton foil. A set of threads on the front side of the ion chamber allows to mount a holder for the APD detector. The small dimensions of the chamber (24 mm x 47 mm x 20 mm) allows one to incorporate it in the very compact design of the delay unit.

The second type of chambers, i.e. the 'big' chamber allows achieving higher ionization currents.

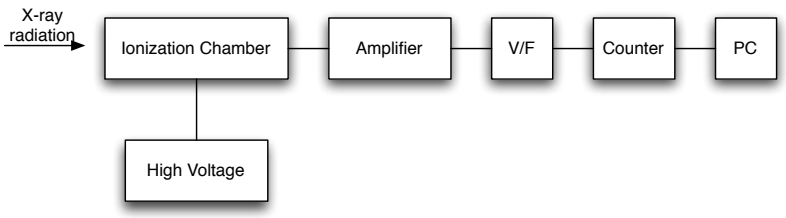

Figure 3.13: Scheme of the electronics used in the ion chamber detection system

A diagram of the ionization chamber electronics is shown in figure 3.13. The electric field is created in the chamber by applying a voltage between the electrodes from a high voltage power supply (NHQ 234M). The measured ionization current is amplified by a current-voltage amplifier (FEMTO DLPCA-200). The voltage signal is processed by a voltage to frequency (VF) converter and then by a counter (CAEN V260). The count rate is read out by the Linux PC workstation using the SPECTRA program package (cf. section 3.4.4).

The performance of both chambers was measured at beamline C of DORIS III (cf. section 3.5.1) with a beam of 8.39 keV X-rays, monochromatized by perfect Si(111) crystals. The beam size defined by exit slits was 1 mm × 2 mm (vertically × horizontally). The first beam splitter was replaced by a Bragg crystal. The ionization current reached saturation at 200 V and 300 V for the small and the big chamber, respectively. The typical ionization current measured at IC1 and IC2 positions was 1.25 pA and 2.5 pA, respectively.

3.4.2 Avalanche PhotoDiode

Time delay measurements were performed with an APD detector [39, 40]. Figure 3.14 shows one of the APDs used in the experiment. The detector consists of a silicon diode and a fast amplifier. They are mounted in a metal case, reducing possible noise and reflections. The downstream electronics is presented in the following section. The front side of the detector is covered with a thin aluminized mylar window, used as a shielding against parasitic light.

Figure 3.14: Amplifier and APD head with an active area of 10 x 10 mm^2.

The large active area of 10 × 10 mm^2 and the high dynamical range of the detector allowed to speed up the alignment of delay unit optics. With a specially designed holder the detector can be mounted on each ionization chamber (see figure 3.11).

A second APD detector with a 3 mm diameter active area is fully dedicated to time delay measurements. The detector was provided by the staff of the beamline ID18 of ESRF.

3.4.3 Timing electronics

Figure 3.15 shows a schematic of the electronics used in time delay measurements. The detector signal is amplified close to the diode by a fast amplifier (AMP). The signal is sent with an amplitude of typically 20 to 100 mV to a constant fraction discriminator (Ortec 935 CFD), which filters out the noise from the amplifier. The output signal from the CFD is used as a start trigger of a time to amplitude converter (Ortec TAC/SCA 567). The bunch clock signal from the synchrotron ring is used as a stop pulse for the TAC. Since the TAC range is limited, the arrival time of the stop pulse can be adjusted by an electronic delay unit. The TAC produces a pulse with an amplitude proportional to the time interval between the start and stop pulses. The amplitude distribution of TAC pulses is digitized by an analog to digital converter (Canberra ADC 8715) and stored in a multichannel analyzer (MCA TVME200). The conversion of channels to time is determined with the time calibrator (Ortec Time Calibrator 462) or the electronic delay unit.

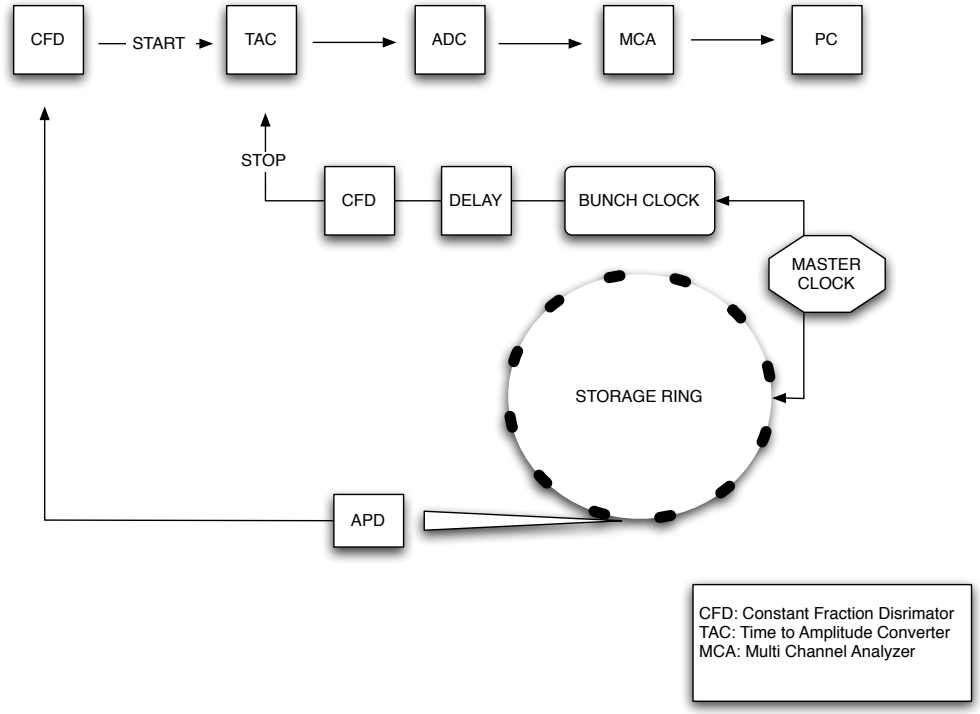

Figure 3.15: Standard signal processing of the time delay measurements.

3.4.4 Software

The time delay experiments and the crystal alignment is controlled by a linux PC using the SPECTRA/ONLINE program package, developed at HASYLAB [41, 42]. The delay unit can be operated either via a traditional command line interface or a graphical user interface called TKI. Several macros have been compiled allowing automatic alignment of the delay unit optics.

3.5 Description of beamlines

3.5.1 Beamline C at DORIS III

Figure 3.16 shows the schematic layout of the beamline C (CEMO) of DORIS III. The time structure of the storage ring is characterized by 482 equally spaced orbital positions (buckets) with 2 ns spacing. In 5 bunch mode only 5 out the 482 buckets in the ring are filled resulting in 4 bunches traveling with 192 ns and one bunch with 196 ns time spacing.

The beamline provides X-rays in the range from 6 keV to 43 keV. The horizontal and vertical source sizes are 2.8 mm and 0.9 mm, respectively. The vertical beam divergence is 0.12 mrad. The two sets of slits, located upstream the beamline monochromator define the size of the incident synchrotron beam. The water cooled Si(111) double crystal monochromator is located 19.3 m from the source in vertical scattering geometry. At 8.39 keV the intrinsic bandwidth of the monochromator crystals is 1.17 eV. A third set of slits (exit slit) is installed in the experimental hutch 28.8 m from the bending magnet source. The intensity downstream the monochromator was monitored by an ionization chamber (IC MON), located directly after the exit slit. The first crystal of the delay line is located 32 m downstream from the source. The location of the delay unit in the CEMO hutch is shown in 3.17.

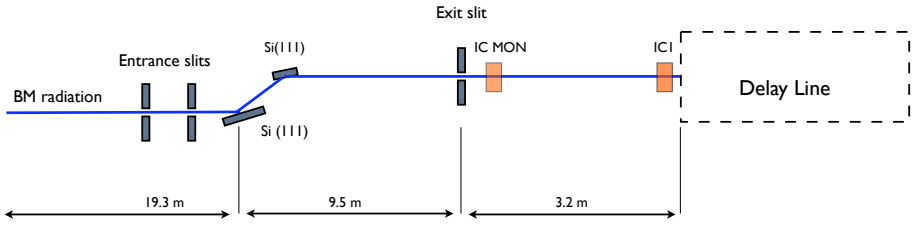

Figure 3.16: Schematic side view of the beamline C at DORIS III, HASYLAB.

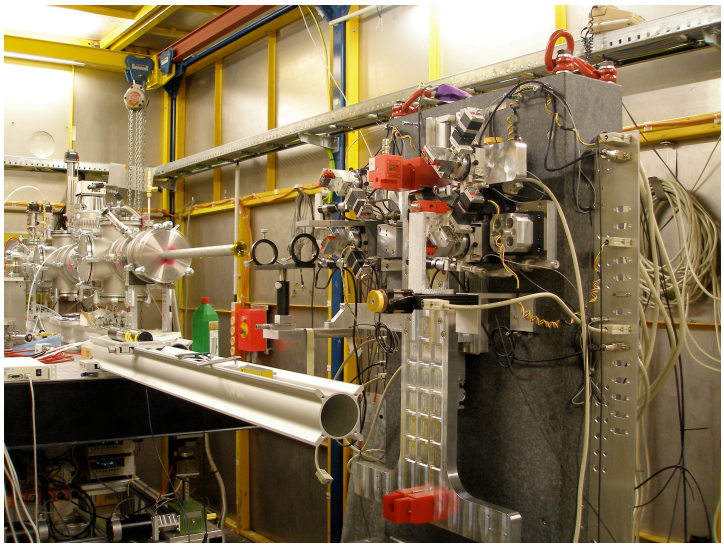

Figure 3.17: The delay line unit in the one branch configuration situated in the hutch of beamline C.

3.5.2 Beamline D4 at DORIS III

Figure 3.18 shows the general layout of the beamline D4 experimental hutch, located at the storage ring DORIS III. The polychromatic synchrotron radiation entering the hutch is collimated by a slit assembly (primary slits). A vertical mirror bends the beam downwards and cuts off the high energy part of the X-ray beam. The reflected beam can be visualized by a diamond fluorescent screen (CVD) placed downstream of the mirror. The energy of the incoming radiation is defined by a single-bounce Si(111) monochromator in horizontal scattering geometry. Further monochromatization ($\Delta\lambda/\lambda = 8.6{\cdot}10^{-6}$) is achieved by a monolithic Si(333) channel-cut crystal. The final beam size is defined by secondary slits, located 150 mm upstream of the sample stage.

In order to test the performance of the Si(511) beam splitter at a scattering angle of 45°, the crystal was mounted in the vertical diffractometer equipped with two detectors. The crystal was glued with wax to a sample holder and mounted with a goniometer head to the diffractometer (see figure 3.19). The sketch of the scattering geometry used in the experiment is shown in figure 3.18.

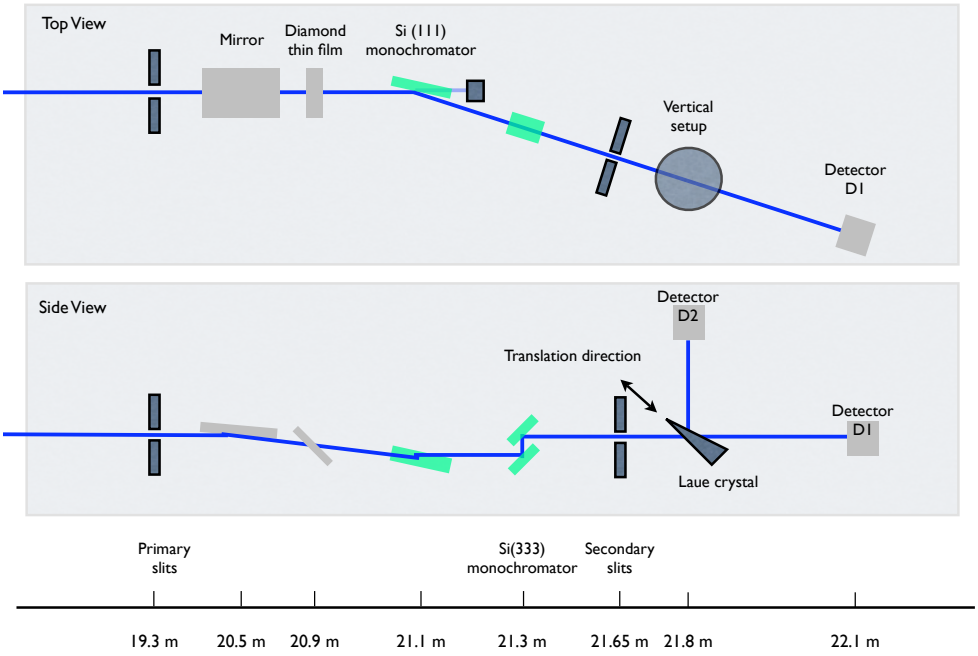

Figure 3.18: Layout of D4 beamline

The vertical setup consists of a 2-theta arm, omega movement and two tilt stages. Additional translations are provided by the goniometer head. The intensities of the scattered and transmitted beams were monitored by two detectors. One was mounted on the vertical 2-theta arm and positioned in the scattering plane right above the crystal. The second one was placed into the direct (transmitted) beam. The variations of the scattered and transmitted intensity were recorded while the crystal was rotated and vertically translated through the beam.

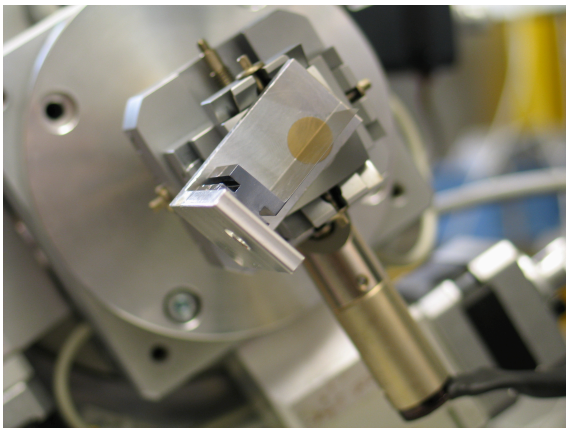

Figure 3.19: Goniometer head with the beam splitter crystal mounted on the vertical spectrometer. The setup was placed on the 3 - axis sample translation stage of beamline D4.

3.5.3 Beamline PETRA 1 at PETRA II

PETRA 1 was a beamline operating in the energy range from 12.4 keV to 55 keV with radiation provided by an undulator situated in the straight section of the PETRA II storage ring. The time structure of the ring can vary from 80 bunches with 98 ns separation down to one single bunch resulting in a pulse interval of 7.68 μsec.

The source size and the divergence of the photon beam from the undulator are given in the table 3.1. Figure 3.20 shows a simplified layout of the PETRA 1 beamline. The undulator beam is split by a diamond crystal oriented in asymmetric Laue geometry ($\alpha = 54.7^0$). The beam is directed downstream the diamond crystal to the PETRA 1 experimental hutch using a Ge(220) monochromator

Table 3.1: Source size (FWHM) and divergence (FWHM) of the photon beam from the PETRA 1 undulator.

	source size [mm]	divergence [μrad]
Horizontal	2.82	49.45
Vertical	0.3	14.12

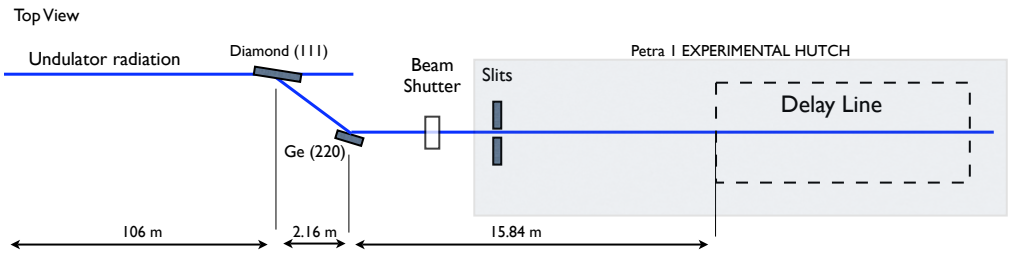

Figure 3.20: Simplified layout of the PETRA 1 beamline. The delay line was located 123 m downstream the source.

crystal. The achieved energy resolution is $1.45{\cdot}10^{-4}$. The final beam size is defined by the exit slit system located at the entrance of the experimental hutch.

3.5.4 Beamline ID10C Troïka at ESRF

The ID10C beamline is part of the multi-station undulator beamline ID10 at ESRF. The storage ring operates in various timing modes: 4 bunch mode with 704 ns time spacing between the pulses e.g. 16 bunch mode with 176 ns inter-bunch spacing and uniform filling, where 992 electron bunches are equally separated by 2.82 ns.

The layout of the ID10C beamline is sketched in figure 3.21. The X-ray source consists of 3 undulator segments: one 27 mm undulator (U27), one 35 mm undulator (U35), and a revolver unit carrying both U27 and U35 undulators. The electron beam size and the photon beam divergence are listed in table 3.2.

Table 3.2: Source size (FWHM) and divergence (FWHM) of the photon beam at the Troïka beamline.

	source size [μm]	divergence [μrad]
Horizontal	928	28
Vertical	23	17

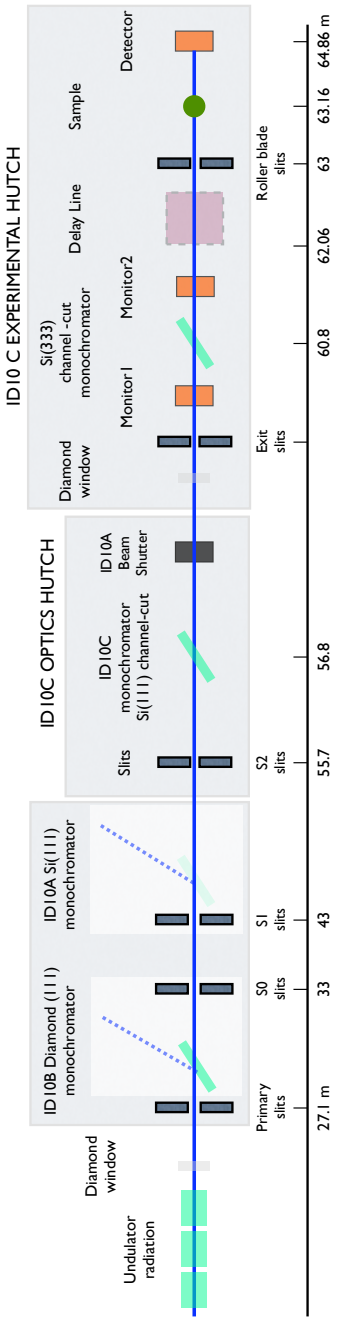

Figure 3.21: Layout of the ID10C beamline (top view)

Before the beam enters the first optic hutch it passes through a 300 μm thick CVD diamond window. The first set of slits (primary slits) is located 27.1 m away from the source. At 30.5 m from the source the beam passes the diamond(111) monochromator delivering the beam to the ID10B experimental hutch. A second slit system S0 is located 33 meters from the source. A third pair of slits S1 is placed 1.2 m before the Si(111) ID10A beamline monochromator, which was moved out from the beam path during experiments at ID10C station. A fourth set of slits is installed 1.1 m before the ID10C beamline monochromator. The water cooled Si(111) ID10C monochromator is a monolithic channel-cut crystal diffracting the 8.4 keV X-rays in the horizontal scattering plane. Next follows a thin diamond window, which separates the vacuum of the optics hutch from the experimental hutch. Monitor detectors (scintillation counters) at the beamline ID10 measure scattering from a thin caption foil at 90 degrees. Monitor 1 is placed right behind the exit slits ES. It allows to monitor the stability of the incoming intensity. The beam is further monochromatized to $\Delta\lambda/\lambda = 8.6 \cdot 10^{-6}$ by a monolithic Si(333) channel-cut crystal oriented in vertical scattering geometry. The crystal was mounted without housing[3] on a diffractometer located 60.8 m downstream the source.

Since the Si(333) monochromator suppresses the higher harmonic components of intensity there was no need to use a mirror in the experimental setup. Monitor 2 was placed downstream the monochromator 300 mm in front of the X-ray beam splitter (i.e. the first crystal of the delay line). The incident flux achieved at the Monitor 2 position with U27 and U35 undulators and slits settings: S0($200 \times 200\ \mu m^2$), S1($3 \times 3\ \mathrm{mm}^2$) S2($300 \times 300\ \mu m^2$) and ES($3 \times 3\ \mathrm{mm}^2$) was $2.72{\cdot}10^{11}$ photons/s at 60 mA storage ring current.

The location of the delay line in the ID10C hutch is shown in figure 3.22. The granite support was placed on a custom designed support structure described in section 3.2.1. The delay line optics was enclosed by a plexiglass shield to minimize any influence of temperature changes existing within the hutch.

[3]The crystal was operated under ambient condition without any housing protecting against temperature variations in the hutch.

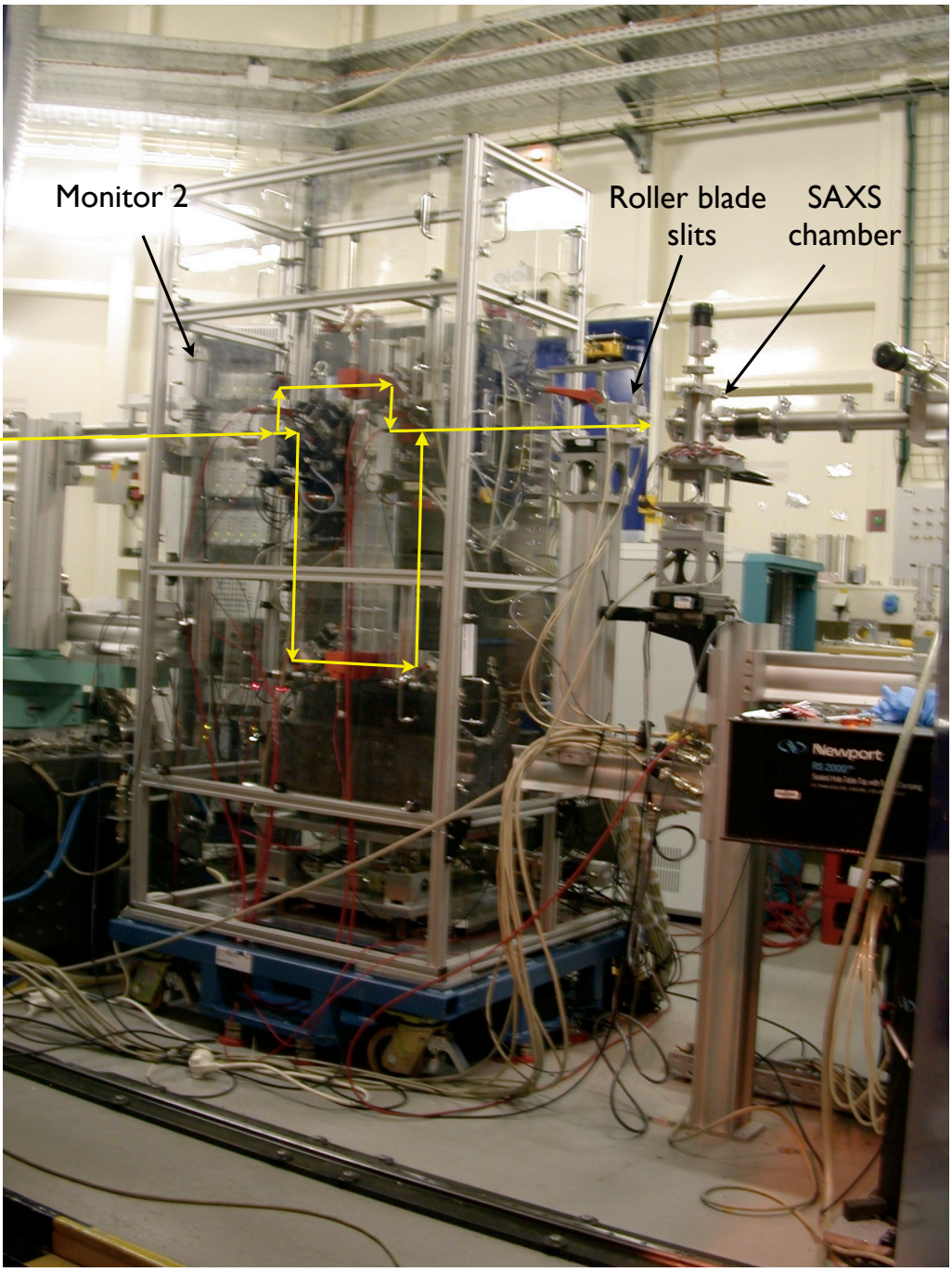

Figure 3.22: Delay unit at the ID10C experimental hutch. The X-ray path is denoted by the yellow line.

The experimental setup downstream the delay unit is described in the following sections.

Experimental setup for Fraunhofer pattern measurements

In order to investigate the coherence properties of the X-ray beam one can study the scattering from a collimating slit in the far field. Figure 3.23a shows the detailed view of the experimental setup utilized in the Fraunhofer pattern measurements. Downstream of the delay unit (i.e. 63 m from the source) the size of the X-ray beam is defined by a pair of roller blade slits [43]. The slits are polished tantalum blades of cylindrical shape with a longitudinal offset of 3 mm. A 1.5 m long evacuated flight tube minimizes air scattering and absorption. The Fraunhofer diffraction pattern of the slits is measured with a point detector (a scintillation counter) located at the end of the flight tube. The detector is mounted on a translation stage, which allows movements in the vertical and horizontal plane. Additionally, the detector stage is equipped with a set of horizontal and vertical slits that allows one to select the solid angle of the intensity diffracted by the slits. The detector slits setting defines the resolution of the measured Fraunhofer pattern. The slit system is located 1.855 mm from the the roller blade slits.

Experimental setup for the static speckle analysis

The setup for the static speckle pattern measurements is similar to the configuration used to measure Fraunhofer patterns. Figure 3.23b shows a detailed view of the experimental setup. The coherent part of the radiation is selected by roller blade slits. The sample is placed in a capillary in a custom designed SAXS chamber [44] mounted 155 mm downstream of the slits.

The static speckle pattern was recorded by a direct illumination CCD Princeton camera which comprised 1340 $\times$ 1300 pixels each of dimension 20 $\times$ 20 μm^2. The detector - sample distance was 1.7 m. The beam stop was mounted in front of the detector to prevent it from illumination by the direct beam. About half of the detector area was obscured by the beamstop as illustrated in figure 3.23b.

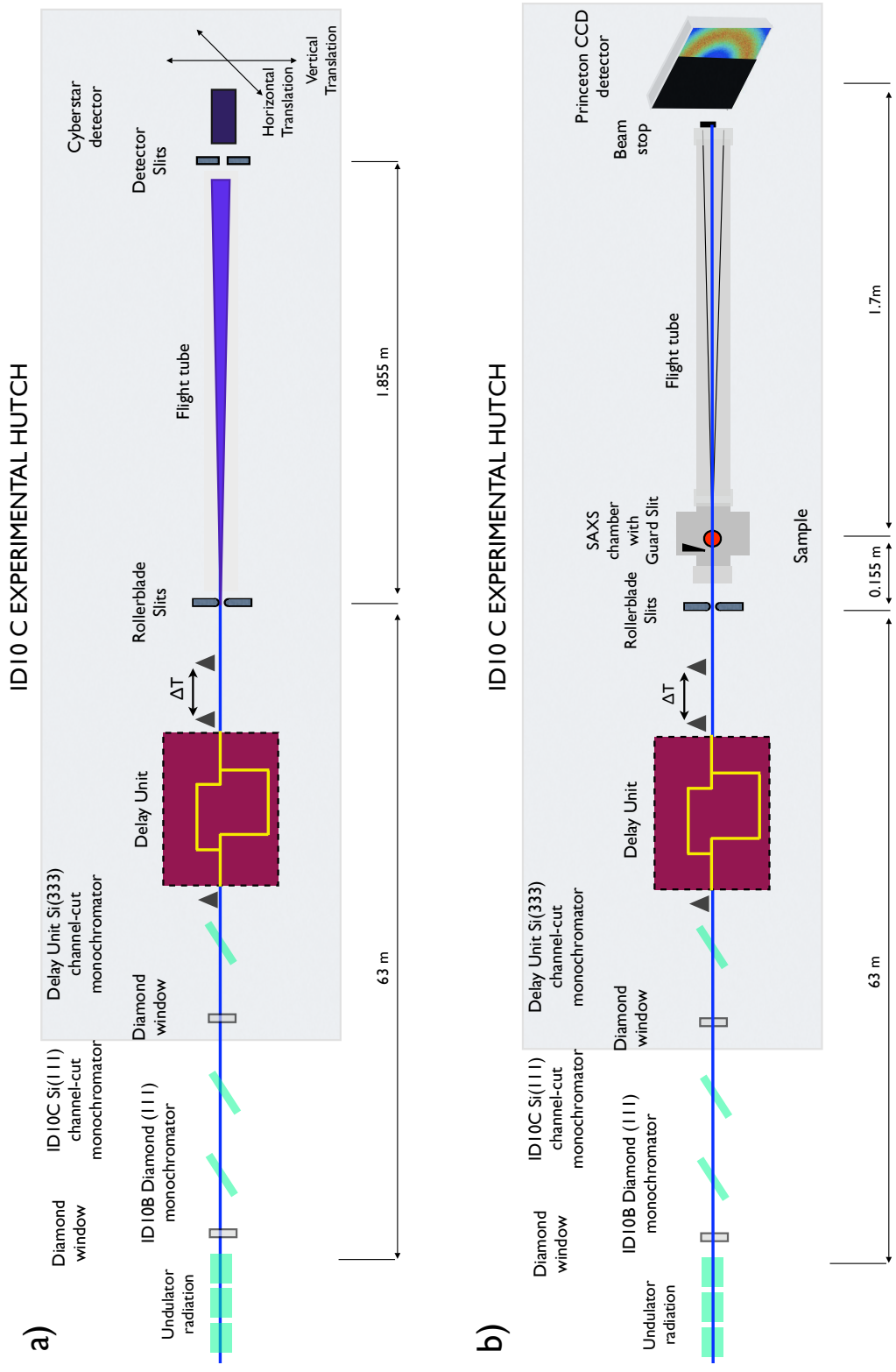

Figure 3.23: a) Detailed arrangement of the experimental components used in the slit scattering experiments. b) Layout of the experimental setup for coherence characterization of the delayed photon beam with statistically disordered SiO_2 sample.

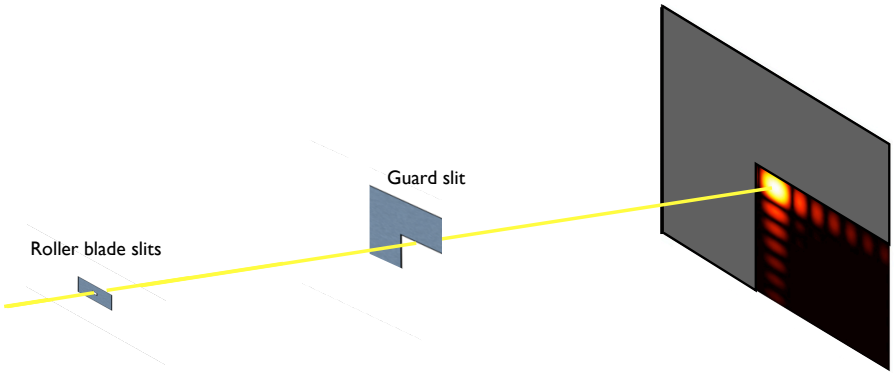

Figure 3.24: Schematic representation of the effect of the guard slit.

Since the pinhole produces coherent radiation the measured signal in the far field contains not only the scattered intensity from the sample but also a coherent scattering from the slits. In order to transmit only the central Fraunhofer peak the chamber is equipped with the thick tantalum guard slit, which is located just in front of the sample position. If the guard slit is opened widely, the full Fraunhofer pattern is visible on the detection plane. In the optimum position of the guard slit the Fraunhofer diffraction can be suppressed, which is illustrated schematically by figure 3.24.

Figure 3.25 shows two examples of diffraction patterns from disordered SiO_2 powder sample obtained at various guard slit positions. In the first case, presented in figure 3.25a, only the scattering ring from the sample is detected. Since the sample is illuminated by the coherent beam the diffraction pattern is decorated with intense bright spots i.e. speckle pattern. Translating the guard slit away from the beam results in a speckle pattern with higher count rate but the Fraunhofer diffraction of the slits is superimposed. This is illustrated in figure 3.25b. It is clear that alignment of the guard slit is essential for the static speckle experiments.

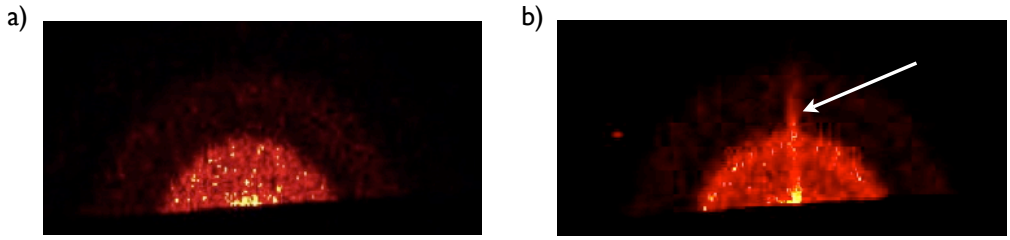

Figure 3.25: Speckle pattern obtained from $Si0_2$ with two different positions of the guard slit. a) Optimum position of the guard slit. b) Position at which the guard slit is away from the direct beam and the pinhole produces a parasitic scattering, indicated by the arrow.

Chapter 4

X-ray delay unit performance

The performance of the X-ray delay unit at 8.39 keV and 12.4 keV is described in this chapter. The quality of the optical components of the delay unit is characterized and the throughput of the delay unit is measured. The effect of the non-dispresive (+n,-n) and dispersive (+n,+n) crystal configurations on the throughput is discussed within the context of a DuMond approach. Delay time measurements are performed in the one and two - branch configurations. The influence of the delay unit optics on the coherence properties of undulator radiation are investigated by measuring Fraunhofer diffraction and speckle patterns from a static disordered sample.

4.1 Delay unit optics

4.1.1 Introduction

The delay unit is a tool for conducting pump-probe and correlation spectroscopy experiments. To utilize this device in the aforementioned techniques, it is necessary to understand the behavior of each optical component and quantify the performance of the whole unit in terms of throughput and stability. As it was shown in the previous chapters, the X-ray delay unit utilizes two Laue and six Bragg crystals arranged in dispersive (+n,+n) and non-dispersive (+n,-n) configurations. To characterize the throughput of such a complex optical system the experiments are performed in steps. First, the quality of the Bragg optics in the 4 crystal Bragg configuration is investigated. Then the splitting performance of the Laue crystals is verified. Finally, the throughput and the stability of the delay unit is measured in the two-branch configuration.

In order to preserve the high source brightness, each of the delay unit crystals has to diffract the X-ray beam efficiently. An ideal single crystal has a reflectivity which equals unity and a reflectivity curve matching the Darwin profile. Due to absorption, the crystal reflectivity will be always lower than unity. For the delay unit optics i.e. Si(511) and Si(553) the theoretical reflectivities at 8.39 keV and 12.4 keV are 0.89 and 0.92, respectively. From the dynamical theory of X-ray diffraction, it is known that the profile of a measured diffraction curve provides information about crystal imperfections, strain and asymmetry. Therefore, the full width at half maximum (FWHM) of the rocking curve can be taken as a measure of the crystal quality. For Si(511) and Si(553) the expected Darwin widths are 8.6 μrad and 2.3 μrad, respectively.

To observe a nearly intrinsic rocking curve profiles one needs to employ an extremely collimated and monochromatized X-ray beam [45]. This condition implies the use of crystal monochromators and beam collimating optics. Both i.e. monochromatization and collimation can be achieved by using asymmetric reflections. However, even without sophisticated beam collimating optics, information on the quality of optical elements can be obtained by the measurement

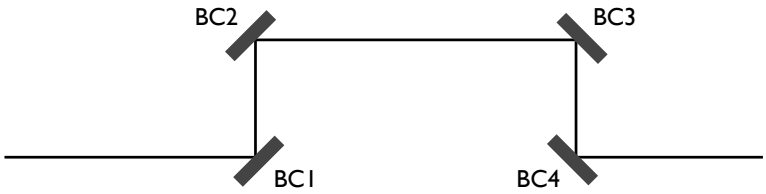

Figure 4.1: Crystal arrangement of the delay unit in the symmetric four crystal Bragg configuration.

of double-crystal rocking curves in a non-dispersive arrangement e.g. BC1-BC2 or BC3-BC4 in a 4 crystal arrangement shown in figure 4.1. This is shown for the BC3-BC4 case in figure 4.2a. When the crystal BC4 is rocked (through the Bragg angle) its Darwin curve (and corresponding reflection band in the DuMond diagram) crosses successively positions A, B, C, D, and E, as shown in figure 4.2b. Maximum transmission is obtained at position C, where the reflecting planes of the both crystals are parallel. The double-crystal rocking curve is the integral over the product over two Darwin curves as a function of angular displacement. It contains therefore information about the quality of both crystals. Figure 4.2c shows the expected double - crystal rocking curve calculated[1] for two Si(511) reflections. It is interesting to note that the resulting curve is symmetric in contrast the Darwin curve and has a width of 12.2 μrad.

In the delay unit experiments, the reflectivity of each crystal was determined from $R_C = I_1/I_0$, where I_1, I_0 are the intensities measured by ionization chambers (depicted in figure 4.2c) located upstream and downstream the crystal, respectively. Since the intensity is normalized to I_0, the maximum reflectivity of BC3 has been taken as unity in the calculations. The FWHM of the calculated double - crystal rocking curve in the present example obtained from a gaussian fit is 12.2 μrad. The expected maximum peak reflectivity is 0.73.

[1] calculated by the XOP 2.11 package [24].

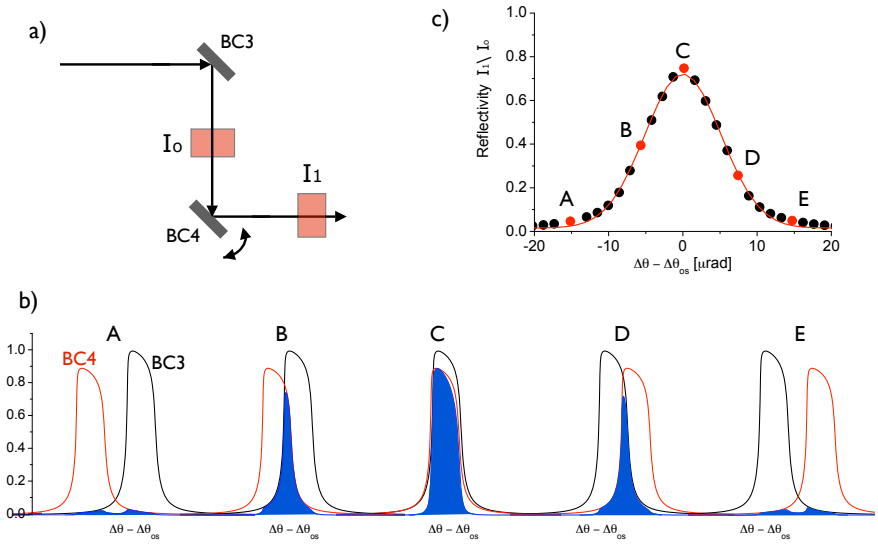

Figure 4.2: a) BC3-BC4 crystal arrangement. b) Double-crystal diffraction curve when the crystal BC4 is "rocked". The blue profile is the product of two Darwin curves. c) Calculated double-crystal rocking curve. The red solid line is a Gaussian fit.

4.1.2 The four crystal Bragg device

In this section the Bragg optics of the delay unit is studied in detail. The setup, shown in figure 4.1, utilizes four symmetric Bragg crystals arranged in 90° geometry. The diffraction properties of two sets of crystals i.e. Si(511) and Si(553) are investigated at 8.39 keV and 12.4 keV, respectively.

The measurements of Si(511) rocking curves were carried out the undulator beamline ID10C at ESRF(see figure 3.21). The incident beam was monochromatized by the Si(111) and Si(333) monochromators. The beam size was defined by collimating slits S0, S2 and ES, that were set to 200 × 200 μm^2, 300 × 300 μm^2 and 3 × 3 mm^2, respectively. Measured data were normalized to the monitor count rate. Since the experiment was performed under ambient conditions, the measured rocking curves were corrected for absorption losses.

Figure 4.3 shows two typical measured rocking curves for two pairs of Bragg crystals. The red solid line is the fit of a gaussian to the experimental data. The FWHM of the fit is 11.2 μrad and 11.77 μrad, respectively. The calculated

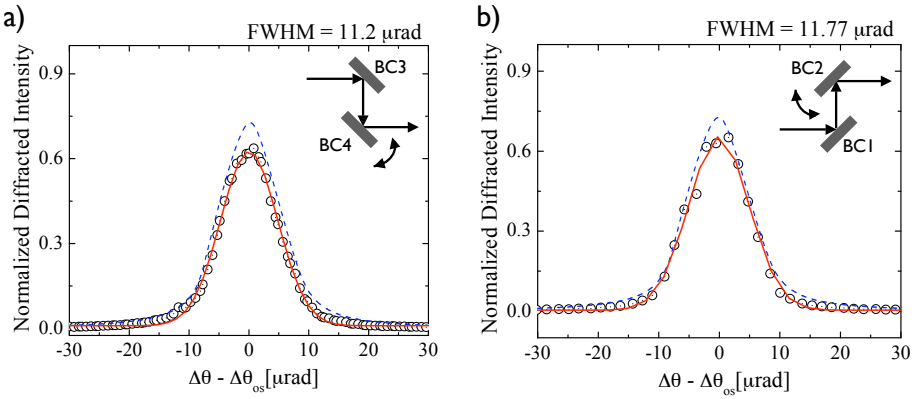

Figure 4.3: Diffraction profiles of Si(511) in symmetric Bragg geometry at E = 8.39 keV measured at the undulator beamline ID10C. BC1, BC2, BC3, and BC4 denote the Bragg crystals depicted in figure 3.9b. The red solid line is a Gaussian fit to the experimental data. The calculated rocking curves are shown by the blue dashed line. The inset of each figure shows corresponding crystal arrangement. The arrow indicates the crystal being rocked.

rocking curve $\omega = 12.2$ μrad is depicted by the blue dashed lines.

The measured rocking curve widths are slightly narrower (see below) than the theoretical values with relative deviations (see equation A.2) of 8% and 3%, respectively. This shows the very good quality of the respective crystal pairs.

The reflectivities of the crystals BC4 and BC2 are 0.62 and 0.63, respectively. These values are lower than the expected value of 0.73. The slightly smaller than theoretical rocking curve width together with the reduced reflectivity might be attributed to the misalignment of the channel-cut Si(333) crystal relative to the delay unit optics (see also figure 4.5). The reflection band of the Si(111) crystal is wider than the one of Si(511), therefore, the monitor located between the Si(333) channel-cut and the BC1 crystal is not sensitive to any instabilities of the channel-cut. This is not the case for monitors downstream of the BC1 crystal. Thus, the throughput and the reflection width of the delay unit optics can be affected.

Figure 4.4a shows the measured diffraction curve of the crystal BC1, arranged in (+n,-n) geometry relative to the Si(333) channel-cut monochromator. Since the reflection width of the reflections Si(333) and Si(511) are identical (see table 2.2)

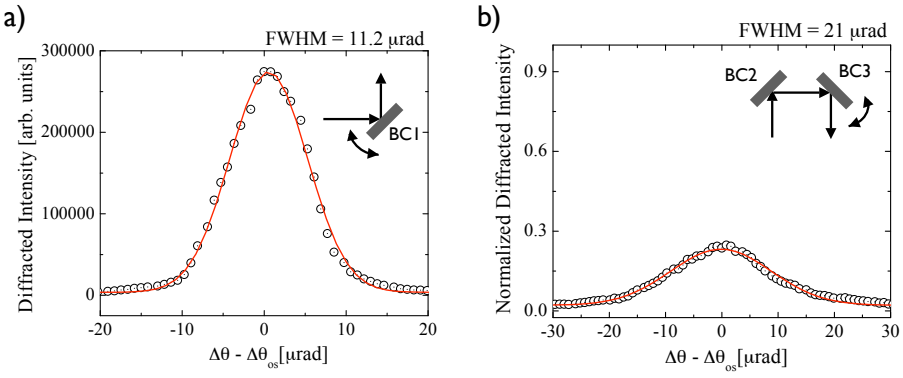

Figure 4.4: Diffraction profiles of Si(511) in symmetric Bragg geometry at E = 8.39 keV measured at the undulator beamline ID10C. BC1, BC2, BC3, and BC4 denote the Bragg crystals depicted in figure 3.9b. The red solid line is a Gaussian fit to the experimental data. The inset of each figure shows corresponding crystal arrangement. The arrow indicates the crystal being rocked.

the expected width of the resulting curve should be equal to 12.2 μrad. A FWHM of 11.2 μrad is measured. This indicates again a slight misalignment of the lattice planes in the crystal of the Si(333) channel-cut monochromator. This effect is illustrated in figure 4.5a. When the lattice planes of the crystals A and B are slightly displaced in angle from the parallel position, the resulting diffraction curve is much narrower than the Darwin width. This leads to a narrowing of the double - crystal rocking curves. Figure 4.5b shows the corresponding DuMond diagram. One should note that the exit beam divergence and the overall throughput of the delay unit optics can be affected by the lower performance of the Si(333) monochromator. It should also be mentioned here that a slight narrowing of the reflection width occurs whenever a X-ray beam is reflected by more than one crystal [21].

Figure 4.4b shows the diffraction curve measured by rocking the crystal BC3. Since the crystals BC2 and BC3 are arranged in dispersive (+n,+n) configuration, the reflectivity of the rocking curve is expected to be the lowest i.e 0.23 (cf. section A.2). The measured curve can be also used to quantify the incident beam divergence. A divergence of Ω = 19 μrad was obtained using expression (A.1)

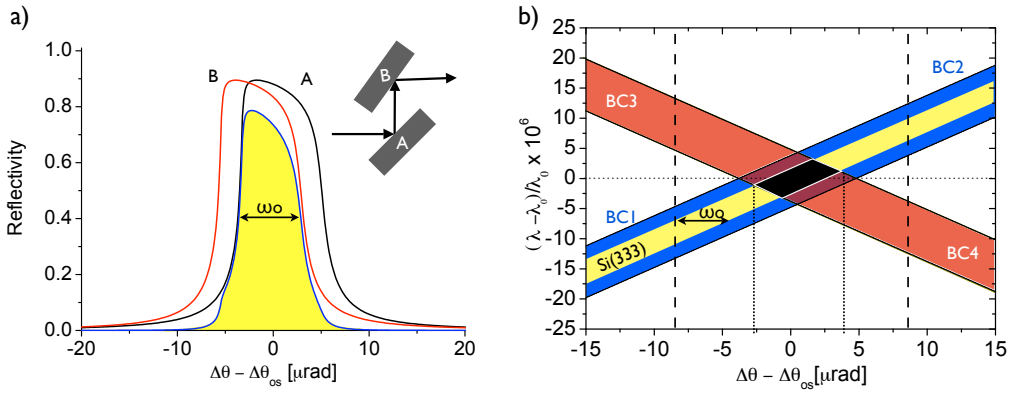

Figure 4.5: a) The 'narrowing' effect of the Darwin curve by a slight misalignments of axes of crystals A and B shown in the inset. The yellow profile is the product of the two unshaded curves. b) Corresponding DuMond diagram. The dashed and dotted line correspond to the incident and exit divergence.

and taking into account the Darwin width of Si(511) and the measured width of the BC3 rocking curve. The resulting value is comparable with the nominal source divergence (i.e. 17 μrad).

From the results obtained at the undulator source it can be concluded that the quality of the delay unit Bragg crystals is very good. Since all delay unit crystals were cut from the same silicon ingot and all measured crystals were of similar quality it is expect that this is the case for all used Bragg crystals. Additional characterization of the delay unit optics was performed at a bending magnet source without Si(333) channel-cut monochromator (cf. appendix A.2). One observes that the reflectivity of the crystal BC2, measured without Si(333) channel-cut is slightly higher than with the Si(333) crystal.

The performance of the Bragg optics at E = 12.4 keV with Si(553) Bragg crystals was investigated at the PETRA 1 beamline of the PETRA II storage ring (cf. section 3.5.2). The measurements were performed with the horizontal and vertical beam size of 6 × 1 mm^2 defined by the exit slit system. The incident beam was monochromatized by the Ge(220) beamline monochromator scattering in horizontal geometry. The DuMond diagram of the corresponding crystal

configuration is shown in figure 4.6a.

Figure 4.6b shows the measured rocking curve of the crystal at the position BC4 (see figure 4.1). The blue dashed line represents the calculated profile of the double-crystal configuration. Good agreement between both curves is found. The discrepancy between measured and calculated width of the rocking curve is 3%.

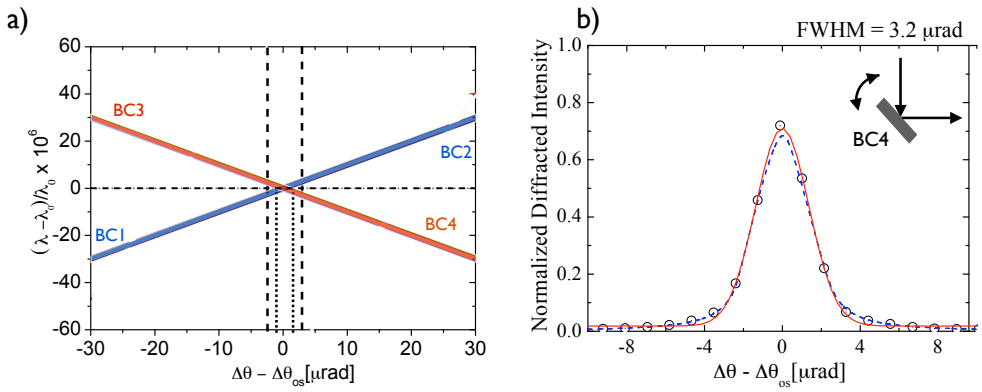

Figure 4.6: a) DuMond diagram of the crystal arrangement at PETRA 1 beamline. The incident and exit divergence is represented by dashed and dotted lines, respectively. b) Measured diffraction profile of Si(553) in symmetric Bragg geometry at E = 12.4 keV. The red solid line is a Gaussian fit to the experimental data. The calculated rocking curve is shown by a blue dashed line.

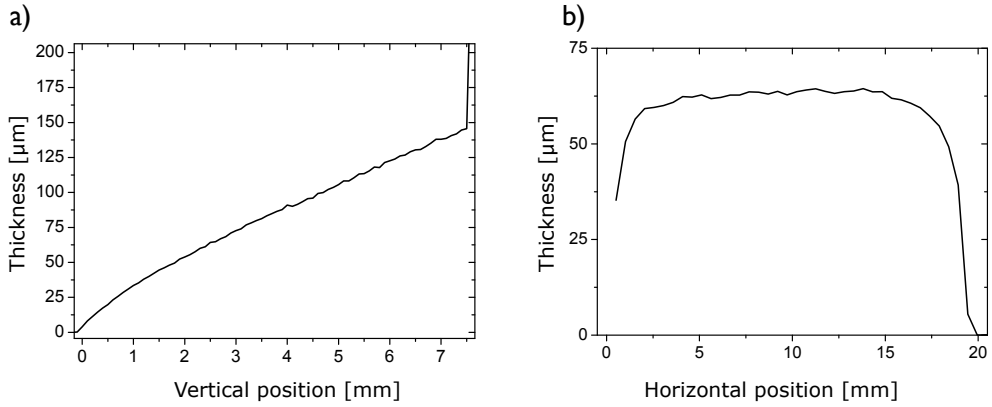

Figure 4.7: Variation of the thickness along the crystal height a) and crystal width b) obtained by transmission measurement

4.1.3 X-ray beam splitter

The Laue beam splitter is one of the key components of the delay unit. It permits to control the splitting ratio. For different experiments different splitting schemes have to be applied. For instance, the 'split-pulse' XPCS technique (cf. section 1.3) requires two equal intensity pulses for autocorrelation measurements. For 'pump-probe' experiments the excitation of the sample is produced by the first very intense pulse and the evolution of the process is observed by the second much weaker pulse. Thus, a different ratio of pulse intensities is demanded. Quantifying the performance of the splitter in terms of its ability to control the splitting is particularly important for the aforementioned experiments. In this section the performance of the beam splitter, proposed in section 2.4.1.3, is presented.

The initial tests of the X-ray beam splitter at E = 8.39 keV were carried out at DORIS III at the beamline D4 (cf. section 3.5.2). The incoming synchrotron radiation beam was monochromatized to a relative bandwidth, $\Delta\lambda/\lambda$ of $8.6{\cdot}10^{-6}$ by the Si(333) channel-cut monochromator. The incident beam divergence was reduced by primary and exit slits set to 200 × 200 μm^2 and 100 × 100 μm^2, respectively.

Since the reflected and forward diffracted intensity oscillate as a function of

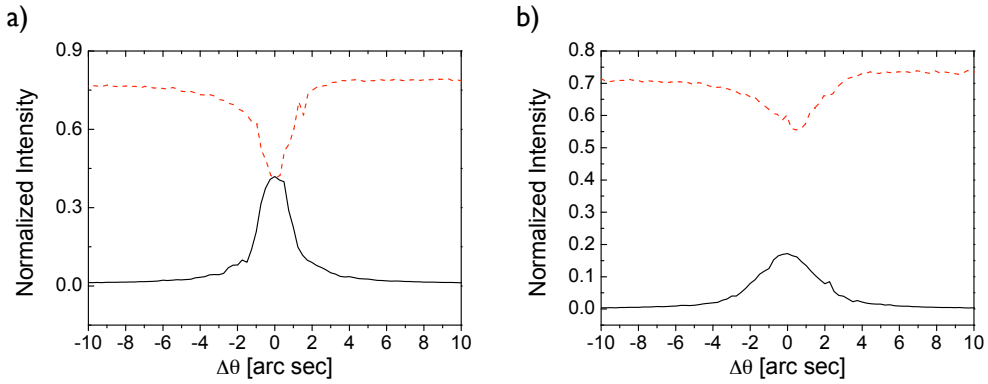

Figure 4.8: Variations of reflected (solid line) and transmitted (dashed line) intensity diffracted by the Laue(511) crystal as a function of $\Delta\theta = \theta - \theta_B$, where θ and θ_B are an incident and Bragg angle, respectively. The crystal was probed at two positions corresponding to a thickness of a) 19.8 μm and b) 25.8 μm.

the thickness of the Laue crystal, the chosen beam splitter was examined first by transmission measurements. Figure 4.7a shows the thickness of the crystal, as determined by transmission measurements. Although the crystal face has a height of about 20 mm, only the top 7.5 mm can be accessed for splitting X-ray radiation. The reason for that is the large foot of the crystal which absorbs the beam completely at 45° geometry (cf. section 3.1). One can see from figure 4.7a that the accessible thickness of the crystal varies from 150 μm down to less than 15 μm at the top. The measurements along the crystal width (i.e horizontally in the plane normal to the beam direction) reveals a constant thickness of the crystal (see figure 4.7b).

From the dynamical theory of X-ray diffraction [21], the Pendellösung effect manifests itself in intensity variation as a function of the crystal thickness. Since the crystal has a wedged form various splitting ratios should be obtained simply by translating the crystal in the scattering plane (cf. section 3.5.2).

In order to split the synchrotron beam into two equal parts the crystal was tested at various positions. Figure 4.8 shows the variations of the forward diffracted and reflected intensities as a function of the relative incident angle recorded at two

positions of the Si(511) Laue crystal corresponding to two different thicknesses. A splitting ratio close to 1:1 was achieved by using the crystal at a thickness of 19.8 μm (see figure 4.8a). At this position 42% of the beam is reflected and 41% is diffracted in the forward direction. About 17% of the intensity is lost due to absorption. The splitting ratio is in agreement with calculations (cf. section 2.4.1).

A dramatically different behavior is observed by probing the crystal close to a characteristic Pendellösung distance Λ_l, namely at the thickness t = 25.8 μm (see figure 2.13). In this case the largest splitting ratio is expected. Figure 4.8b shows the variations of the split beams measured at the thickness of 25.8 μm. At this crystal position only 17% of the beam was reflected and 55% were diffracted with the momentum parallel to the incoming beam. This results in the splitting ratio close to 1:3.

Figure 4.9 shows a plot of diffracted intensities measured at $\Delta\theta = 0$ as a function of crystal thickness. It is evident that a splitting ratio of 1:1 can also be obtained by probing the crystal at a thicker part i.e. 42.7 μm or 53.3 μm. At these crystal positions the Pendellösung fringes are blurred due to the unequal absorption of the wavefields in the crystal [46]. This effect reduces the stability demands on the incident beam but on the other hand the loss of intensity due to absorption is more than 40%. Since the delay unit design uses two beam splitters the absorption losses need to be minimized by working at the thinner (below 25 μm) part of the crystal.

It is worth mentioning that a slight change of the crystal position results in a significant changes of the diffraction profile and consequently the splitting ratio. For instance, the change in the beam height of 0.2 mm will affect the ratio of split beams from 1:1 to 1:3. Thus, the beam splitter requires proper alignment and stabilization of the incoming beam.

The beam splitting capabilities of the Si(553) Laue crystal were investigated at E = 12.4 keV with undulator radiation of the beamline PETRA 1. The experiment was performed with the crystal arrangement shown in figure 2.5. The first beam splitter crystal at the position SP1 was moved out of the beam, restricting

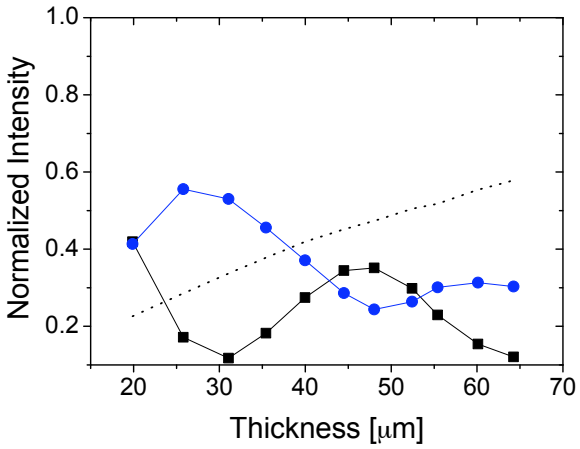

Figure 4.9: Variations of the forward diffracted(circles) and reflected (squares) beam intensities at 8.39 keV as a function of the beam splitter thickness. The data were normalized to the incident intensity. The part of the intensity absorbed by the crystal at 8.39 keV is indicated by the dotted line.

the beam to travel only through the lower branch. The beam size was set to 500 × 500 μm^2 and the incident beam divergence was filtered out by the anti-parallel (+n,+n) arrangement of Bragg crystals at the positions BC5 and BC6. The measured intensities were normalized to the monitor intensity, recorded upstream the crystal SP2.

The oscillatory behavior of the diffracted intensities as a function of the thickness of the crystal SP2 is shown in figure 4.10. Since the two beams diffracted by the splitter were measured with two different APD detectors, the splitting ratio cannot be precisely determined. In agreement with dynamical theory [21] the Pendellösung period Λ_l increases with the energy. Having a large Λ_l is of benefit for the delay unit because it puts less demand on the incident beam stabilization. Additionally, at E = 12.4 keV the absorption length for silicon is more than 3 times larger than at E = 8.39 keV and hence the absorption losses are much smaller.

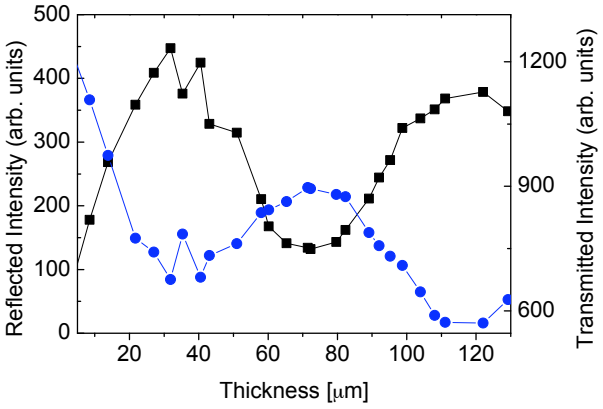

Figure 4.10: The Pendellösung effect at E = 12.4 keV determined with the Si(553) beam splitter. The reflected (squares) and forward diffracted (circles) intensities correspond to the left and right hand side axis, respectively.

4.1.4 Overall throughput

The performance of the Si(511) delay unit optics in the two branch configuration has been verified with 8.39 keV undulator radiation at the ID10C beamline of the ESRF (cf. section 3.5). The crystal arrangement of the delay unit is again shown in figure 4.11. To optimize the throughput of the delay unit all crystals were aligned to the angular position providing maximum reflectivity. The throughput T_M was obtained from the ratio of the X-ray intensity measured by the APD detector located upstream and downstream of the delay unit, i.e. $T_M = I_1/I_0$

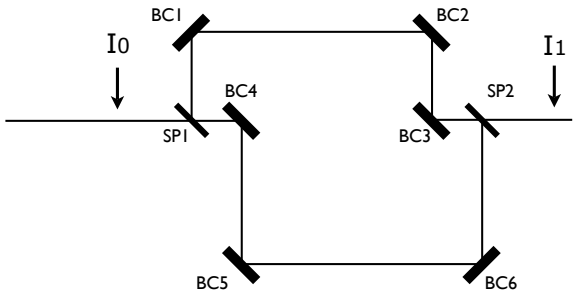

Figure 4.11: Crystal arrangement of the delay unit in the two-branch configuration.

The throughput value obtained with the Si(333) monochromator located upstream the delay line is $T_M = 6 \cdot 10^{-3}$. It is important to note that the diffraction properties of the Si(333) reflection are the same as for the Si(511). In addition, the incident radiation was well collimated by the slits located upstream of the delay unit. Therefore, the transmitted flux measured in this configuration can be mainly attributed to the performance of the delay unit optics. The calculated performance (based on ray tracing [35] and including absorption) gives a comparable value of the throughput (see table 2.3). The transmission value of the delay unit optics measured with a Si(111) beamline monochromator is $T_M = 2.7 \cdot 10^{-4}$. Since the wavelength bandpass of a Si(111) monochromator is 16 times larger than the one for Si(333), one expects in this case a smaller value for the delay

Table 4.1: Measured T_M and calculated T_{CALC} values of the delay unit throughput obtained under various conditions i.e energy E, pre-monochromatization (MONO) and incident divergence Ω. The calculated values were corrected for the x-ray absorption in air. T_{CORR} denotes the measured throughput values corrected for the x-ray absorption in air.

hkl	E [keV]	MONO	Ω [μrad]	T_M	T_{CORR}	T_{CALC}
511	8.39	Si(333)	17	$6.0 \cdot 10^{-3}$	$6.6 \cdot 10^{-2}$	$6.8 \cdot 10^{-2}$
511	8.39	Si(111)	17	$2.7 \cdot 10^{-4}$	$3 \cdot 10^{-3}$	$2.9 \cdot 10^{-3}$
553	12.4	Ge(220)	6.0	$1.2 \cdot 10^{-8}$	$2.4 \cdot 10^{-8}$	$9.9 \cdot 10^{-5}$

unit throughput[2]. The results of the throughput measurements are summarized in table 4.1. The measured throughput is in very good agreement with the calculated values. It should be noted, however, that a higher value for the throughput could be expected with Bragg beam splitters (cf. section 2.4.1.4). The X-ray beam splitter in Laue geometry acts as a prism dispersing wavelengths into angles. Any increase of the beam divergence, introduced by the first beam splitter SP1 is filtered by the (+n,+n) configuration of the crystals BC1 and BC2, leading to a decrease of the overall throughput. The effects of the Laue-Bragg geometries on the performance of the delay unit are discussed in appendix A.3.

The preliminary performance of the second set of crystals, i.e. Si (553) in the same crystal configuration of the delay unit was characterized at the beamline PETRA 1. The measurements were performed at 12.4 keV with an incident beam divergence of 6 μrad. The monochromatization of $\Delta\lambda/\lambda = 1.45 \cdot 10^{-4}$ was achieved with the beamline double crystal monochromator C(111) - Ge(220), in horizontal scattering geometry. The measured value for the transmission was $T_M = 1.2 \cdot 10^{-8}$. The low value of T_M it is caused by the source characteristics. The incident beam divergence is more than twice larger than the angular acceptance of Si(553) at 12.4 keV (i.e 2.33 μrad). In addition, the wavelength

[2]The calculated throughput is higher than the one listed in table 2.3. This is due to the collimation effects of the slits of the ID10C beamline which are not included in calculations of table 2.3.

bandwidth of photons selected by the beamline monochromator C(111) - Ge(220) is significantly larger than the bandwidth of Si(553) i.e $\Delta\lambda/\lambda = 2.33 \cdot 10^{-6}$. The calculated throughput using ray tracing yields a value of $T_{CALC} = 9.89 \cdot 10^{-5}$. The reason for the lower throughput[3] might be multiple Bragg diffractions [21] in the crystals[4]. Further performance tests at this energy are required to quantify the effect of multiple scattering. The results are also listed in table 4.1.

[3] this value is probably also compromised by the experimental procedure.
[4] multiple diffraction effects were not included in the ray tracing.

4.1.5 Stability

Knowledge on the stability of the delay unit components is essential to conduct pump-probe and correlation spectroscopy experiments in the future. Both aforementioned techniques will be performed in a stroboscopic manner. Therefore, the device should provide a stability such that no crystal realignment is necessary during the acquisition time at a chosen delay time.

Figure 4.12 shows the intensity variation of the Si(333) channel-cut monochromator measured with 8.39 keV at ID10C. The crystal was located 0.65 m upstream the delay unit (cf. section 3.5.4). The intensity was monitored by the scintillator counter detector, located right before the first crystal of the delay unit. The data was corrected for the variations of the storage ring current. The data clearly demonstrate that the intensity varies with time. This is likely due to temperature instabilities of the environment.

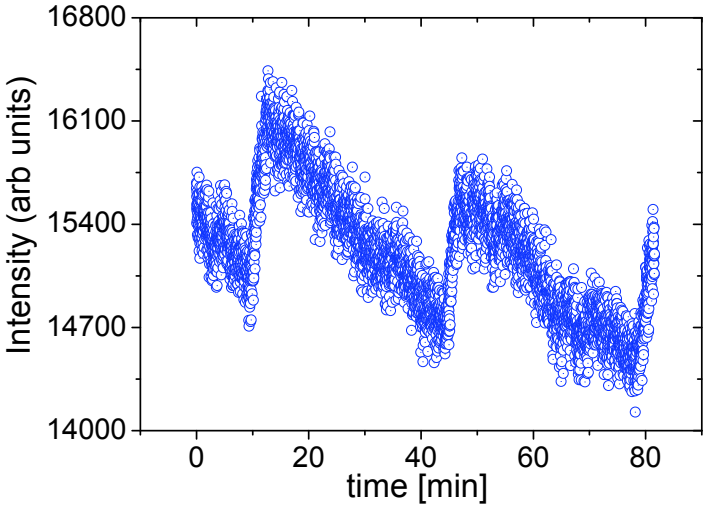

Figure 4.12: Stability of the Si(333) monochromator located upstream the delay unit.

Figure 4.13 shows stability measurements of the delay line. The intensity variations were recorded with the avalanche photodiode detector placed right behind the delay unit. The detector counts were normalized to the intensity collected by

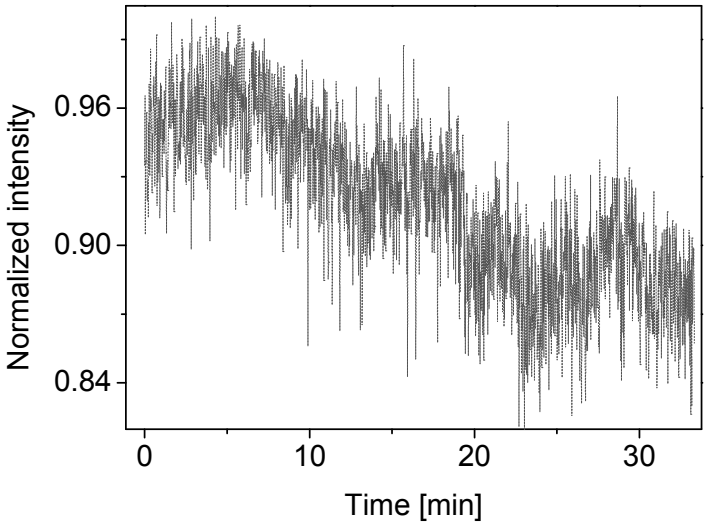

Figure 4.13: Stability of Si(511) delay unit optics measured at ID10C.

ionization chamber IC1, located behind the Si(333) channel-cut monochromator.

Without stabilization of the Si(333) monochromator, the loss in transmitted intensity is less than 10% over 30 minutes (see figure 4.13). Due to the combination of non-dispersive and dispersive crystal arrangements (cf. section 4.1.2) the outgoing beam intensity decays faster than the incident beam intensity.

Stability measurements at E = 12.4 keV in the two branch configuration were carried out at the beamline PETRA 1 (cf. section 3.5.3). The Darwin width of the Si(553) reflection at 12.4 keV is only 2.33 μrad. This is more than 3 times smaller than for the Si(511) crystals at 8.39 keV. Crystals with such a small reflection width place much higher demands on temperature stabilization of the delay unit components. Following the discussion in section 2.4, the optimal performance of the delay unit will be guaranteed with a temperature stabilization of $\Delta T < 0.3\ K$.

Figure 4.14 shows the normalized intensity measured by the APD detector, located downstream of the delay unit. Over 30 minutes of operation the intensity stability is acceptable indicating no need for realignment of the delay unit optics.

After that time the intensity decays since neither temperature stabilization nor active feedback was implemented in the setup.

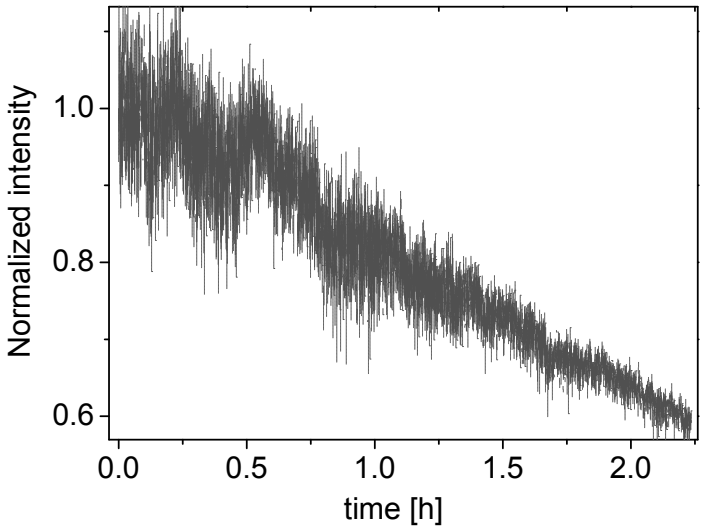

Figure 4.14: Stability of the Si(553) delay line optics measured at beamline PETRA 1.

4.1.6 Summary

The performance of the optical components of the delay unit was characterized at bending magnet and undulator sources. The measured rocking curve widths of the Bragg crystals are in excellent agreement width the theoretically expected values, thus indicating the high quality of the Bragg components. The performance of the X-ray beam splitters was verified and a splitting ratio of 1:1 was achieved utilizing Si(511) and Si(553) reflections in Laue geometry. The maximum achieved splitting ratio at E = 8.39 keV is 1:3. The overall efficiency of the setup at 8.39 keV is 0.6% with $\Delta\lambda/\lambda = 8.6\times10^{-6}$ bandwidth of the incident undulator beam. This value is in very good agreement with the theoretically expected value. The throughput of 1.2×10^{-8} was achieved for the Si(553) optics at E = 12.4 keV. The system shows good mechanical stability at the aforementioned energies.

4.2 Delay time measurements

4.2.1 Introduction

Measuring time delays introduced by the delay unit requires a fast diagnostics tool. In the preliminary experiments at DORIS III an APD detector with a large active area was employed (cf. section 3.4.2). An ultra-fast APD was utilized during the performance tests at the ESRF (cf. section 4.2.3). Since information about the performance of a detector is essential for the determination of the time resolution of the delay unit, the time resolution of the aforementioned detectors were measured prior to the delay time experiments.

Figure 4.15 shows the time response of the ultra-fast detector to a 8.39 keV beam during 4 bunch operation of ESRF. The time interval between the photons detected by the APD and the storage ring bunch clock signal[5] was measured by a chain of CFD/TAC/ADC electronics (cf. section 3.4).

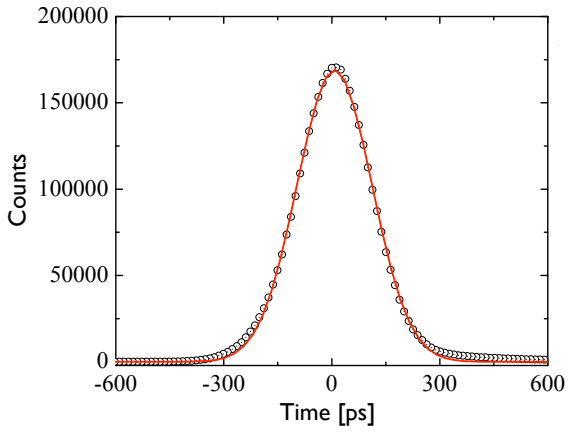

Figure 4.15: Temporal response of the ultra-fast APD detector to 8.39 keV radiation measured at ID10C. The width of the peak is 235 ps.

The result shown in figure 4.15 corresponds to the distribution of events recorded as a function of the time interval. It can be also interpreted as the probability distribution of detecting a photon at a time t.

[5] the signal synchronized to the frequency of the synchrotron.

One can define the resolution of a detection system (i.e. APD detector and the bunch clock signal) as being given by the width (FWHM) of the measured time pattern. Since the measured pattern shows a slight asymmetry, the peak position t_0 and its intensity A is extracted by using an asymmetric Gaussian function defined by

$$f(t) = A \cdot \begin{cases} \exp\left(-\frac{(t-t_0)^2}{2r^2\sigma^2}\right) & \text{if } t < t_0, \\ \exp\left(-\frac{(t-t_0)^2}{2\sigma^2}\right) & \text{if } t > t_0 \end{cases} \tag{4.1}$$

where r is the asymmetry parameter. The standard deviation σ in expression (4.1) is related to time resolution ΔT (FWHM) according to

$$\Delta T = \sqrt{2ln(2)} \cdot \sigma \cdot (1 + r) \tag{4.2}$$

For an asymmetry parameter $r = 1$ the expression (4.2) simplifies to a symmetric Gaussian function and $\Delta T = 2\sqrt{2ln(2)} \cdot \sigma$.

The solid line in figure 4.15 is the result of the fit of equation (4.1) to the measured time pattern which yields the time resolution of the detection system $\Delta T = 235$ ps. This value contains contributions from the electron bunch length and the detector resolution. Using a length (FWHM) of the electron bunch[6] of $\Delta T_B = 140$ ps one finds for the resolution of the detector ΔT_D :

$$\Delta T_D = \sqrt{\Delta T^2 - \Delta T_B^2} \tag{4.3}$$

The result $\Delta T_D = 189$ ps is in good agreement with the expected value of 190 ps [48]. It should be noted that the electron bunch length depends on the current of the storage ring which influences the width of the measured peak[7].

In time delay experiments the photons delayed by the upper and the lower

[6] The time pattern was recorded at 35 mA of the ESRF storage ring. This corresponds to ΔT_B of 140 ps [47].

[7] This change is however very small. During the 4 bunch mode of ESRF and using $\Delta T_D =$ 189 ps one can expect only 22 ps change of the total width of the measured peak.

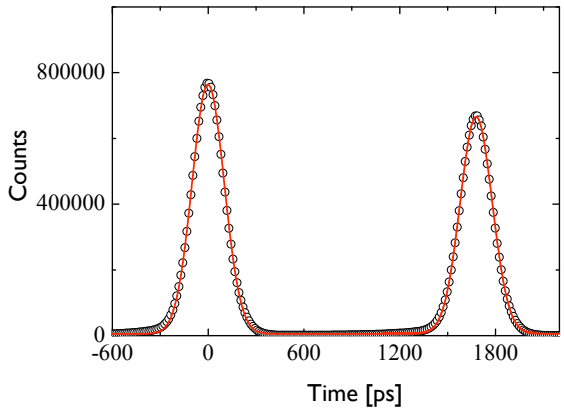

Figure 4.16: Temporal response of the ultra-fast APD detector measured at ID10C during the experiments with the two-branch configuration of the delay unit.

branch are detected by the APD detector. Therefore, the measured time pattern reveals two peaks, as illustrated in figure 4.16. The delay time between the peaks can be obtained by the fit with two asymmetric Gaussian functions, defined by

$$f(t) = f_1(t) + f_2(t) \tag{4.4}$$

where the f_1 and f_2 are given by equation (4.1).

The measured delay time τ_m is the difference between the positions of the measured peaks i.e.

$$\tau_m = t_{01} - t_{02} \tag{4.5}$$

Since both pulses are delayed with respect to the direct beam the measured τ_m gives a relative delay time.

Although the resolution of the detection system (i.e the FWHM of the measured peak) is 235 ps the relative accuracy of the measured delay time τ_m is much better. It can be determined with an accuracy of typically 10% of the resolution of the detection system ΔT. Consequently the expected relative resolution is

$$\Delta\tau_m \simeq 0.1 \cdot \Delta T \tag{4.6}$$

which corresponds to 23.5 ps for $\Delta T = 235$ ps.

The resolution value for the large active area APD utilized for the preliminary tests at DORIS III was $\Delta T = 860$ ps.

4.2.2 Preliminary tests at DORIS III

Preliminary delay time measurements at E = 8.39 keV have been carried out at beamline C of DORIS III during 5 bunch mode. The delay unit was operated in the pump-probe (cf. figure 3.9a) and the two-branch (cf. figure 2.5) configuration. The detector used in this preliminary experiments was a large active area APD (cf. section 3.4.2).

Prior to the time delay experiments the performance of the detection system was investigated. Figure 4.17 shows the resulting time pattern. A time resolution $\Delta T = 860$ ps was obtained by fitting the peak defining time t = 0. The detector resolution ΔT_D of 848 ps was obtained using expression (4.3) and using the length of the electron bunches in the DORIS III storage ring $\Delta T_B = 146$ ps [49].

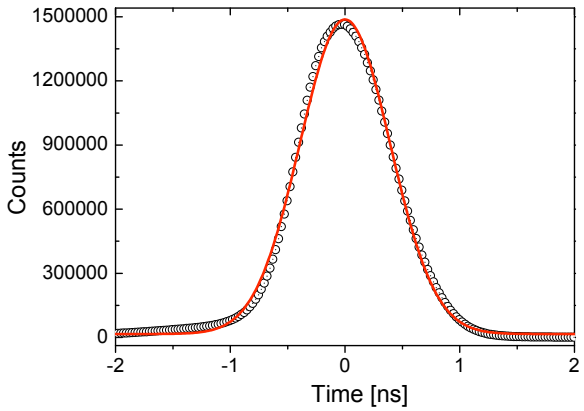

Figure 4.17: Time response of the 10 × 10 mm^2 APD detector to 8.39 keV X-rays at 5 bunch mode of DORIS III. The red line is a fit of equation (4.1) the data and yields $\Delta T = 860$ ps.

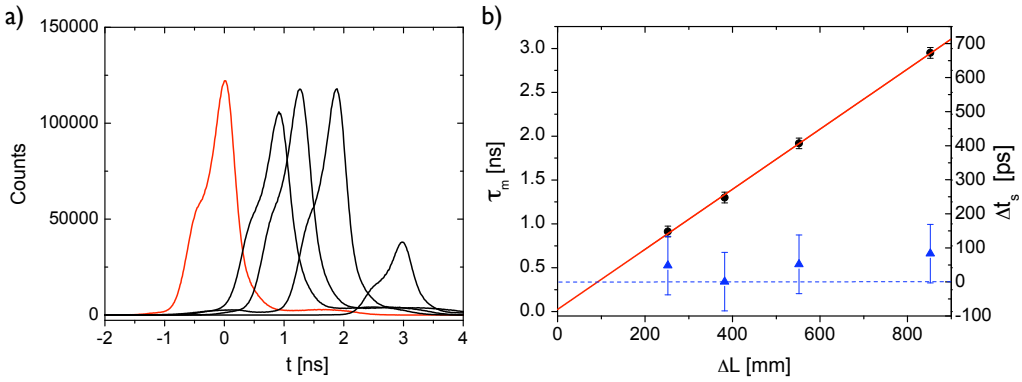

Figure 4.18: a) Time pattern of the X-ray pulses delayed by the delay unit (black lines) and the direct beam (red line). b) Measured delay time τ_m as a function of the applied delay path length difference ΔL denoted by black circles. Blue triangles correspond to the discrepancy $\Delta t_s = \tau_m - \Delta L/c$ between the applied τ_c and the measured τ_m time delay. The blue dashed line denotes $\Delta t_s = 0$. The red solid line is a fit to the data.

Figure 4.18 shows the first results of the delay time measurements performed in a X-ray pump X-ray probe scheme. The arrival time of the delayed and the direct beam was measured separately by blocking the direct beam and the delay arm path, respectively. The delay time was varied during the experiment by translating the main aluminium plate to four different positions. The resulting time patterns are shown in figure 4.18a. The arrival time of the signal changes as a function of applied path length difference. This is quantified in figure 4.18b. A maximum delay time of 2.95 ns was achieved. The measured intensity varied for the different settings of the delay unit. This effect is attributed mainly to crystal alignment problems, that occurred during the experiments[8]. Moreover, each peak reveals a small shoulder, caused by the detector electronics. Therefore, the delay time analysis was restricted to finding the maximum of each measured peak and the corresponding delay time τ_m was calculated from expression (4.5).

The (red) solid line in figure 4.18b corresponds to a least square fit to the

[8] At this stage of time delay experiments the throughput of the delay unit varied with the experimentally applied time delay. As it is shown in the next section, the alignment procedure of the delay unit optics was improved. After that, the throughput was less sensitive to the applied time delay.

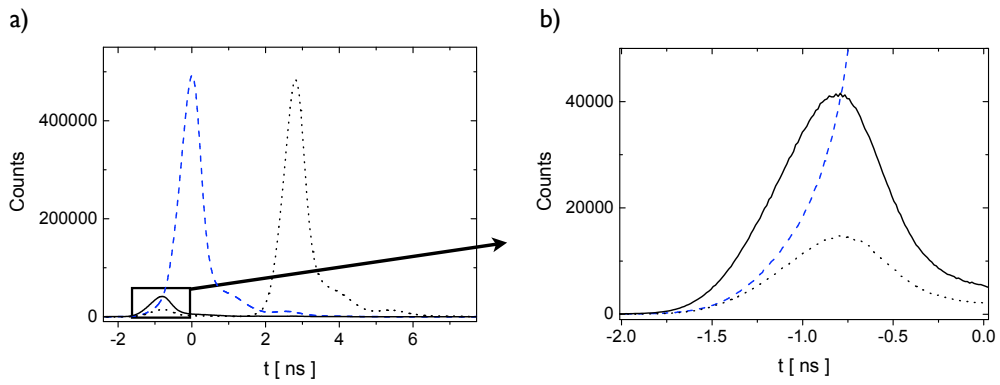

Figure 4.19: Time pattern of X-ray pulses delayed by the delay unit in the two-branch configuration. Blue and black dotted lines correspond to the photons delayed by the lower and upper branch of the delay line, respectively. The black line corresponds to high energy photons not delayed but passing straight through the delay unit.

measured data. It reveals a slope of $(3.42 \pm 0.18) \cdot 10^{-3}$ ns/mm and a fine offset of 25 $\pm$98 ps. The latter value accounts for a constant offset in the measured delay times. It is considerably larger then the expected value[9]. It is believed that the obtained offset is not related to mechanical misalignment of the delay unit and it is mostly determined by the resolution of the detection system. The deviations Δt_s calculated for each delay time and corrected for the offset value are indicated by the blue triangles in figure 4.18. The resulting values exhibit the maximum value of 83 ps with a mean of 46 ps, which is within the resolution ($\Delta\tau_m \simeq 86$ ps estimated via equation (4.6)) of the detection system.

Figure 4.19a shows the time pattern of the X-ray beam recorded with the delay unit arranged in the two-branch configuration. Since both branches introduce a time delay to the split photon beams coming from the storage ring, the time pattern reveals two strong peaks separated in time by 2.82 ns. The third, much weaker peak, recorded simultaneously with the delayed photons of the lower branch, originates from the direct beam (i.e. non delayed photons). Figure 4.19b shows a zoom of the time pattern. The low countrate of the peak is related to

[9] in the pump-probe configuration the translation of the crystal SP2 allows to vary the offset value up to 0.3 ps.

the lower efficiency[10] of the APD at higher (than 8.4 keV) energies and to the absorption by the crystals BC4 and BC3 (see figure 3.9b). The origin of this peak was clarified by recording the time pattern after blocking both paths of the delay unit. The solid (black) line in figure 4.19 shows the resulting time pattern. The time structure of the weak peak is the same as that for the electron bunches in the storage ring. Therefore, by measuring its position the absolute delay time can be obtained.

In conclusion: The first attempt to delay X-rays from a storage ring source using the delay unit was successfully undertaken at DORIS III. Delay times up to 2.95 ns were achieved with 0.046 ns resolution. In this preliminary tests the time resolution was limited by the detector electronics and misalignment of the delay unit optics. The value of the error in the determination of the delay time is by far dominated by the resolution of the used detection system. Therefore, further experiments with a detector of higher temporal resolutions are required.

4.2.3 Performance tests at ESRF

In order to further test the performance of the delay unit, the experiments with an ultra-fast APD detector at ESRF were conducted. The experiment has been carried out at beamline ID10C during 4 bunch mode operation of the storage ring. The delay unit was arranged in the two-branch configuration. The incident beam size on the ultra-fast APD detector was defined by the slit system located upstream of the delay unit , horizontally and vertically to approximately 500×400 μm^2. The incident countrate was kept below 400 kHz to minimize dead time effects[11]. The analysis of the detector performance, discussed in section 4.2.1, yields a time resolution of the detection system of $\Delta T = 235$ ps, which should allow to measure the delay time with the precision of $\Delta\tau_m \cong 23.5$ ps.

[10]The efficiency of an APD depends on its effective thickness, which is defined as the part of the detector in which X-ray absorption lead to electron amplification process.

[11]The precision of the electronics is the highest at low count rates

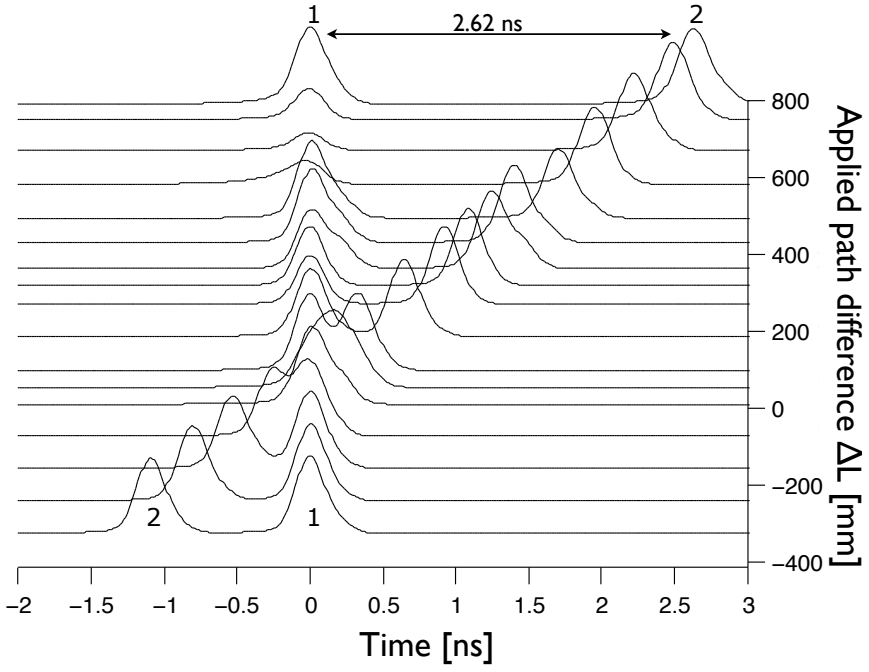

Figure 4.20: Time patterns corresponding to delayed X-ray pulses measured as a function of applied path difference ΔL between the two branches. The maximum measured τ_m is 2.62 ns.

Figure 4.20 shows a plot of the time patterns recorded at various settings of the delay unit. For the sake of clarity the position of the X-ray pulse delayed by the lower branch of the delay unit was offset to t = 0. The time patterns were recorded simultaneously for photons delayed by the upper and the lower branch. In order to obtain statistically good data, each time pattern was measured over approximately 30 min. The shape and the peak intensity varies for the first four time delay patterns (corresponding to the longest delay times). The peak shape can be influenced by the detector electronics. The peak intensity variation is due to a non ideal alignment procedure of the delay unit. The values of the delay time τ_m were obtained by the fitting procedure described in section 4.2.1. For the delay unit settings corresponding to delay times smaller than 100 ps the arrival time of the delayed photons was measured separately for each branch. At a path length difference ΔL of 792.75 mm the time pattern reveals two equally intense

X-ray pulses separated by 2.62 ns. This corresponds to the maximum delay time τ_m achieved in the experiment. The delay path difference ΔL was successively changed during the experiment with variable steps from 80 mm (276 ps) to 22 mm (73 ps).

It was shown in section 2.3 that the design of the setup allows to choose which of the split pulses arrives at the sample position first. This was achieved by moving the translation stage from the position of 2 mm to 200.5 mm which changed the path difference ΔL from 792.75 mm to 0 mm. At the latter position the paths of both branches have the same lengths and the resulting time pattern reveals only one peak centered at delay time 0. Further translation to 300 mm reversed the position of the pulses in time. The paths length difference at this position is 402 mm and corresponds to 1.34 ns delay. The exchange of pulse position corresponds to the negative values of ΔL and $\Delta\tau_m$, as demonstrated in figure 4.20. In contrast to the results of the preliminary tests at beamline C, described in the pervious section, the alignment procedure was improved by a precise alignment of the granite support to the vertical scattering plane. As a result, the variations of the maximum peak intensity at different setting of the delay unit (i.e applied delay times τ_c) were minimized.

Figure 4.21 shows the plot of the measured delay time τ_m as a function of the applied path length difference ΔL. The (solid) red line is a least square fit to the data, which yields a slope of $(3.35\ \pm 0.01) \cdot 10^{-3}$ ns/mm and the offset of -4.3 $\pm$3.2 ps. The linearity between the applied path length and the measured delay time shows the high quality of the mechanics and promises simple operation according to equation (2.10) without the need for higher order correction terms when setting the path length difference. The value for the offset decreased compared to the value obtained with the large area APD detector[12]. This indicates that the resolution of the detection system has in fact a significant influence on the determination of the offset and delay time τ_m.

The delay time error $\Delta t_s = (\tau_m) - \Delta L/c$ was extracted for every data point.

[12]the APD detector used during delay time experiments at beamline C, described in the previous section.

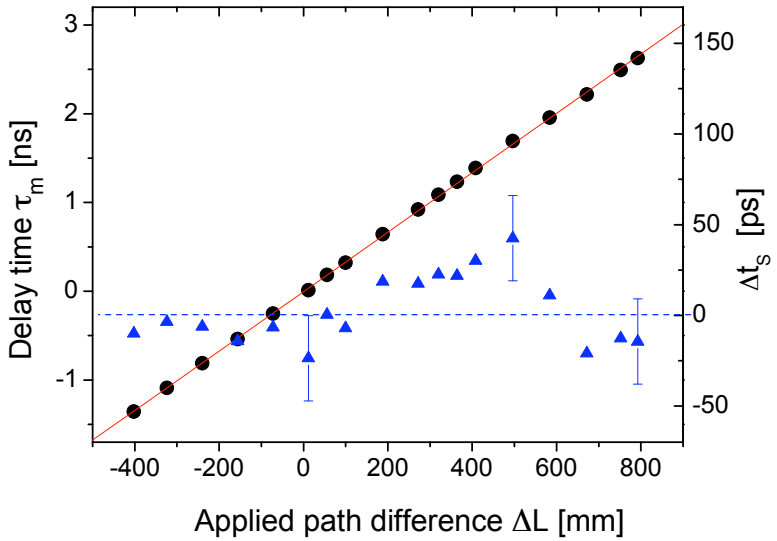

Figure 4.21: Measured delay time τ_c vs applied path difference ΔL. Negative values of ΔL and τ_m denote inversed photon beam arrival times (see text for explanation). The solid red line is a linear fit to the data. The difference between the applied path length difference and the measured delay time is quantified by the triangles. For clarity reasons the relative detector resolution $\Delta\tau_m = 23.5$ps is indicated for selected data points.

The results (corrected for the offset) are also shown (blue triangles) in figure 4.21. The mean delay time error is 16.7 ps. The maximum deviation was found to be less than 43 ps.

In oder to test the reproducibility a second delay time measurements was carried out. This time the translation unit was moved from 300 mm back to the 11.5 mm position. The fit to the data yielded an offset of 7.9 ±8.4 ps. The delay time error Δt_s was corrected for this offset and the results are plotted in figure 4.22 (red filled circles). The mean error is 12.5 ps. For comparison the errors of the previous run are also plotted (blue triangles) in figure 4.22. The averaged mean error for the two measurements is 15.4 ps. This is close to the relative detector resolution of 23.5 ps.

A measure of the reproducibility of the setup is the difference in the mean

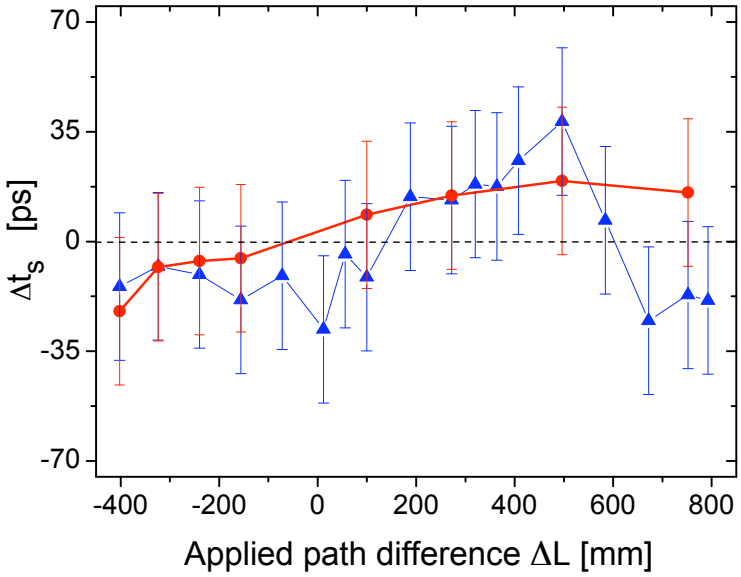

Figure 4.22: Repeatability of the measured delay time obtained from the deviation Δt_s measured for each position of ΔL in forward (blue traingles) and reverse (red circles) direction. The negative values correspond to the data obtained when the photon pulses positions were exchanged. The dashed line denotes the position where $\Delta t_s = 0$.

error between the two measurements shown in figure 4.22. The mean value for the reproducibility is given by

$$\Delta t_{rep} = \frac{\sum_{i=1}^{N}(\Delta t_{si}^{1} - \Delta t_{si}^{2})}{N} \tag{4.7}$$

and yields 12.3 ps.

It is important to state that the achieved time resolution of 15.4 ps does not represent the intrinsic value of the delay unit. Much better time resolutions could be achieved with a higher resolution of the detection system. A detector with a time resolution below the pulse duration would improve the analysis of the measured patterns. In addition, it would allow a simultaneous measurement of the two delayed pulses at a shorter delay than currently achievable. Furthermore,

Table 4.2: Achieved time resolution Δt_s and contributions from the mechanical accuracy of the $\Delta\tau_{mech}$ and temperature inaccuracies $\Delta\tau_{temp}$.

Δt_s [ps]	$\Delta\tau_{mech}$ [fs]	$\Delta\tau_{temp}$ [fs/K]
15.4	6.67	100

using detector electronics with a smaller dead time would make the measurements more efficient and less sensitive to the long term instabilities of detector electronics.

The limits for the intrinsic time resolution of the current setup is given by the mechanical components of the delay unit and the temperature stability. The positional accuracy of the central translation unit (i.e. the main aluminium plate) is 0.5 μm, which allows one to change the delay time with a precision of not better than $\Delta\tau_{\mathrm{mech}}$ =6.67 fs (in the two-branch configuration). Since the delay unit operates in ambient conditions, a change in temperature affects the position of the delay unit crystals due to the thermal expansion of the main aluminum plate. The expected effective change $\Delta\tau_{\mathrm{temp}}$ in the measured delay time for $\Delta T = 1$ K is 100 fs. Table 4.2 summaries the factors affecting the total resolution.

From the obtained results one can conclude that the time resolution of the detector and its electronics are the limiting factors for the diagnostics measurements of the delay unit up to now. It was shown that using the detector with higher time resolution[13] improves also the precision of measured delay time. The achieved value of 15.4 ps is more than 3 orders of magnitude larger than the intrinsic time resolution of the delay unit. The contributions from the mechanical inaccuracy and temperature effects are negligible unless the resolution of the diagnostics will become higher than hundreds of femtoseconds.

[13] compared to the measurements at beamline C described in the previous section.

4.2.4 Summary

First time delay measurements have been performed utilizing two different delay unit schemes. The preliminary tests at DORIS III were carried out in the pump-probe delay unit configuration. The maximum delay time of 2.95 ns was achieved with 46 ps resolution. The delay unit in the two-branch crystal configuration was tested at ESRF. The maximum delay time of 2.62 ns was achieved with 15.4 ps resolution. The reproducibility was 12.3 ps. The performance of the delay unit was verified with the Si(553) optics (not shown) at PETRA II, indicating the feasibility of performing time delay experiments with 12.4 keV X-rays. Delay times up to 2.66 ns have been achieved.

4.3 Coherence preservation of the delay unit

4.3.1 Introduction

The coherence properties of 3$^{\text{rd}}$ generation sources can be described by the transverse ξ_t and longitudinal ξ_l coherence lengths and the coherent flux I_C. The transverse coherence length ξ_t is a measure of the phase correlations between the waves of a monochromatic source of finite size in the plane perpendicular to the direction of propagation [18]

$$\xi_t = \frac{\lambda}{2} \cdot \frac{R_s}{s} \tag{4.8}$$

where R_s is the distance from the source and s is the source size.

The longitudinal coherence length defines a phase relation of the emitted radiation in the propagation direction. It is related to a spectral purity of the source according to [18]:

$$\xi_l = \frac{\lambda}{2} \cdot \frac{\lambda}{\Delta\lambda} \tag{4.9}$$

The temporal coherence properties of the beam can be described by a coherence time τ_0, which is related to the longitudinal coherence length by [50]

$$\xi_l = \tau_0 \cdot c \tag{4.10}$$

where c is the speed of light. The meaning of τ_0 is the time over which the phase of the radiation undergoes no fluctuation.

In order to produce a coherent beam at a 3$^{\text{rd}}$ generation source, the emitted

undulator beam has to be spatially and spectrally filtered. In practice the spatial filtering can be done with a pinhole-aperture or a set of slits set in such way that the slit size is smaller than the transverse coherence length in the vertical and horizontal directions[14]. Narrowing the bandwidth $\Delta\lambda$ of a source is usually achieved by utilizing a monochromator crystal or a mirror in an experimental setup. Thus the conditions for the coherent illumination can be fulfilled, however, at the expense of photon flux. The fraction of the undulator flux that is spatially (transversely) coherent at wavelength λ is given by

$$I_C = \left(\frac{\lambda}{2}\right)^2 \cdot B \tag{4.11}$$

where B is the brilliance of the source defined as a number of photons per second, per mm^2, per mrad^2 per 0.1% source bandwidth.

As it was pointed out is section 1.3 the delay unit will find an application in the split-pulse XPCS technique [13]. The main requirement for this technique is that the investigated sample must be illuminated coherently. Optical components inserted into a beam path might affect (degrade) the coherence properties of the radiation, meaning that they might reduce the visibility of any diffraction or interference experiment. As it was presented in previous sections, the delay unit utilizes up to eight optical components. In order to perform the split-pulse XPCS experiments at future XFEL sources the influence of the delay unit optics on the coherence of undulator radiation was investigated at beamline ID10C at ESRF. The coherence properties of the beam were investigated initially by taking Fraunhofer diffraction patterns from a rectangular slit aperture. A slit system (cf. section 3.5.4) was placed downstream of the delay unit and the diffraction pattern was recorded with a point detector. In the second stage of the experiment, a speckle pattern was recorded from a disordered sample. The evaluation of the degree of coherence of the beam was based on a statistical analysis of the measured speckle patterns [51, 52].

[14]The value for a transverse coherence length might differ in the horizontal and vertical plane due to the source asymmetry.

4.3.2 Single slit diffraction measurements

In this section the coherence properties of the beam passing through the delay unit are quantified by Fraunhofer diffraction measurements from a single rectangular aperture. The concept of the visibility of Fraunhofer fringes is introduced. The influence of the resolution and the stability of the experimental setup on the fringe visibility is discussed. Finally, the results of the Fraunhofer diffraction measurements with the delay unit arranged in various crystal configuration are presented.

4.3.2.1 Fraunhofer diffraction

A simple[15] method of estimating the coherence properties of monochromatized radiation is the measurement of Fraunhofer diffraction from a pinhole or rectangular aperture. If the aperture is illuminated coherently (i.e. its size is smaller than the ξ_t in vertical and horizontal plane) an interference pattern is formed on the detection plane located in the far field. The Fraunhofer diffraction pattern from a rectangular aperture is defined by [50]:

$$I_s(q_x, q_z) = \mathrm{sinc}^2(\frac{s_x}{2}q_x) \times \mathrm{sinc}^2(\frac{s_z}{2}q_z) \tag{4.12}$$

where $q_x = 2\pi x/\lambda L$ and $q_z = 2\pi z/\lambda L$ are the values of scattering vectors (in the small angle approximation) along the x and z axis, respectively. The parameters s_z and s_x are the vertical and horizontal slit sizes and L is the distance separating slit and detector positions. From equation (4.12) for $q_x = 0$ one finds that the FWHM of the principal maximum at $q_z = 0$ is

$$D_S = 1.12 \cdot \frac{\lambda}{s_z} \cdot L \tag{4.13}$$

Expression (4.13) allows one to deduce a speckle size in a XPCS experiment.

[15] a more quantitate way of investigating coherence properties of radiation is by performing Young double slits experiment [53].

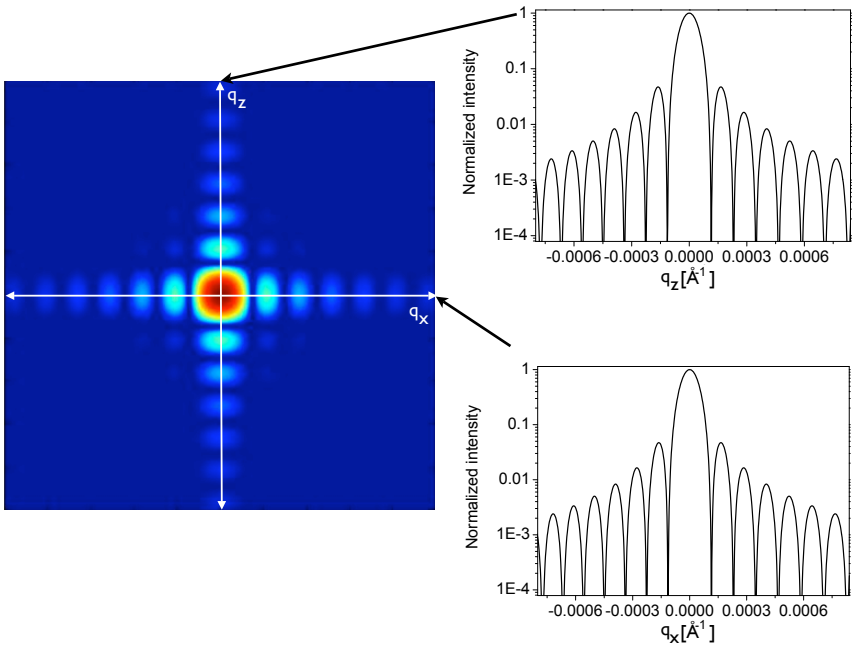

Figure 4.23: Calculated Fraunhofer diffraction pattern of a 5×5 μm^2 rectangular aperture. The two pattern on the right side represent cross sections of the 2D pattern along horizontal x and vertical z directions.

Figure 4.23 shows the Fraunhofer diffraction pattern calculated according to expression (4.12) for $\lambda = 1.478$ Å and a slit size of 5×5 μm^2 located $L = 1.85$ m in front of the detection plane. The resulting pattern reveals oscillations with a gradually diminishing amplitude. The visibility of these oscillations, which are commonly referred to as Fraunhofer fringes is defined by

$$V = \frac{I_{\max} - I_{\min}}{I_{\max} + I_{\min}} \tag{4.14}$$

where $I_{\max}$ is the intensity at the fringe maximum and $I_{\min}$ is an adjacent minimum. In an experiment, when the aperture is coherently illuminated, the measured interference pattern can be smeared out due to detector resolution or instabilities of optical components.

The Fraunhofer pattern expressed by equation (4.12) does not include the

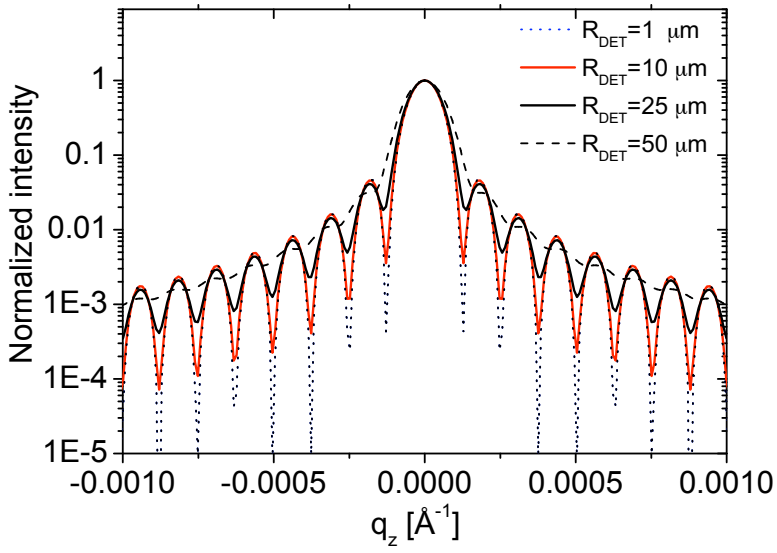

Figure 4.24: Calculated Fraunhofer diffraction pattern as a function of the detector aperture R_{DET}.

resolution of a detector, meaning that the beam diffracted by a slit is recorded at a point in the detection plane. In an experiment one uses a detector which has a finite size[16]. The point intensity recorded by the detector is integrated over this area. This in consequence leads to a decrease of the fringe visibility. This effect is demonstrated in figure 4.24. The red solid line shows the calculated pattern where $I_s(q_x = 0, q_z)$ in equation (4.12) is convoluted with a rectangular transmission function, corresponding to the detector resolution. It is evident that the highest resolution can be achieved with the smallest detector slits opening.

In order to account for the instability of an optical component the simple concept of a resolution function can be introduced. When the optical component experiences vibrations the effective source size increases. Using expression (4.8) one finds that the transverse coherence length will decrease and so will the visibility of the Fraunhofer pattern. The intensity distribution along the z axis of

[16]The minimum illuminated area is usually defined by a pixel size in 1D or 2D detectors or can be controlled by a set of slits in front of a point detector.

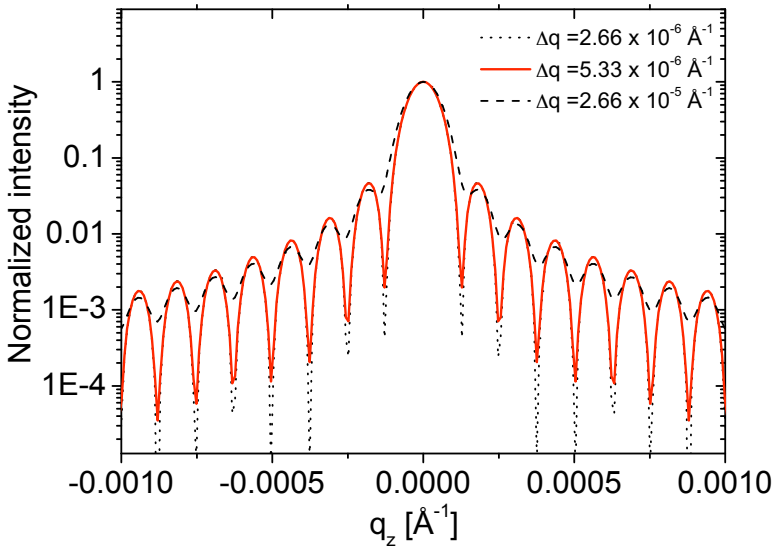

Figure 4.25: Calculated Fraunhofer diffraction patterns as a function of Δq (further details can be found in the text).

the detector plane $I(q_z)$ can be written as

$$I(q_z) = \int_{-\infty}^{\infty} \mathrm{sinc}^2(\frac{s_z}{2}q_0) \cdot \frac{1}{\sqrt{2\pi}\sigma} \exp(-\frac{(q_z - q_0)^2}{2\sigma^2}) dq_0 \qquad (4.15)$$

where the first term corresponds to the scattering intensity from a rectangular aperture, introduced in two dimensions by expression (4.12). The second term of equation (4.15) takes into account a spread of the scattering vector q in the detection plane due to the effective source size increase. For a Gaussian function the spread Δq equals $2\sqrt{2ln2}\sigma$. In case when the spread Δq is infinitely small the second term in equation (4.15) becomes a δ function. As the values of Δq increase the Fraunhofer pattern becomes more washed out, as depicted in figure 4.25. In effect, the second term of expression (4.15) serves as a resolution function for the Fraunhofer pattern.

Another effect that might affect the profile of the Fraunhofer pattern is the

asymmetry of the slits, shown in figure 4.26. The roller blade slits [43] used in the experiment have a longitudinal offset h of about 3 mm [54] between the blades. Due to the parallax effect one side of the Fraunhofer pattern differs from the other side [43]. To account for the slit asymmetry, s_x and s_z in the expression (4.12) are replaced with:

$$s_{xa} = s_x \pm xh/R_s \qquad s_{za} = s_z \pm zh/R_s \tag{4.16}$$

Figure 4.27 shows the calculated Fraunhofer pattern for three different values of the slit asymmetry. One can notice that this effect (at given experimental conditions) is of importance when the asymmetry is considerably larger than 3 mm. It was nevertheless included in the analysis of the experimentally obtained Fraunhofer patterns.

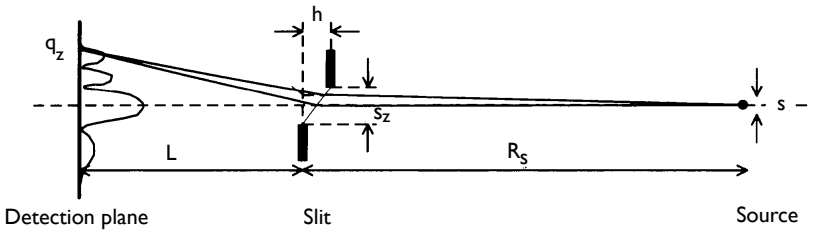

Figure 4.26: Schematic representation of the slit asymmetry h.

4.3.2.2 Alignment of two exit beams

The delay unit arranged in the two-branch configuration with a Laue crystal as a beam splitter produces two exit beams with a small angular mismatch (cf. section 2.4.1.6). The resulting interference pattern recorded at the detection plane, located behind the delay unit, will thus consist of two Fraunhofer patterns unless an alignment procedure involving crystal tilt stages is applied. That this is possible is shown in figure 4.28. It shows the 2D image recorded by a CCD detector located 1.85 m downstream of the delay unit arranged in the two-branch configu-

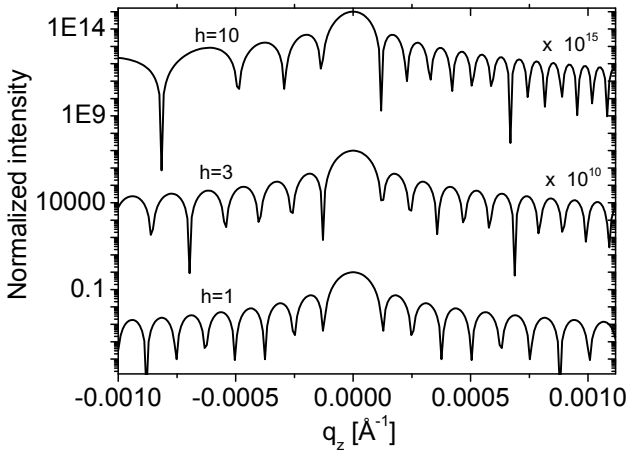

Figure 4.27: Calculated Fraunhofer diffraction patterns for experimentally given conditions as a function of the slit asymmetry h.

ration. The two Fraunhofer patterns arise from the diffracted beams of the upper and lower branch of the delay unit. Both patterns are displaced horizontally by using the BC3 and SP2 tilt stages. One can see that due to a successfully applied alignment procedure involving BC6, SP2, BC2 and BC3 crystals tilt stages the vertical angular offset between two exit beams was compensated. This type of alignment procedure was used to study the coherence properties of the delay unit in the two-branch configuration by means of Fraunhofer diffraction (cf. section 4.3.2.3.2).

4.3.2.3 Experimental results

The Fraunhofer patterns were obtained by recording the intensity diffracted by the rectangular aperture (i.e the rollerblade collimating slits) located 0.155 m downstream of the delay unit, as a function of the detector position in the horizontal x and vertical z planes (cf. section 3.5.4). The expected horizontal and vertical transverse coherence lengths (at the given experimental conditions) at the aperture position (i.e. $R_s = 63$ m from the source) are $\xi_{th} = 16$ μm and

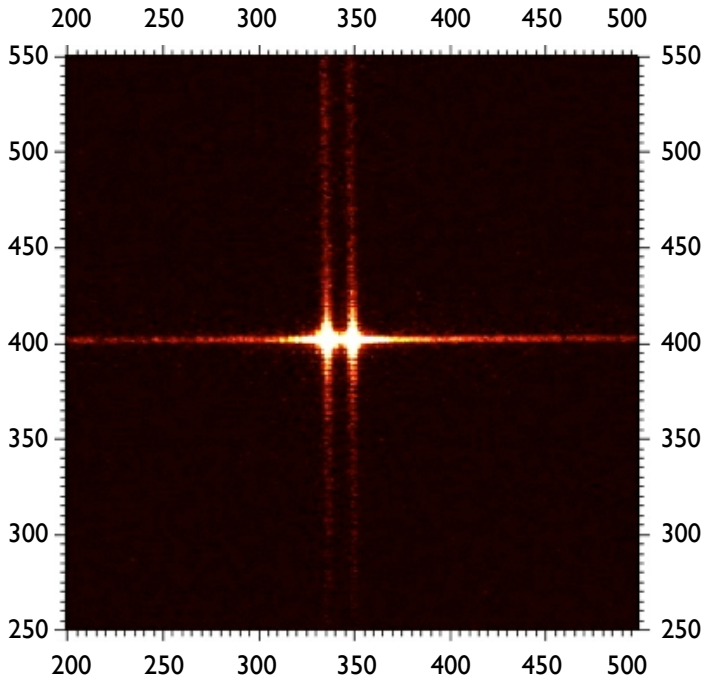

Figure 4.28: Two Fraunhofer diffraction patterns recorded with the delay unit arranged in the two-branch configuration. The axes are labeled by a CCD pixel number.

$\xi_{tv} = 202$ μm, respectively. The resolution of the detector was 25 μm, which was determined by the size of the slit system, located right in front of the detector. In order to study the influence of the delay unit optics on the coherence the experimental setup was first arranged in the configuration consisting of four symmetric Bragg crystals in the upper branch i.e. the Bragg-branch (see figure 3.9b). Although this configuration does not find application in XPCS, it can provide important information about coherence preservation of the delay unit with Bragg optics. In the next step the setup was gradually modified from the basic arrangement to the two-branch configuration, which included Laue beam splitters and more optical components in the beam path. It is important to note that the two-branch configuration will be utilized in the split-pulse XPCS experiments. Therefore the study of the coherence preservation of this configuration is the most important one.

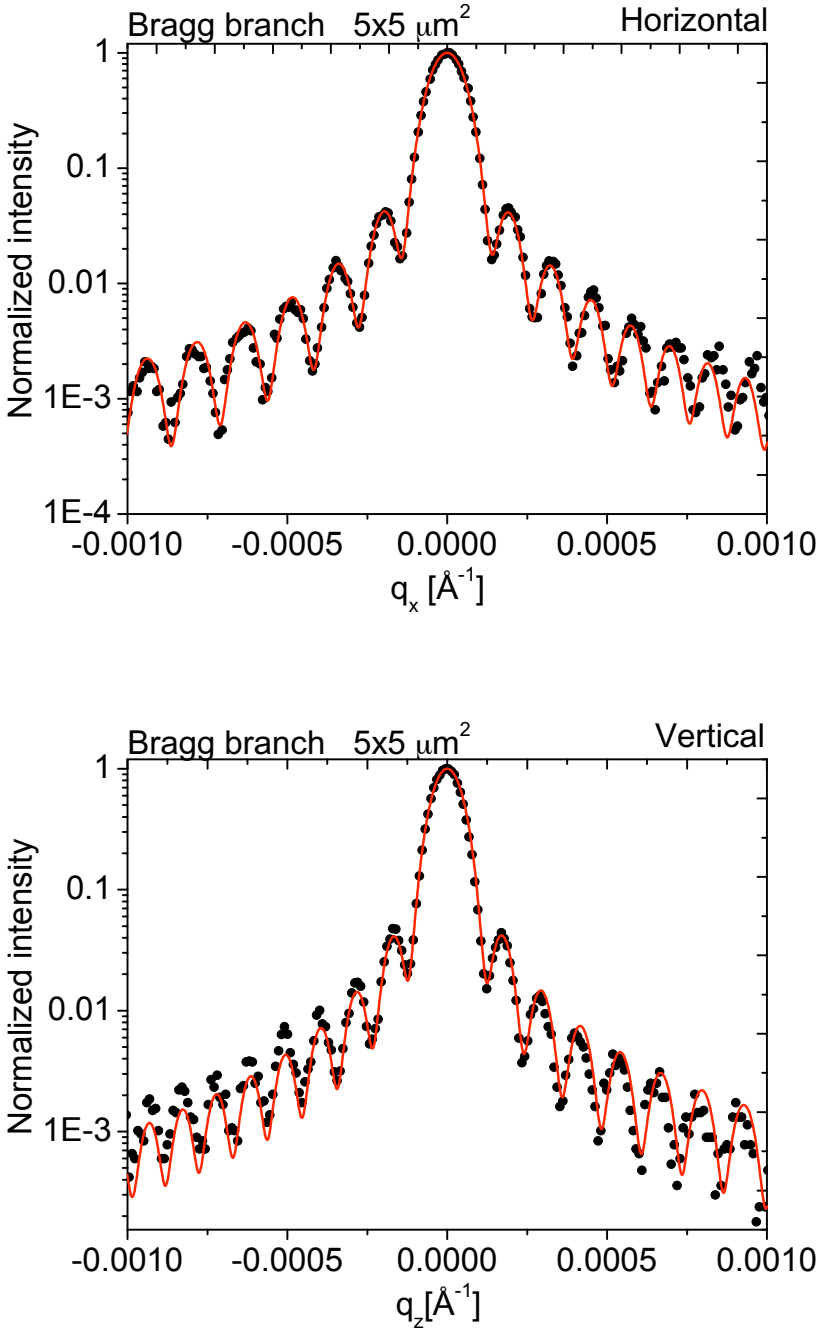

Figure 4.29: Fraunhofer diffraction pattern measured with 5 × 5 μm^2 rectangular aperture (black circles). Scans were made along the x and z directions. The red line is the calculated Fraunhofer pattern convoluted with a detector aperture of 25 μm.

Table 4.3: Parameters used for the calculation of the Fraunhofer pattern of figure 4.29 in vertical and horizontal geometry. Parameters S, h, Δq denote the slit size, asymmetry, detector resolution and the scattering vector spread. The parameter V denotes the visibility of the measured patterns.

S [μm]	h [mm]	R_{DET} [μm]	Δq [Å^{-1}]	V [%]	geometry
4.7	1.6	25	$3.3 \cdot 10^{-6}$	73	horizontal
5.5	1.5	25	$3.3 \cdot 10^{-6}$	74	vertical

4.3.2.3.1 Bragg branch configuration First Fraunhofer measurements were made with the delay unit arranged in the Bragg-branch configuration (see figure 4.1). The results are shown in figure 4.29. The obtained diffraction patterns were measured with the 5×5 μm^2 rollerblade slits. The data was normalized to the maximum intensity. The vertical and horizontal size of the slits was smaller than ξ_{th} and ξ_{tv}, respectively, and the resulting Fraunhofer patters reveals intensity oscillations with an amplitude that gradually diminishes with q. The visibility of fringes is of course reduced compared to the ideal case shown in figure 4.23. The red line in figure 4.29 shows the Fraunhofer pattern calculated using equation (4.15), convoluted with the resolution function of the detector and using parameters (including the negligible wave vector spread) given in table 4.3. The agreement is very good supporting the high performance of the used Bragg optics.

The widths of the Fraunhofer central maxima were slightly different in horizontal and vertical directions. This is due to the slightly different vertical and horizontal sizes of the collimating slits. The calculated vertical and horizontal Fraunhofer patterns indicates a slit size of 4.7 μm and 5.4 μm, respectively.

The visibility V of the measured Fraunhofer patterns was quantified using expression (4.14). The averaged value for the q range shown in the figure (namely in the $-10^{-3} < q < 10^{-3}$Å^{-1} range) yielded comparable values in horizontal ($V_H = 73\%$) and vertical ($V_V = 74\%$) directions. In order to quantify an essential change of visibility of the Fraunhofer patterns measured in different delay unit configurations, the same q range will be used in the further analysis.

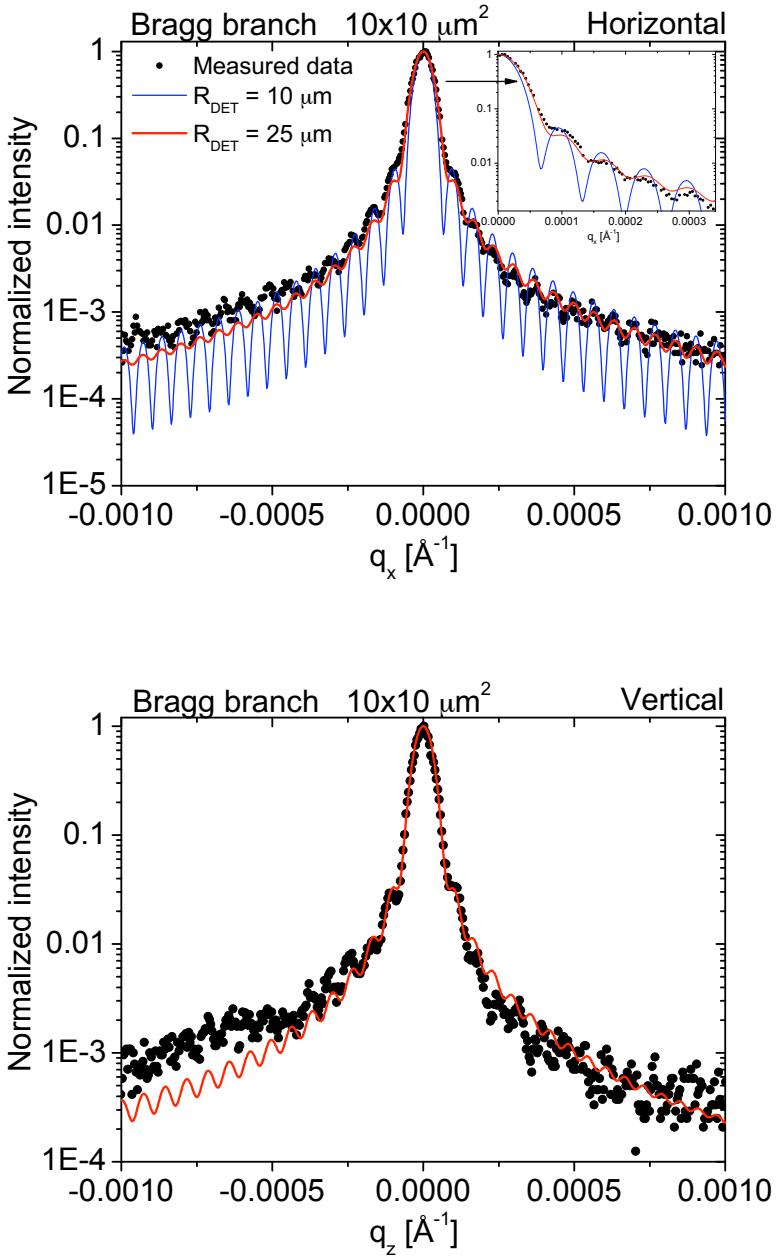

Figure 4.30: Fraunhofer diffraction patterns from 10 × 10 μm^2 rectangular aperture (black circles). The visibility of the fringes is considerably reduced from those from figure 4.29. The red solid line represents the Fraunhofer pattern convoluted with the 25 μm size of the detector aperture. The blue line of the upper plot shows is the calculated pattern for the detector resolution of 10 μm. The inset in the upper figure shows a zoom into the pattern.

Table 4.4: Parameters used in calculating the Fraunhofer pattern of figure 4.30. Parameters S, h, R_{DET}, Δq denote a size of an aperture, asymmetry, detector resolution, the scattering vector spread, respectively.

S [μm]	h [mm]	R_{DET} [μm]	Δq [Å^{-1}]	geometry
9.6	1	25	$3.3 \cdot 10^{-6}$	horizontal
9.6	2	25	$3.3 \cdot 10^{-6}$	vertical

Figure 4.30 shows Fraunhofer patterns produced using a 10×10 μm^2 collimating aperture. As expected from expression (4.12) the separation between the minima of the fringe pattern decreased due to the larger size of the slit opening. It is also observed that the oscillations of horizontal and vertical patterns are significantly washed out as compared to those of figure 4.29. The reason for the moderate quality of the patterns is the low resolution of the detector (i.e. too large aperture size of the detector slits). This interpretation is supported by the calculated Fraunhofer patter for detector slit size of 10 μm showing a much higher visibility, as indicated by the blue line of figure 4.30. The red line is the calculated pattern based on equation (4.12), including the detector resolution used during the experiment, namely 25 μm (see table 4.4). As expected the oscillations fade away quickly with a lower detector resolution. In addition there is evidence that parasitic slit scattering [43] reduces the visibility. The bump in the vertical profile is indicative of that.

4.3.2.3.2 Two-branch configuration of the delay unit In order to determine the coherence preservation properties of the delay unit in the split-pulse XPCS conditions the device was arranged in the two-branch configuration (see figure 2.5). To ensure that there is no interference between the beams of the two branches the delay time τ was set to 273 ps, which is much longer than the coherence time determined by the experimental conditions[17] (i.e $\tau_0 = 1.27$ ps).

[17]The value of τ_0 was obtained from equation (4.10) knowing that the longitudinal coherence length ξ_l during the experiment was 8.3 μm.

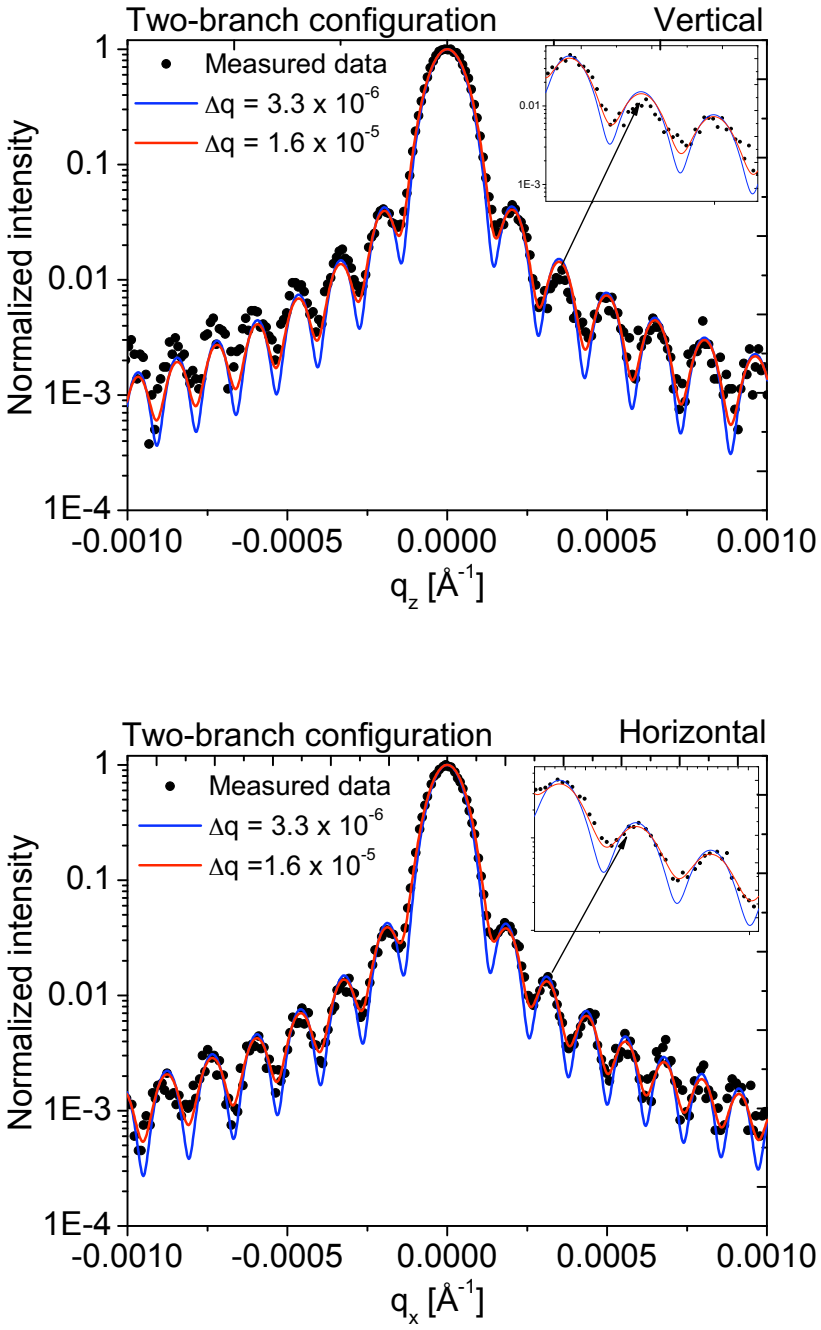

Figure 4.31: Fraunhofer diffraction pattern from the 5 x 5 μm^2 rectangular aperture (black circles) located behind the delay unit, which was operated in the two-branch configuration. The Fraunhofer diffraction pattern calculated for different Δq values are represented by the blue ($\Delta q = 1.6 \cdot 10^{-6}$Å^{-1}) and red ($\Delta q = 3.3 \cdot 10^{-5}$Å^{-1}) lines. The detector resolution (i.e 25 μm opening of the detector slit) was accounted for in the calculations.

Table 4.5: Parameters used for the calculation of the Fraunhofer pattern of figure 4.31 in vertical and horizontal geometries. S, h, R_s, R_{DET}, Δq denote the slit size, asymmetry, detector resolution, the scattering vector spread, respectively. The parameter V denotes the visibility of the measured patterns.

S [μm]	h [mm]	R_{DET} [μm]	Δq [Å^{-1}]	V[%]	geometry
4.9	1.6	25	$1.6 \cdot 10^{-5}$	62	horizontal
5.5	1.5	25	$1.6 \cdot 10^{-5}$	62	vertical

In order to achieve comparable experimental conditions to the Bragg-branch configuration the measurements were performed with 5 $\times$ 5 μm^2 size of the rollerblade slits and the detector resolution of 25 μm. The resulting Fraunhofer patterns are shown in figure 4.31. It should be noted that the figure shows only one Fraunhofer pattern in horizontal and vertical scattering planes, respectively, since the two beams downstream of the delay unit were superposed. The blue line shows the Fraunhofer diffraction pattern, which was calculated according to expression (4.12) and corrected for the detector resolution. Since the smearing of the fringes is stronger than predicted by the detector resolution alone, one might conclude that there is an additional[18] incoherent contribution to the scattering pattern, which leads to a reduction of the visibility. Using expression (4.15) together with the resolution function of the detector one can find a good match to the measured Fraunhofer patterns, as depicted in figure 4.31 by the red line. Table 4.5 lists the parameters used in the calculation. The fringe visibility was deduced from the measured patterns. The analysis based on expression (4.14) yielded $V_H = 62\%$ and $V_V = 62\%$ in horizontal and vertical planes, respectively. The reduction of the fringe visibility indicates a smaller transverse coherence length in both the vertical and horizontal plane.

[18] compared to the Bragg branch configuration

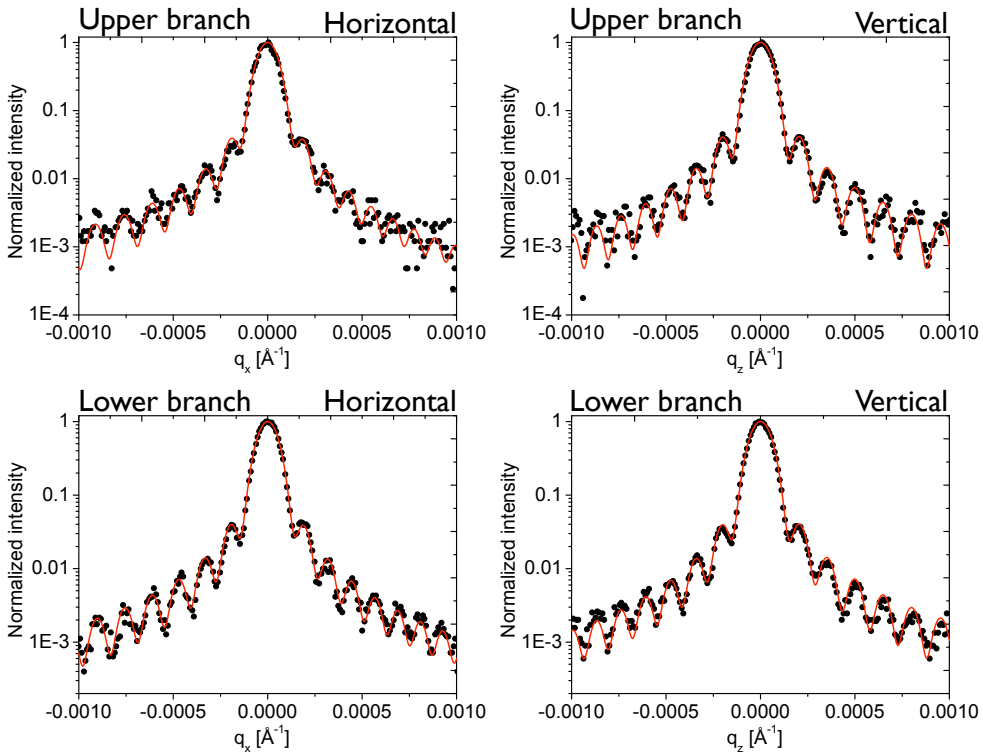

Figure 4.32: Fraunhofer diffraction pattern from 5 x 5 μm^2 rectangular aperture (black circles) located behind the delay unit, which was operated in the upper and lower branch configurations. Calculated Fraunhofer diffraction patterns are represented by a red solid line. The detector resolution (i.e 25 μm opening of the detector slits) was accounted for in the calculations.

4.3.2.3.3 Single branch configuration of the delay unit In order to get more insight in the origin of the reduction of the fringe visibility observed in the two-branch setup, the Fraunhofer measurements were performed separately for the upper and the lower branch of the delay unit. Figure 4.32 shows the resulting diffraction patterns.

Fraunhofer patterns were calculated for all measured data according to equation (4.15) and including the detector resolution. A relatively good match between the calculated and measured patterns was achieved. Tables 4.6 and 4.7 list the parameters used in the calculations. The visibilities of the corresponding measured patterns are listed in table 4.8.

Table 4.6: Parameters used for the calculation of the Fraunhofer pattern of figure 4.32 in vertical and horizontal geometries and the upper branch of delay unit. S, h, R_{DET}, Δq denote the slit size, asymmetry, detector resolution, the scattering vector spread, respectively.

S [μm]	h [mm]	R_{DET} [μm]	Δq [Å^{-1}]	geometry
4.9	1.2	25	$1.6 \cdot 10^{-5}$	horizontal
4.5	1.3	25	$2.7 \cdot 10^{-5}$	vertical

Table 4.7: Parameters used for the calculation of the Fraunhofer pattern of figure 4.32 in vertical and horizontal geometries and the lower branch of delay unit. Parameters S, h, R_{DET}, Δq denote the slit size, asymmetry, detector resolution, the scattering vector spread, respectively.

S [μm]	h [mm]	R_{DET} [μm]	Δq [Å^{-1}]	geometry
4.8	1.3	25	$1.6 \cdot 10^{-5}$	horizontal
4.5	1.1	25	$1.6 \cdot 10^{-5}$	vertical

Table 4.8: The values of visibility V obtained from calculations of Fraunhofer pattern measured in the horizontal and vertical geometry with the delay line operated in various crystal arrangement.

	Bragg Branch	Upper Branch	Lower Branch	Two-Branches
V_h	0.73	0.55	0.62	0.62
V_v	0.74	0.69	0.63	0.62

The visibilities of the upper branch are slightly higher ($V = 0.69$) than the visibilities of the two-branch configuration. This result can be explained by the fact that the upper-branch consists of less optical elements than the two-branch configuration. As discussed in section 4.3.2.1 any imperfection of an optical com-

ponent can lead to an increase of the effective source size, which may lower the transverse coherence length. Having more optical components in the path might thus eventually increase the effective source size.

The results measured in the upper-branch configuration are however not consistent. One notes different values for the visibility in the horizontal ($V_H = 0.55$) and vertical ($V_V = 0.69$) geometries. The visibility $V_H = 0.55$ for the upper branch is not compatible with the value for the two-branch configuration. This result is not understood. However the data were taken during independent measurements and the result points to improper alignment in the upper branch measurement. Further measurements are required to investigate the visibility values obtained with the upper and lower branch of delay unit. For instance the Fraunhofer measurement of a single Laue beam splitter would reveal the influence of the crystal on the coherence properties of the beam.

The results of the Fraunhofer measurements can be summarized as follows. For the 5×5 μm^2 collimating slit size and the delay unit configuration consisting of 4 symmetric Bragg crystals one finds that the Fraunhofer pattern is perfectly described by the theoretical expression and taking the resolution of the detector into account. The obtained visibility is 73-74%. Increasing the collimating slit size to 10×10 μm^2 significantly reduces the visibility of the fringes. This can be explained as a resolution effect; the applied detector resolution in the experiment was too low. The Fraunhofer diffraction pattern produced by the 5×5 μm^2 aperture and the delay unit arranged in the two-branch configuration including two Laue crystals show a 11% to 12% decrease of the fringe visibility compared to the Bragg-branch arrangement in the horizontal and vertical planes, respectively. Based on the present data one cannot decide whether or not this is caused by imperfections of the Laue optics or is just an effect caused by the doubling of the number of optical elements.

4.3.3 Statistical analysis of a speckle pattern

4.3.3.1 Introduction

The coherence properties of the beam can be estimated by the Fraunhofer measurements, as shown in the previous section. It can be also quantitatively determined by a statistical analysis of a static speckle pattern [51, 52]. When a disordered sample is illuminated coherently one can observe a grainy interference pattern in the detection plane commonly called a 'speckle' pattern. When the sample is static the speckle pattern will not change in time. A statistical analysis of such a speckle pattern can provide a quantitative information on the degree of coherence or the contrast. This knowledge is important prior to performing XPCS measurements [12].

Coherent illumination of a sample implies the usage of an X-ray beam with sufficient transverse and longitudinal coherence lengths. More specifically, the illuminated area of the sample must be smaller than the coherence area, determined by the product of $\xi_{th} \times \xi_{tv}$. In addition, the maximum path length difference PLD in the sample has to be smaller or comparable to the longitudinal coherence length, requiring in transmission geometry that [44]

$$PLD \approx 2W \cdot \sin^2\theta + S \cdot \sin 2\theta \leqslant \xi_l \tag{4.17}$$

where W is the sample thickness, S is the size of the beam and 2θ is the scattering angle. Equation (4.17) sets the limit of the maximum q vector accessible in the experiment.

The Fraunhofer measurements shown in the previous section proved that the delay unit is capable of transmitting a coherent beam. All these measurements involved very small scattering vectors, i.e. $q < 1 \cdot 10^{-3}$ Å^{-1}. In order to quantify the degree of coherence at larger scattering vectors, static speckle patterns were measured with the delay unit arranged initially in the two-branch configuration. Further measurements were performed separately for the upper and lower branch of the delay unit.

An advantage of the static speckle measurement is that the same experimental configuration as for XPCS measurements is used. Therefore the information about the delay unit performance under split-pulse XPCS conditions is obtained.

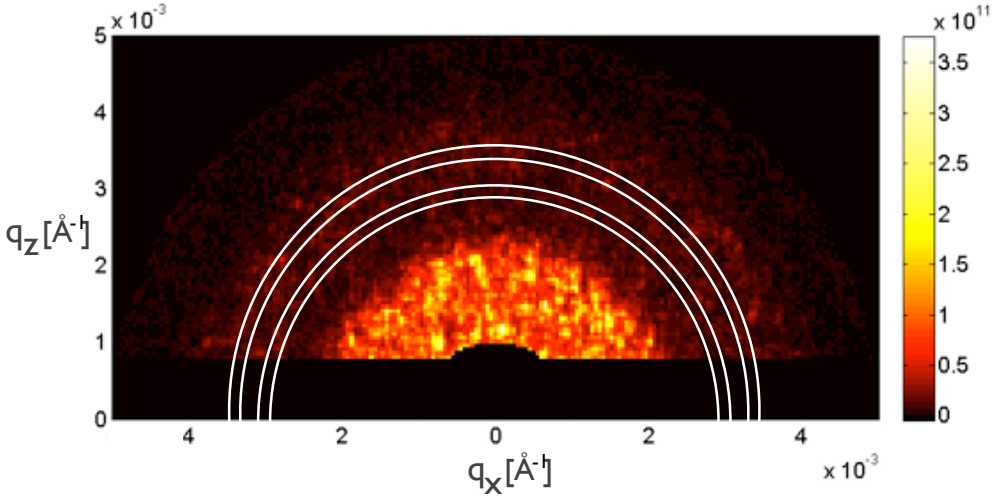

Figure 4.33: Speckle pattern of a silica powder recorded with a direct illumination CCD camera. The range of scattering vectors used in the analysis is depicted by the interior of two semicircles. The selected areas corresponds to the 0.0029 $Å^{-1}$ < q < 0.0031$Å^{-1}$ and 0.0034 $Å^{-1}$ < q < 0.0036$Å^{-1}$, respectively.

4.3.3.1.1 Two-branch configuration of the delay unit Figure 4.33 shows the diffraction pattern recorded with the delay unit arranged in the two-branch configuration. The sample was illuminated with a beam size of 9 × 9 μm^2 defined by a pair of roller blade slits [43] placed downstream the delay line. Since the nominal vertical and horizontal transverse coherence length is larger at this position, the aperture selects a coherent portion of the incident radiation. The sample was mounted 155 mm downstream of the aperture. In order to transmit only the central Fraunhofer peak, a guard slit was placed just before the sample position (cf. section 3.5.4). The coherent flux achieved in this configuration at the sample position was 2.26 $\times 10^4$ photons/s at 34 mA ring current. This value is more than 4 orders of magnitude lower than typically reported for experiments dedicated to statistical speckle analysis [51, 52]. The image shown in figure 4.33 was obtained

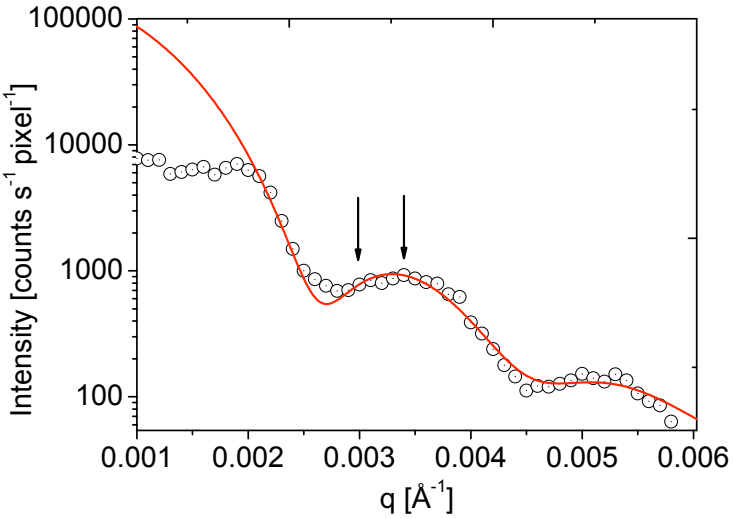

Figure 4.34: Angularly averaged small angle scattering pattern of silica powder shown in figure 4.33

by summing 200×15 s exposures. The electronic noise of the CCD was accounted for in the analysis by measuring a series of 15 s dark images without X-ray beam and its average was subtracted from each frame before summation.

The coherently illuminated sample was a silica (SiO_2) powder [55]. The small angle scattering signal recorded from the sample (see figure 4.33) was averaged over annuli of constant q. The result is shown in figure 4.34. The intensity of the averaged signal falls off rapidly with increasing q but shows modulations as expected for a sample of monodisperse spherical particles. The fit of the small angle scattering profile with a model utilizing the form factor of spherical particles convoluted with the Schulz size distribution function [56] is also shown in figure 4.34. The quality of the fit is reasonable and yields an average radius R = 1666 Å.

Due to the particular shape of the guard slit (cf. section 3.5.4) the parasitic slit scattering cannot be completely eliminated yielding a distortion of the speckle pattern at very small q vectors. At large q values the speckle pattern is more affected by the subtraction of the electronic noise of the CCD camera. Hence, the

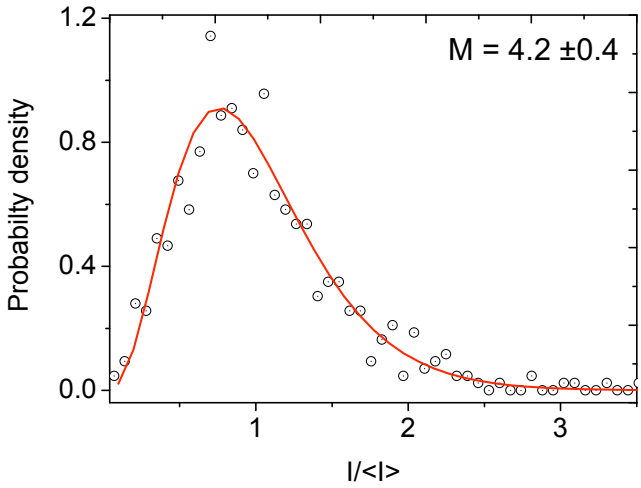

Figure 4.35: Probability density function of the speckle with an intensity recorded at q centered at 0.003 $Å^{-1}$. X-ray beam was passing two branches of the delay unit and the slit size of 9×9 μm^2.

analysis of the speckle pattern was carried out at intermediate q values, depicted by arrows in figure 4.34. It is important to note that for highly monochromatized X-ray radiation the expected q dependence of the contrast is very week [51].

Figure 4.35 shows the probability density function of the speckle pattern displayed in figure 4.33. The intensities in the q ring from 0.0029 $Å^{-1}$ to 0.0031 $Å^{-1}$ were selected and normalized to the mean intensity <I>. The probability function, $p(I)$, was obtained by histogramming the selected intensities. The obtained histogram shows a wide distribution of intensities. The variations of intensities are larger than expected for Poisson statistics. This is a characteristic feature of speckle.

For fully coherent illumination it can be shown that a speckle pattern should follow a negative exponential function [53]:

$$p(I) = (1/ < I >) \exp(-I/ < I >) \tag{4.18}$$

For partially coherent illumination the intensity distribution of a speckle pattern can be defined by [53]:

$$p(I) = (\frac{M}{< I >})^M I^{M-1} \frac{\exp{(-M \times I/ < I >)}}{\Gamma(M)} \tag{4.19}$$

where Γ is a gamma function . The contrast β of a speckle pattern is related to M according to $\beta = 1/M$ [51]. Figure 4.36 shows the probability distribution function plotted for different M values. For M = 1 the equation (4.19) simplifies to a form of equation (4.18) and reflects the intensity distribution of the fully coherent beam with $\beta = 1$.

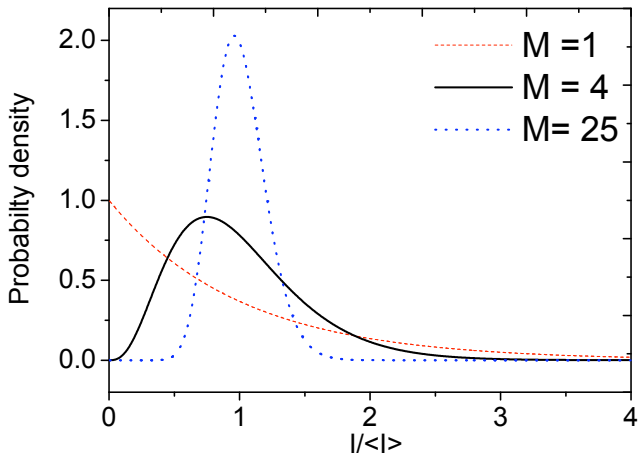

Figure 4.36: The probability density function of photons emited from fully coherent (M=1) source. The effect of partially coherent illumination is demonstrated by plots with M=4 and M=25.

The solid line in figure 4.35 shows a fit of equation (4.19) to the experimental data centered at the q value of $3 \cdot 10^{-3}$Å^{-1}. The fit procedure yields M = 4.2±0.4 which corresponds to the contrast β=0.23 ± 0.02. The same statistical analysis was applied to the q annulus centered at $q = 3.5 \cdot 10^{-3}$Å^{-1}. A comparable value for the contrast β=0.26 ± 0.02 is found. Figure 4.37 shows the resulting histogram and the corresponding fit.

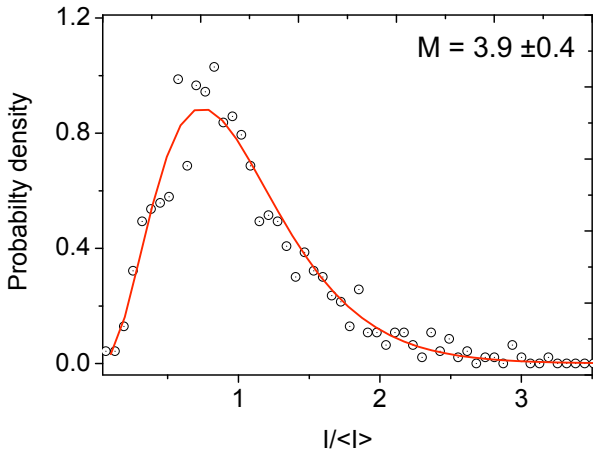

Figure 4.37: Probability density function of the speckle pattern intensity at $q = 3.5 \cdot 10^{-3}$Å^{-1} recorded with X-ray beam passing two branches of the delay unit and the 9×9 μm^2 slit size.

Whether or not the collimating aperture influences the contrast was investigated by closing the collimating aperture 5×5 μm^2. Figure 4.38 shows the probability distribution function of a speckle pattern produced with a 5×5 μm^2 aperture. The corresponding speckle pattern is shown in figure 4.40a. In this configuration the flux was 6.96×10^3 photons/s at 34 mA ring current. The contrast values obtained at $q = 3 \cdot 10^{-3}$Å^{-1} and $q = 3.5 \cdot 10^{-3}$Å^{-1} are $\beta = 0.23 \pm 0.03$ $\beta = 0.17 \pm 0.02$, respectively. It is suspected that the low contrast value at $q = 3.5 \cdot 10^{-3}$ Å^{-1} might be due to lower statistics of the measured speckle patterns with the 5 x 5 μm^2 aperture. This is because at low count rates and high scattering vectors, the removal of the detectors dark current might affect the static speckle analysis.

4.3.3.1.2 Single-branch arrangement of the delay unit The same statistical analysis was applied to the speckle pattern recorded with 9×9 μm^2 slit size but only one branch of the delay unit. This yields a slightly higher value for the contrast. Figures 4.39a and 4.39b shows probability distribution functions

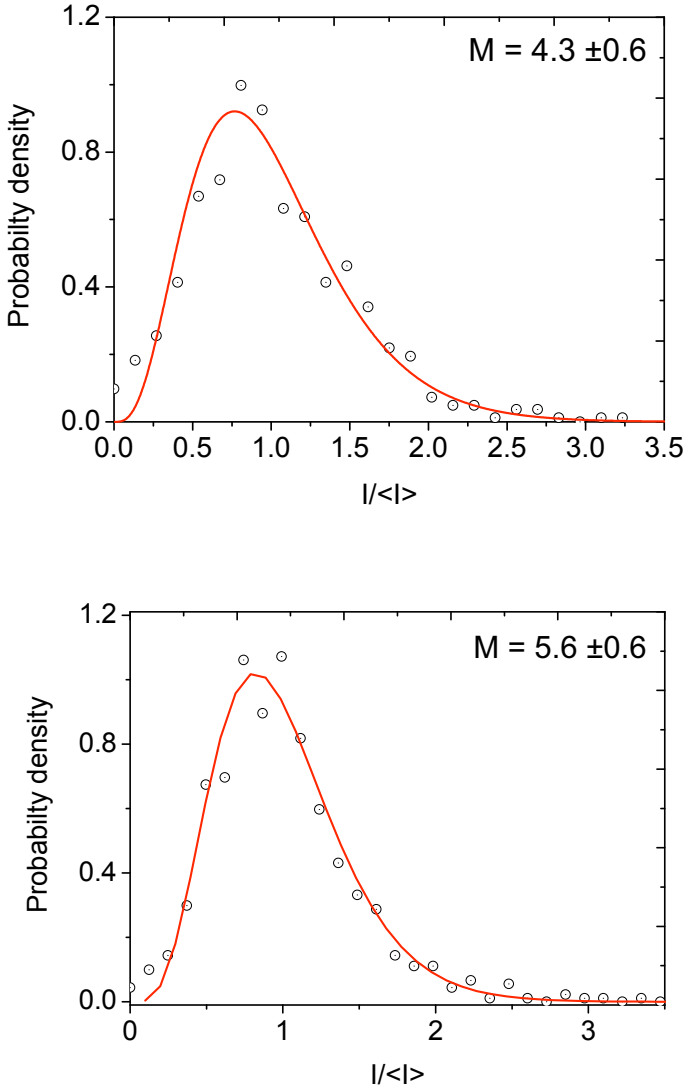

Figure 4.38: The probability density function of the speckle pattern intensity recorded with X-ray beam passing the two branches of the delay unit and 5×5 μm^2 aperture size. The upper and lower figures corresponds to the static speckle pattern analysis at $q = 3 \cdot 10^{-3}$Å^{-1} and $q = 3.5 \cdot 10^{-3}$Å^{-1}, respectively.

Table 4.9: Values of contrast β obtained from statistical analysis of measured speckle patterns at $q = 0.003\text{Å}^{-1}$ and $q = 0.0035\text{Å}^{-1}$, respectively. The delay unit was arranged in the two-branch, upper-branch and lower-branch configurations. Various slits setting were utilized in the measurements.

	Slit configuration [$\mu m \times \mu m$]			
	9×9	5×5	9×9 (upper)	9×9 (lower)
$\beta(q = 0.0030\text{Å}^{-1})$	0.23(2)	0.23(3)	0.26(1)	0.29(4)
$\beta(q = 0.0035\text{Å}^{-1})$	0.26(2)	0.17(2)	-	-

obtained in these experimental configuration, where the X-ray beam was passing either through the upper or lower branch. The corresponding speckle patterns recorded by the area detector are shown in figure 4.40b and 4.40c. The contrast obtained from the fit procedure is $\beta = 0.26 \pm 0.01$ and $\beta = 0.29 \pm 0.04$ for the upper and lower brach of the delay unit, respectively. The results are summarized in table 4.9. The results seem to indicate that a lower number of optical elements (single branch configuration) yields a slightly higher contrast value.

4.3.4 Summary

The coherence properties of undulator radiation from the Troika beamline of ESRF transmitted through various optical configurations of the delay unit were characterized in two independent experiments. The measured Fraunhofer diffraction show a very good agreement with the calculated patterns. The visibility of Fraunhofer fringes using a 5×5 μm^2 aperture size and the Bragg-crystal branch configuration is 73%[19]. The visibility in the two-branch configuration (employing Laue crystals) was measured separately for the upper and lower branch. The visibility is reduced by 11-12%.

A statistical analysis[20] of static speckle patterns from a silica powder sample yield result for the degree of coherence for large q values. A contrast of 26% and

[19] note that in part of the literature $V = \sqrt{\beta}$ is used

[20] note that the statistical analysis of the speckle pattern yields information not only on the coherence properties of the incident beam but on the complete experimental setup (i.e. sample and optics)

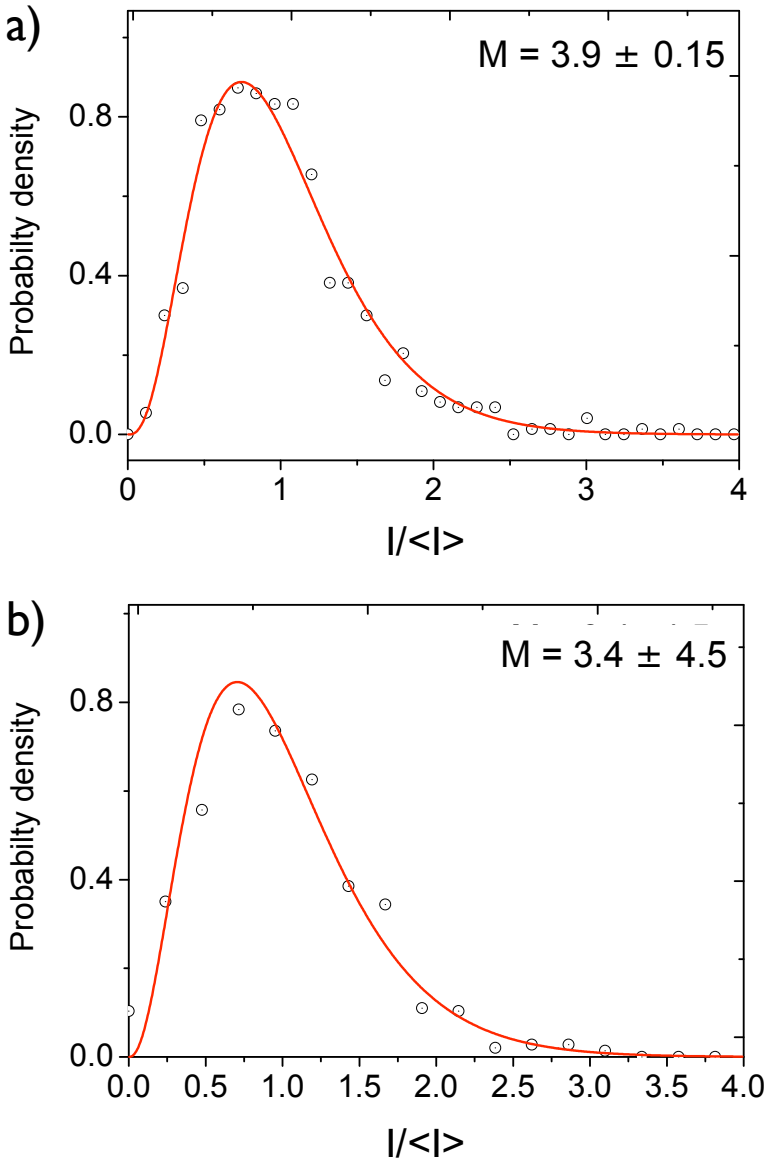

Figure 4.39: Probability density function of the speckle pattern intensity recorded with the X-ray beam passing either through the a) upper or b) lower branch crystals of the delay unit. A 9×9 μm^2 aperture was used. The analysis was performed at $q = 3 \cdot 10^{-3}$Å^{-1}.

29% is found for the upper and lower branch configuration. A reduction of the contrast β to 23% was found in the two-branch configuration.

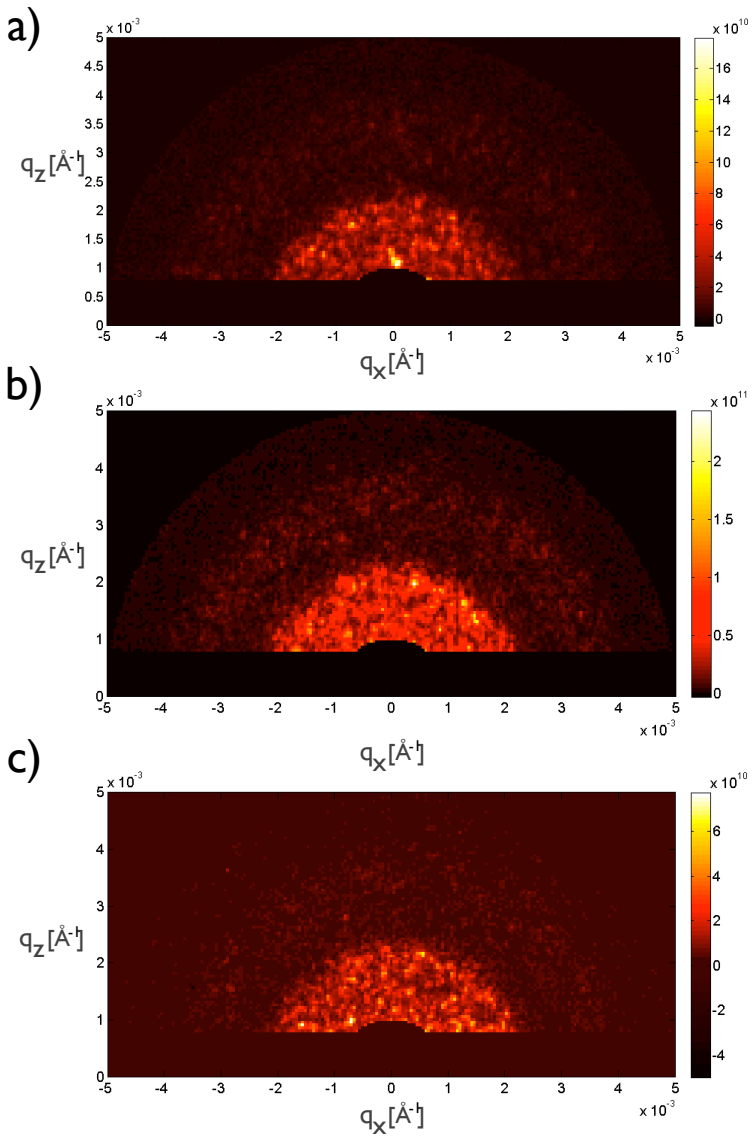

Figure 4.40: Speckle pattern recorded with various openings of the beam defining slit and configurations of the delay unit. a) 5 × 5 μm^2 slit opening and two-branch configuration. b) 9 × 9 μm^2 slit opening upper-branch configuration c) 9 × 9 μm^2 slit opening and lower-branch configuration.

Chapter 5

Outlook

The described device is the first delay unit working with hard (8.39 keV - 12.4 keV) X-rays. An application of the delay line to a wider range of experiments requires its further development. Possible upgrades of the delay unit are discussed in this chapter. Improvements of the existing 90 degree scattering scheme concern mainly crystal optics, diagnostics, and mechanical components. An extension to longer delay times and a wider range of wavelengths imposes modification of the scattering geometry and the development of alternative delay schemes.

Crystal optics

The throughput of the described two-branch delay unit was found to be very close to the theoretically expected value (cf. section 4.1.4), based on the high quality of the optical components. The throughput of the system can be further increased by replacing the Laue beam splitters with very thin Bragg crystals, as discussed in section 2.4.1.4. The replacement of the optics would result not only in a higher throughput but would also allow to recombine the two exit beams downstream of the delay unit, as discussed in section 2.4.1.6.

Mechanics

The key component of the delay unit is the central linear translation stage (cf. section 3.2.1). The movement of the translation stage is based on conventional friction based bearing technology. The performance tests of the translation made with the autocollimator yielded a yaw of 10 μrad, which is sufficient for performing delay time experiments with the Si(511) Bragg crystals at 8.39 keV, without severe implications on the crystal realignment procedure. Using a higher index reflection than 511 would put higher demands on the central translation unit. New high resolution approaches, based on air-bearing technology [57], are currently under development. The off axis deviations of the main translation (like yaw and pitch) could be significantly reduced, by using air-bearing technology, allowing probably a continuous change of the delay time with higher order reflections (e.q. 553) without additional crystal alignment.

Diagnostics

The results of the delay time measurements (cf. section 4.2.3) indicated that the precision is mainly limited by the time resolution of the detection system. A streak camera with sub picosecond resolution could be considered as an essential improvement of the diagnostic system.

Performing pump-probe and correlation spectroscopy with the delay unit re-

quires precise knowledge of the applied delay time. In the current setup the detector, dedicated for the timing measurement, is located in the beam path between the delay unit and the sample. In this configuration the delay time measurement and the experiment cannot be conducted simultaneously. If the beams of the upper and lower branches fulfill the Bragg condition at the position SP2, two pairs of pulses with the same time delay should exit the crystal SP2.

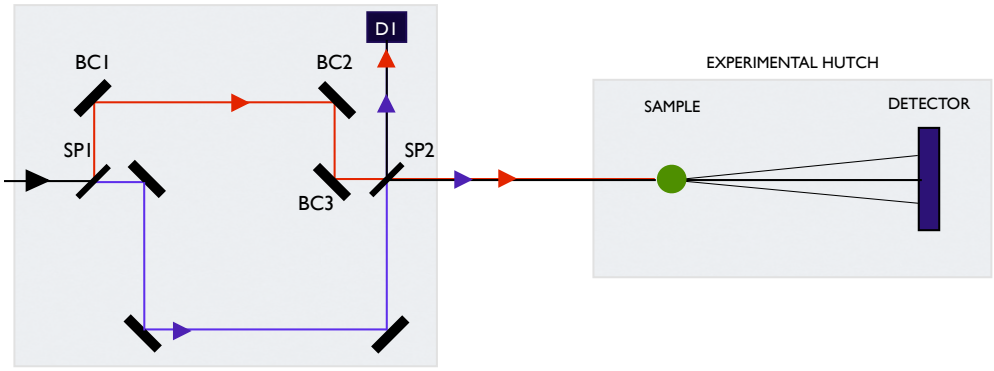

Figure 5.1: Diagnostics for the experiments with the delay unit. SP1 and SP2 are thin crystals oriented in Bragg geometry. The fast detector located at D1 position measures the pulse separation during the pump probe or XPCS experiments.

Housing

The delay time experiments were performed at room temperature under ambient conditions. The X-ray path inside the delay unit in the two - branch configuration is 2.180 m. Due to absorption of X-ray beam in air the throughput of the delay unit is considerably affected. At 8.39 keV 89% of the incoming X-ray beam is absorbed. Enclosing the experimental setup in a He environment should decrease the absorption losses to about 1% and make the intensity ratio of the beams of the upper and lower branches less dependent on the applied delay time[1]. The high thermal conductivity of He should also improve the temperature stabilization of the delay unit, which has an impact not only on the performance of the crystal

[1]With the change of the delay time the path lengths of the delay unit branches change and consequently the absorption loses are influenced as well.

optics (i.e the position and intensity) but also on the delay time. Due to the thermal expansion of the aluminum plate, which holds the crystals, a drift in temperature of 1 K will result in a 100 fs change of the delay time (in the two-branch configuration).

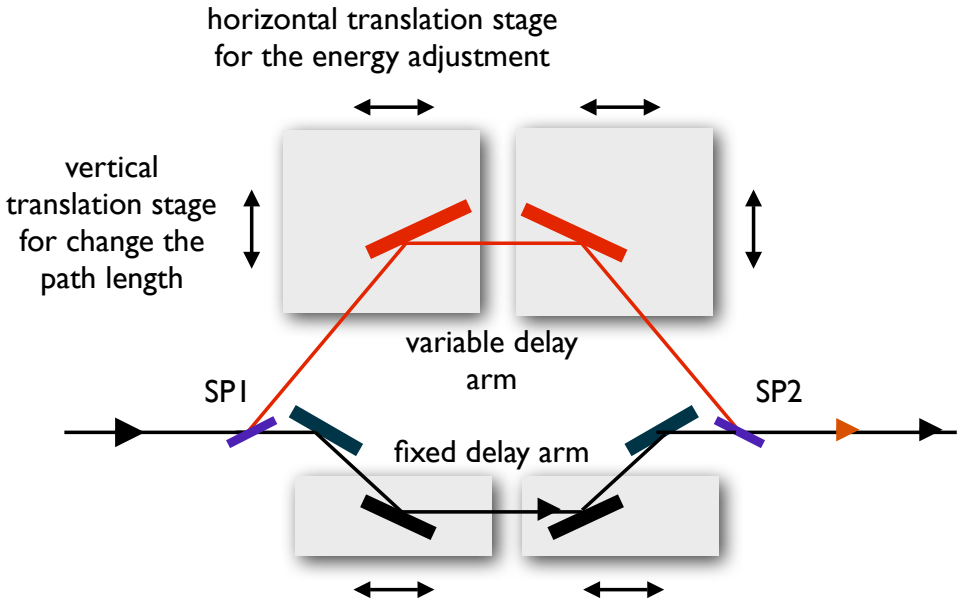

Figure 5.2: Delay line scheme for variable incident energy. The X-ray beam is split by a very thin Bragg crystal SP1 and travels two unequal paths defined by Bragg crystals mounted on delay arms. Various delay times are achieved by translating one of the two delay arms in the scattering plane. Both beams are recombined on the original path by the beam mixer SP2.

Alternative delay schemes

Due to the fixed angle geometry the energy of the delay unit can only be varied in discrete steps. Extending the application of the delay unit to a wider range of experiments imposes a modification of the current design. Alternative delay schemes [1, 16] employ scattering geometries at Bragg angles other from 45°. However, a change of the time delay is more complicated then in the current design and requires more than one translation stage, unless the size of the reflecting crystals is large. Figure 5.2 shows a proposed scheme for a X-ray delay line

working with a wider wavelength range. The X-ray beam is split by a very thin Bragg crystal SP1. The pulse delay is achieved by translating only one delay arm. Both pulses are recombined by the beam mixer SP2. The two arms of the delay unit are equipped with separate horizontal translation stages to account for the change of energy. The lower arm is fixed, producing only a very small delay time. The Bragg crystals in the upper arm have a large surface to account for the change of the delay path. A simple geometrical consideration of this effect for the Si(511) reflection is shown in figure 5.3.

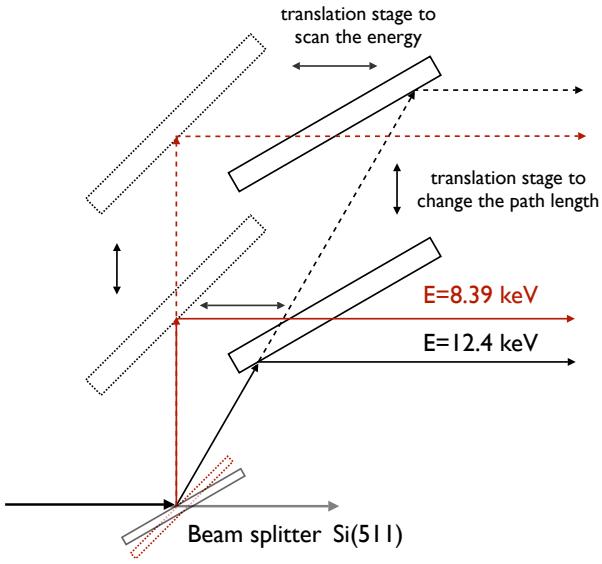

Figure 5.3: Simple geometrical consideration for the change of energy and delay time

The maximum path length depends on the crystal reflection and the applied energy. The main difficulty of this scheme will be to produce sufficiently long perfect crystals with low enough slope errors. An alternative solution is a combined translation of the crystals horizontally and vertically in the scattering plane for a change of the delay time.

Chapter 6

Summary and conclusions

This work reports on a novel design and successful implementation of a delay unit dedicated for fast time domain XRD and pump-probe type studies. The scheme of the delay unit is based on perfect crystal optics used in 90° scattering geometry. The device employs up to eight perfect silicon crystals that split a single X-ray pulse into two sub-pulses. The two pulses propagate through two branches with different path lengths before they are recombined in the beam mixer. The beam splitting and mixing is accomplished by Laue crystals and the X-ray path inside the delay unit is defined by Bragg crystals. Using Laue and Bragg optics in the same setup does not allow for a perfect recombination of both split pulses on the same path, unless the crystal alignment procedure involves also tilting of the crystals. Due to the fixed scattering angle geometry the design provides only limited energy tunability, namely 8.39 keV and 12.4 keV using different crystals Si(511) and Si(553).

The technical realization of the delay unit concept required 40 motorized stages for alignment and diagnostics purposes. An excellent performance of the translation unit was verified first by optical metrology, showing a yaw not larger than 11 μrad.

The optical performance of the Bragg reflecting and Laue splitting crystals has been tested at DORIS III, PETRA II and ESRF. The quality of the Si(511) and Si(553) crystals was verified by rocking curve measurements at 8.39 keV

and 12.4 keV, respectively. The results were very close to the theoretical values, showing the high quality of silicon crystals. The performance of the X-ray beam splitter was also verified at the aforementioned energies. Splitting ratios from 1:1 to 1:3 were achieved. A throughput of $T_M = 0.6\%$ is achievable at 8.39 keV with a Si(333) pre-monochromator under ambient conditions. This value is in very good agreement with the theoretically expected value. The setup shows good stability allowing for 30 min operation without the necessity of crystal realignment. No temperature stabilization nor active feedback was implemented yet in the system.

Time delay measurements were performed at 8.39 keV and 12.4 keV. Delay times up to 2.95 ns and 2.62 ns have been achieved with the one-branch and two-branch configuration, respectively. A time resolution of 15.4 ps was achieved in the measurements. This value is mainly determined by the time resolution of the detection system. Higher time resolution should be achievable by using a streak camera.

The influence of the optical elements on the coherence properties of an undulator beam was investigated by means of Fraunhofer diffraction and static speckle analysis. A high fringe visibility and a contrast of 23% were measured in the two-branch configuration. This indicates that coherence experiments with the delay unit will be feasible.

The results obtained with synchrotron radiation indicate that the device is ready for further diagnostic tests and experiments with XFEL radiation.

Appendix A

Appendix

A.1 Acronyms

ADC	Analog to Digital Converter
APD	Avalanche PhotoDiode
BC	Bragg Crystal
CFD	Constant Fraction Discriminator
ESRF	European Synchrotron Radiation Facility
LCLS	Linac Coherent Light Source
MCA	Multi Channel Analyzer
IC	Ionization Chamber
SASE	Self amplified spontaneous emission
TAC	Time to Amplitude Converter
XFEL	X-ray Free Electron Laser
XPCS	X-ray Photon Correlation Spectroscopy
XRD	X-ray Diffraction

A.2 Performance of the delay unit optics at a bending magnet

Measurements of Si(511) rocking curves were performed at the bending magnet beamline C, DORIS III. The layout of the beamline was shown in figure 3.5.1. Data were collected in vertical scattering geometry with the vertical and horizontal exit slit openings of 1×2 mm^2, located 28.8 m from the source. Additional collimation of the X-ray beam was provided by the primary slits set to 1×3 mm^2 in vertical and horizontal directions, respectively. The reflected intensity from each crystal was normalized to the incident intensity, which was monitored by ionization chambers. In this way any intensity variations coming from instabilities of the beamline monochromator were corrected. The measured rocking curves were corrected for absorption losses.

Figure A.1 shows rocking curve measurements of the delay unit Bragg crystals. The red solid line is the result of a fit using a gaussian to the experimental data. The FWHM of the fit is given in each figure. The calculated rocking curve is depicted by the blue dashed lines. The inset shows the schematic setup. Figure A.1a shows the reflection curve of the Si(511) crystal at the position BC1. The expected width ω of the rocking curve is a convolution of the Si(511) Darwin curve ω_0 and the angular spread Ω of the incident radiation from the Si(111) beamline monochromator, i.e.

$$\omega = \sqrt{\Omega^2 + \omega_0^2} \tag{A.1}$$

The red solid line in figure A.1a is the result of a fit of a gaussian to the measured data. The FWHM of 108 μrad obtained from the fit is comparable to the nominal value of the beam divergence at beamline C, i.e. about 120 μrad.

Since at position BC1 the rocking curve width is dominated by Ω, information about the quality of the Si(511) crystal cannot be deduced. This is different for the position BC2. Rocking the crystal BC2 allows one to determine the quality of crystals BC1 and BC2. Following the discussion given in section 4.1.1, the

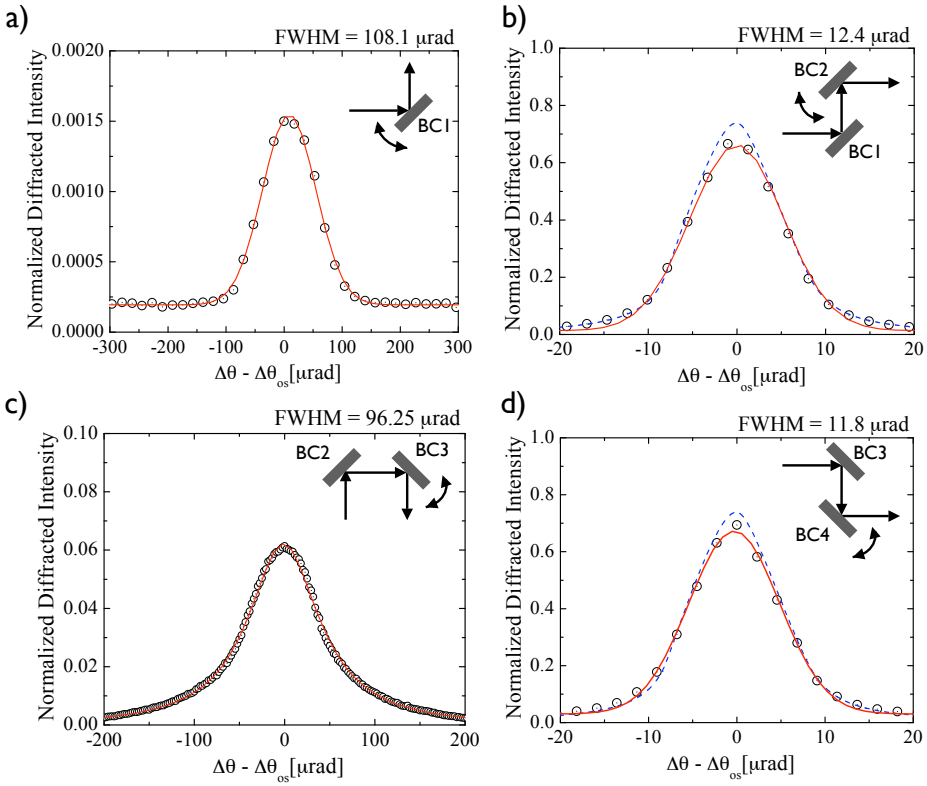

Figure A.1: Measured reflectivity of Si(511) in symmetric Bragg geometry at E = 8.39 keV. BC1, BC2, BC3, and BC4 denote the positions of the Bragg crystals depicted in figure 3.9b. The red solid line in figures a) b) and d) shows Gaussian fits to the experimental data. The calculated rocking curves are represented by dashed blue lines. In figure c) the red line is the result of a Lorenzian curve fit. The inset of each figure shows the corresponding crystal arrangement.

expected double-crystal rocking curve is the convolution of two Si(511) Darwin curves yielding the peak reflectivity of 0.73 and a width of 12.2 μrad. Figure A.1b shows the measured profile of the Si(511) at the BC2 position. Theory and measured values agree to within the estimated error of a few %. A relative discrepancy D between width of the calculated ω_{CALC} and measured $\omega_{\mathrm{MEASURE}}$ rocking curves, calculated following

$$D = \frac{|\omega_{\mathrm{CALC}} - \omega_{\mathrm{MEASURE}}|}{\omega_{\mathrm{CALC}}} \tag{A.2}$$

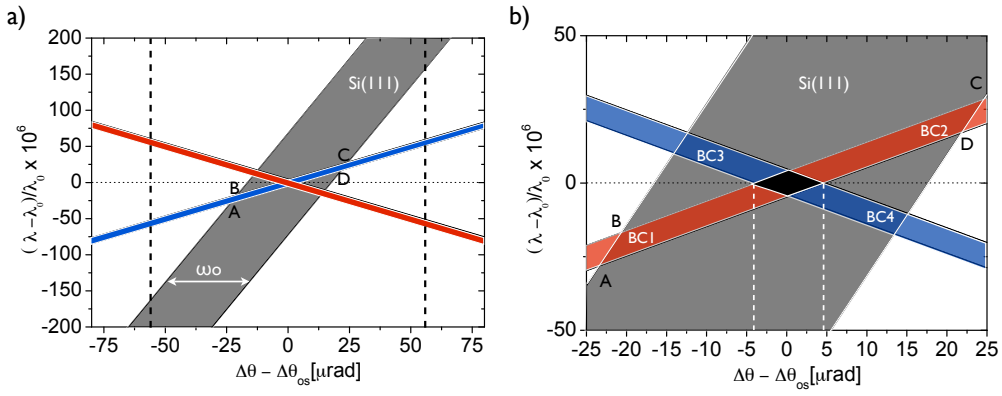

Figure A.2: a) DuMond diagram of the Si(511) Bragg crystals arrangement sketched in figure 3.9b. The dashed lines correspond to the incident vertical beam divergence at the beamline C, Ω =120 μrad. b) The dispersive configuration of the BC2 and BC3 crystals. The resolution element of the setup is depicted by the black area. The dashed line correspond to the exit beam divergence.

is 1.6%. This measurement confirms the good quality of the Bragg crystals.

The rocking curve measured at position BC3 is shown in figure A.2c. The FWHM obtained from the fit of the peak profile is 96.25 μrad, which is considerably larger than the Si(511) Darwin width. Since the BC1 and BC2 crystals are arranged in a non-dispersive (+n,-n) configuration, all X-rays enclosed by parallelogram ABCD, in figure A.2a, are transmitted and collected when rocking the crystal BC3. Note that BC2-BC3 arrangement is dispersive (+n,+n). The exit angular divergence and energy spread in this configuration are thus defined by the cross section of BC2 and BC3 reflection bands, depicted in the DuMond diagram in figure A.2b. The energy resolution and angular divergence in this case are limited only by the intrinsic width of the crystal reflection. When the BC3 crystal is rocked, the small 'black' area moves along the BC2 reflection band. In this case the BC3 crystal acts like an analyzer to the radiation reflected by BC2. From figure A.2b it can be seen that the expected width is about 50 μrad. This is considerably smaller than the measured (96.25 μrad) width. This discrepancy might arise from a situation when a beam illuminates a crystal area of higher

Table A.1: Reflectivity of Bragg optics measured at a bending magnet source. Measured reflectivities were corrected for X-ray absorption in air. The values in the brackets represent calculated crystal reflectivities based on DuMond diagram shown in figure A.2

MONO	BC1/MONO	BC2/BC1	BC3/BC2	BC4/BC3
Si(111)	0.0015(0.021)	0.67(0.73)	0.061(0.09)	0.69(0.73)

mosaicity[1].

The good match between the measured and calculated diffraction profiles is also found at the BC4 position. The discrepancy D is 3.5%, indicating a good quality of the Si crystal. Figure A.1d shows the corresponding results.

The calculation of the crystal reflectivities is based on the DuMond diagram, shown in figure A.2. The diagram was generated by the Matlab code, which calculates the area of each transmission window given by the cross section of two reflection bands in the DuMond diagram. According to DuMond [34] the transmitted intensity is proportional to the transmission window area. The throughput of two-crystal arrangement is found from the ratio of calculated areas multiplied by the crystal reflectivity. Table A.1 shows the calculated reflectivities of the delay unit crystals. Since the crystals BC1-BC2 and BC3-BC4 arrangement are non-dispersive the reflectivity is not affected by the incident beam divergence. The reflectivity of the BC1 is strongly affected by the properties of the incident beam. The divergence Ω and the bandwidth $\Delta\lambda/\lambda$ of the beam diffracted by the beamline Si(111) monochromator are significantly larger than the angular acceptance and the bandwidth $\Delta\lambda/\lambda$ of the Si(511) reflection. This is indicated in the DuMond diagram of figure A.2. As a result the value for the reflectivity is much lower than 0.73. Additionally, one should note that the photon flux is filtered significantly by the dispersive scheme of the BC2 - BC3 crystals. Only 6.1% of the 8.39 keV radiation can be transmitted through this crystal configuration.

[1] note that the beam size in the experiment is relatively large. The performance of the same crystal was found to improve when illuminating it with smaller beam, which is demonstrated in section 4.1.2.

Table A.2: Measured T_M, corrected for the X-ray absorption in air T_{ABS} and calculated T_C values of the delay unit throughput in the Bragg - branch configuration.

hkl	E [keV]	Mono	T_M	T_{CORR}	T_{CALC}
511	8.39	Si(111)	1.9×10^{-5}	4.2×10^{-5}	1.1×10^{-3}

The measured throughput T_M of the Bragg optics is 1.9×10^{-5}. Correcting this value for the X-ray absorption in air yields $T_{ABS}= 4.2\times10^{-5}$, which is considerably smaller than the calculated value, i.e. $T_{CALC} = 1.1\times10^{-3}$. The results of the throughput measurements are summarized in table A.2.

The measurements at a bending magnet source support the result from chapter 4 and confirms the good quality of the employed Bragg crystals. The throughput of the delay unit optics strongly depends on the properties of the incident beam. A much higher throughput of the delay unit should be achieved with sources of the emmitance lower than a bending magnet as shown in section 4.1.1.

A.3 Laue-Bragg and Bragg-Laue crystal settings

The effect of the crystal geometry on the reflected beam divergence is shown in figure A.3. The rocking curves of the Si(511) Laue beam splitter and the Bragg crystal were measured at the position SP1 (see figures 2.5 and A.3b). The diffracted intensity was recorded by ionization chamber (IC) situated at 90° above the crystal in the scattering plane. Although the incident radiation was monochromatized ($\Delta\lambda/\lambda = 8.6 \cdot 10^{-6}$) the broadening of the Laue rocking curve relative to the Bragg curve is clearly visible. It is evident from the figure, that the exit divergence of the beam splitter is larger than the angular acceptance of the crystal. This behavior can be explained by the dispersion effect of wavelengths into angles, which is characteristic to the Laue geometry (cf. section 2.5). Since the divergence of the beam is reduced to the Darwin width of Si(511) by the (+n, +n) crystal arrangement of BC1 and BC2 (in the upper branch) or BC5 and BC6 (in the lower branch) any increase of the beam divergence introduced by the first beam splitter leads to a decrease of the overall throughput.

As demonstrated above, the use of Laue crystal as a beam splitter affects the overall throughput. Another effect has to be taken into account when the Laue crystal is used at the position SP2. Since the divergence of the beam splitter is

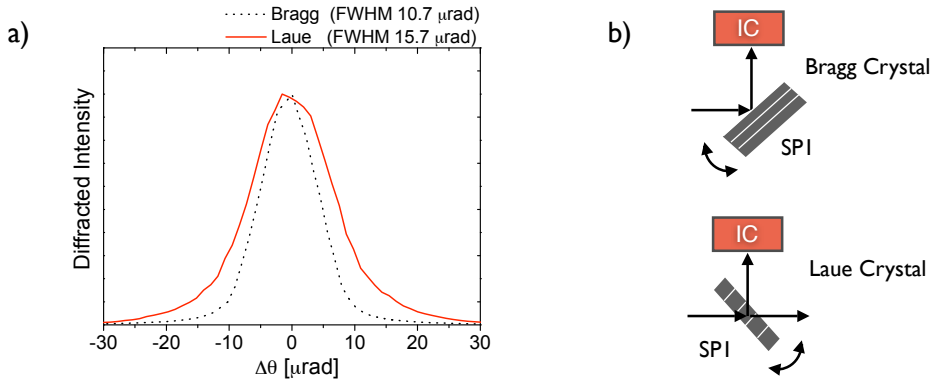

Figure A.3: a) Rocking curves of Laue and Bragg crystals measured at the position SP1 shown in figure 2.5. b) Corresponding Bragg and Laue geometries. IC denotes the ionization chamber detector.

larger than the Bragg reflector, the two exit beams of the delay unit will have a slightly different divergence. This effect is illustrated in figure A.4a, which shows rocking curves of Bragg and Laue crystals at positions BC3 and SP2, respectively. Figure A.4b shows the corresponding crystals of the two-brach configuration of the delay unit. The FWHM of the Laue rocking curve is more than 3.2 μrad larger compared to the Bragg crystal case.

It is important to note that the Laue beam splitter at the SP2 position is the last crystal in the delay unit and any modification of the beam properties (such as divergence) will also have a direct influence on the experiments taking place downstream. In case of experiments involving coherent X-rays and a pinhole aperture located downstream of the delay unit, the increase in beam divergence by SP2 leads to a decrease of the coherent flux at the sample position[2].

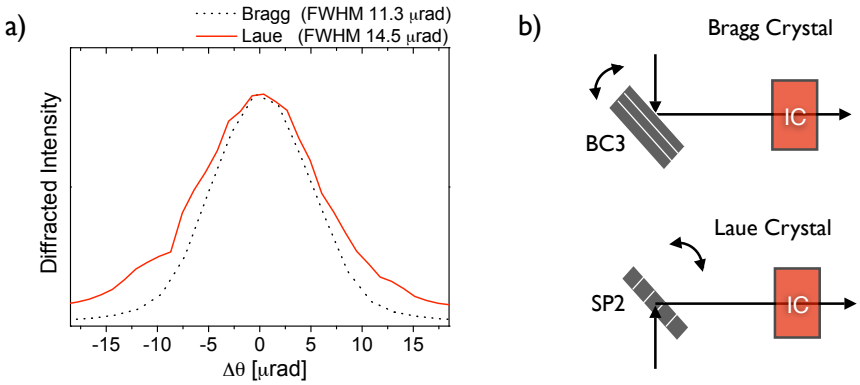

Figure A.4: a) Rocking curves of Laue and Bragg crystals measured at positions SP2 and BC3, respectively. b) Corresponding Bragg and Laue geometries. Note that the figure shows only selected crystals of the delay unit in the two-branch configuration. IC denotes the ionization chamber detector.

[2]compared to the optimally matched conditions e.q. using a Bragg beam splitter.

Bibliography

[1] XFEL: Technical Design Report Part V. (2001)

[2] LCLS, The First Experiments (2000)

[3] http:/www.riken.jp/XFEL/eng/greeting.html (2008)

[4] M. Dantus, M. J. Rosker, and A. H. Zewail. The Journal of Chemical Physics, **87** 2395 (1987)

[5] H. Ihee, M. Lorenc, T. K. Kim, Q. Y. Kong, M. Cammarata, J. H. Lee, S. Bratos, and M. Wulff. Science, **309** 1223 (2005)

[6] C. Spielmann, N. H. Burnett, S. Sartania, R. Koppitsch, M. Schnurer, C. Kan, M. Lenzner, P. Wobrauschek, and F. Krausz. Science, **278** 661 (1997)

[7] C. Rischel, A. Rousse, I. Uschmann, P.-A. Albouy, J.-P. Geindre, P. Audebert, J.-C. Gauthier, E. Froster, J.-L. Martin, and A. Antonetti. Nature, **390** 490 (1997)

[8] R. W. Schoenlein, S. Chattopadhyay, H. H. W. Chong, T. E. Glover, P. A. Heimann, C. V. Shank, A. A. Zholents, and M. S. Zolotorev. Science, **287** 2237 (2000)

[9] J. Arthur, S. Boutet, J.-C. Castagna, H. Chapman, Y. Feng, W. Foyt, D. Fritz, K. Gaffney, G. Grübel, J. Hajdu, J. Hastings, N. Kurita, J. Larsson, K. Ludwig, M. Messerschmidt, J. Miao, D. Reis, A. Robert, G. Stephenson,

T. Tschentscher, and N. van Bakel. LCLS Ultrafast Science Instruments: Conceptual Design Report (2007)

[10] Technical Design Report of the European XFEL (2007)

[11] M. Drescher, M. Hentschel, R. Kienberger, M. Uiberacker, V. Yakovlev, A. Scrinzi, T. Westerwalbesloh, U. Kleineberg, U. Heinzmann, and F. Krausz. Nature, **419** 803 (2002)

[12] G. Grübel and F. Zontone. Journal of Alloys and Compounds, **362** 3 (2004)

[13] G. Grübel, G. B. Stephenson, C. Gutt, H. Sinn, and T. Tschentscher. Nuclear Instruments and Methods in Physics Research Section B: Beam Interactions with Materials and Atoms, **262** 357 (2007)

[14] Private communications with A. Robert

[15] R. Mitzner, M. Neeb, T. Noll, N. Pontius, and W. Eberhardt. S. Kleinfelder, D. L. Paisley, Z. Chang, J.-C. Kieffer, and J. B. Hastings, editors, *Ultrafast X-Ray Detectors, High-Speed Imaging, and Applications. Edited by Kleinfelder, Stuart; Paisley, Dennis L.; Chang, Zenghu; Kieffer, Jean-Claude; Hastings, Jerome B. Proceedings of the SPIE, Volume 5920, pp. 86-95 (2005).*, volume 5920 of *Presented at the Society of Photo-Optical Instrumentation Engineers (SPIE) Conference*, 86–95 (2005)

[16] *X-ray beam transport and diagnostic.* Technical report, LCLS (2002)

[17] S. Joksch, W. Graeff, J. B. Hastings, and D. P. Siddons. Proceedings of the 4th international conference on synchrotron radiation instrumentation, **63** 1114 (1992)

[18] J. Als-Nielsen and D. McMorrows. *Elements of Modern X-ray Physiscs*. John Wiley & Sons (2001)

[19] B. E. Warren. *X-Ray Diffraction*. Dover Publications (1990)

[20] B. W. Batterman and H. Cole. Rev. Mod. Phys., **36** 681 (1964)

[21] A. Authier. *Dynamical theory of x-ray diffraction*. Oxford University Press (2001)

[22] W. H. Zachariasen. *Theory of X-Ray diffraction in Crystals*. Willey, New York (1945)

[23] S. Brauer, G. B. Stephenson, M. Sutton, S. G. J. Mochrie, S. B. Dierker, R. M. Fleming, R. Pindak, I. K. Robinson, G. Grübel, J. Als-Nielsen, and D. L. Abernathy. Proceedings of the 5th International Conference on Synchrotron Radiation Instrumentation, **66** 1506 (1995)

[24] R. J. Dejus and M. S. del Rio. *XOP: A graphical user interface for spectral calculations and x-ray optics utilities*, volume 67, 3356–3356. AIP (1996)

[25] L. B. Da Silva, T. W. Barbee, Jr., R. Cauble, P. Celliers, D. Ciarlo, S. Libby, R. A. London, D. Matthews, S. Mrowka, J. C. Moreno, D. Ress, J. E. Trebes, A. S. Wan, and F. Weber. Phys. Rev. Lett., **74** 3991 (1995)

[26] E. Goulielmakis, G. Nersisyan, N. A. Papadogiannis, D. Charalambidis, G. D. Tsakiris, and K. Witte. Applied Physics B: Lasers and Optics, **74** 197 (2002)

[27] H. Mashiko, A. Suda, and K. Midorikawa. Applied Physics B: Lasers and Optics, **76** 525 (2003)

[28] G. Grübel, J. Als Nielsen, and A. K. Freund. Journal de Physique IV, **4** 27 (1994)

[29] J. Feldhaus, T. Möller, E. L. Saldin, E. A. Schneidmiller, and M. V. Yurkov. Nuclear Instruments and Methods in Physics Research Section A: Accelerators, Spectrometers, Detectors and Associated Equipment, **507** 435 (2003)

[30] T. Rautenstrauch. *Untersuchungen mit einem neu entwickelten Röntgen-Michelson-Interferometer auf Basis eines Bragg-Dreistrahlfall-Interferometers*. Ph.D. thesis, Institut für Experimentalphysik, Dortmund (1996)

[31] A. Appel and U. Bonse. Phys. Rev. Lett., **67** 1673 (1991)

[32] S. D. Shastri, P. Zambianchi, and D. M. Mills. D. M. Mills, H. Schulte-Schrepping, and J. R. Arthur, editors, *Proc. SPIE Vol. 4143, p. 69-77, X-Ray FEL Optics and Instrumentation, Dennis M. Mills; Horst Schulte-Schrepping; John R. Arthur; Eds.*, volume 4143 of *Presented at the Society of Photo-Optical Instrumentation Engineers (SPIE) Conference*, 69–77 (2001)

[33] S. D. Shastri, P. Zambianchi, and D. M. Mills. Journal of Synchrotron Radiation, **8** 1131 (2001)

[34] J. W. M. DuMond. Phys. Rev., **52** 872 (1937)

[35] O. Seeck. Hasylab Annual Report, 333 (2006)

[36] T. Matsushita and H. Hashizume. *Handbook on Synchrotron Radiation: X-Ray Monochromators*, volume 1. North-Holland Publishing Company (1983)

[37] S. K. Allison and J. H. Williams. Physical Review, **35** (1930)

[38] Knoll. *Radiation Detection and Measurement*. Jon Wiley & Sons Inc. (2003)

[39] A. Q. R. Baron, S. Kishimoto, J. Morse, and J.-M. Rigal. Journal of Synchrotron Radiation, **13** 131 (2006)

[40] S. Kishimoto. Nucl. Instrum. Methods Phys. Res. A, **309** 603 (1991)

[41] T. Kracht. SPECTRA http:/hasylab.desy.de/infrastructure/index_eng.html

[42] T. Kracht. Computing at Hasylab (1998)

[43] D. Le Bolloch, F. Livet, F. Bley, T. Schulli, M. Veron, and T. H. Metzger. Journal of Synchrotron Radiation, **9** 258 (2002)

[44] A. Robert. *Dynamical behavior of charge stabllizized colloidal suspensions*. Ph.D. thesis, ESRF (2001)

[45] T. Ishikawa, K. Hirano, and S. Kikuta. Nuclear Instruments and Methods in Physics Research Section A: Accelerators, Spectrometers, Detectors and Associated Equipment, **308** 356 (1991)

[46] T. Ishikawa. Acta Crystallographica Section A, **44** 496 (1988)

[47] Private communications with the staff of the beamline ID10C of ESRF

[48] Private communications with the staff of the beamline ID18 of ESRF

[49] Private communications with Frank Brinker

[50] M. Born; and E. Wolf. *Principles of Optics*. Cambridge University Press, sixth edition (1999)

[51] D. L. Abernathy, G. Grübel, S. Brauer, I. McNulty, G. B. Stephenson, S. G. J. Mochrie, A. R. Sandy, N. Mulders, and M. Sutton. Journal of Synchrotron Radiation, **5** 37 (1998)

[52] O. K. C. Tsui, S. G. J. Mochrie, and L. E. Berman. Journal of Synchrotron Radiation, **5** 30 (1998)

[53] J. W. Goodman. *Statistical Optics*. John Willey & Sons (1985)

[54] Private communications with the staff of the beamline ID10C of ESRF

[55] W. Stober, A. Fink, and E. Bohn. Journal of Colloid and Interface Science, **26** 62 (1968)

[56] G. V. Schulz. Zeitschrift fur Physikalische Chemie-Abteilung B-chemie der Elementarprozesse Aufbau der Materie, **43** 25 (1939)

[57] http://www.aerotech.com/cp.html

Acknowledgments

During this project, I was fortunate to have come in touch with a variety of people who directly or indirectly supported me, making this project possible. One of the pleasures of finishing this project is certainly the opportunity to express my appreciation for these people.

First and foremost I'd like to thank my supervisors Dr. Gerhard Grübel, Dr. Hermann Franz and Prof. Dr. Wilfried Wurth. I am indebted and thankful them for offering me the opportunity to work with them on this project. I especially would like thank Dr. Gerhard Grübel for the all the scientific support, advice, encouragement and guidance he gave me during years I spent in HASYLAB. I have benefited greatly from his ideas. He was always available when I needed his help or advice. Im also indebted to Dr. Hermann Franz for his valuable advice and supervision during this project. I always enjoyed scientific discussions with him. I appreciate that he always found the time whenever I had a question. Working with Dr. Gerhard Grübel and Dr. Hermann Franz was a real pleasure for me and it has been more than I could have ever asked as a PhD student. Without their support this thesis would not have been possible.

I would like to express my gratitude to Anita Ehnes for the enormous help during the designing process of the Delay Unit mechanics. Her assistance in the technical part of this project was indispensable. I'm also very grateful to Anita for her patience and understanding while training me in the (German version of)

Solid Edge.

A very special thanks goes to Dr. Horst Schulte-Schrepping and Manfred Spiwek from HASYLAB X-ray Optics Laboratory who provided all the crystals for the Delay Unit. Without their support this project would not be successful.

Dr. Gerhard Grübel, Dr. Hermann Franz, Dr. Horst Schulte-Schrepping, Dr. Olaf Leupold, Dr. Aymeric Robert and Dr. Walter Graeff carefully read the thesis manuscript. I'm very grateful to them for all constructive comments and fruitful discussions.

I'm indebted to the entire Scattering with coherence X-rays Group (Dr. Gerhard Grübel, Dr. Christian Gutt, Dr. Olaf Leupold, Dr. Tina Autenrieth, Dr. Lorenz Stadler, Dr. Agnès Duri, Dr. Simone Streit-Nierobisch, PhD student Fabian Westermeier) for the opportunity to work among them. The friendly and supportive atmosphere of this Group contributed enormously to the outcome of my project.

Dr. Olaf Leupold, Dr. Christian Gutt and Dr. Lorenz Stadler were always very enthusiastic about my project. I have enjoyed scientific and non scientific discussions with them. They gave me many valuable suggestions during the years I spent in HASYLAB and were always very keen on answering all my questions.

I'm also deeply indebted to Dr. Tina Autenrieth, who prepared a SiO_2 sample for the coherence x-ray scattering experiments at ESRF with the Delay Unit. Among many samples that were examined during the experiment only Tina's sample gave a strong scattering signal allowing the continuation of the experiment. Without her help this experiment would not have been as successful as it was.

Im also thankful to the members of the Hard X-ray scattering and diffraction Group for their help. In particular I'd like to thank Dr. Oliver Seeck for his help in setting the ray tracer for the Delay Unit and the numerous interesting (not only scientific) discussions. I'm also grateful to Ruediger Nowak, who helped me in the early stages of this project in purchasing most of the Delay Unit components.

I would also like to thank Dr. Wolfgang Calibe, Dr. M. von Zimmermann,

Dr. Karen Rickers, Dr. Bernd Struth, Dr. Olaf Leupold, Dr. Lorenz Stadler and Dr. Aymeric Robert who helped during the experiments with the Delay Unit at DORIS III and ESRF.

To the members of the Troïka beamline, in particular Dr. Federico Zontone and Dr. Anders Madsen - many thanks for their great support during experiments at ESRF.

I'd like to thank Jens Brehling and the HASYLAB workshop who prepared all the holders and spacers of the Delay Unit (some of them on a very short notice).

I thank Dirk Samberg and Andre Gande who were always keen on helping me.

I would also like to thank my friends in the HASYLAB, particularly Kai, Sebastien, Bente, Lorenz, Tina, Fabian and Agnès for cheer and great fun. I've always enjoyed conversations with them not only during lunch and coffee breaks but also after work. I'm grateful to Fabian, who helped me a lot with translations of many scientific and non-scientific papers from German to English.

Special thanks goes to Agnès. She was a source of great emotional support during the thesis writing period. I cannot adequately express how thankful I am.

I'd also like to thank my office-mates Marcin, Gerd and Milena; I enjoyed the numerous debates with them.

Many thanks go also to Marcin, a very good friend of mine, who studied with me at universities in Poland, Denmark and now in Germany.

Finally, but not least, I want to thank my parents, Czeslaw and Zofia, and my sister Agnieszka whose patience, support, and understanding helped me to write this thesis.